

DOKUZ EYLÜL UNIVERSITY
GRADUATE SCHOOL OF NATURAL AND APPLIED SCIENCES

DAMAGE IN LAMINATED COMPOSITE PLATES
SUBJECTED TO LOW- VELOCITY IMPACT

by
Bülent Murat İÇTEN

May, 2006
İZMİR

**DAMAGE IN LAMINATED COMPOSITE PLATES
SUBJECTED TO LOW-VELOCITY IMPACT**

**A Thesis Submitted to the
Graduate School of Natural and Applied Sciences of Dokuz Eylül University
In Partial Fulfillment of the Requirements for the Degree of Doctoral of Philosophy
in Mechanical Engineering, Mechanics Program**

**by
Bülent Murat İÇTEN**

**May, 2006
İZMİR**

Ph.D. THESIS EXAMINATION RESULT FORM

We have read the thesis entitled “**DAMAGE IN LAMINATED COMPOSITE PLATES SUBJECTED TO LOW-VELOCITY IMPACT**” completed by **BÜLENT MURAT İÇTEN** under supervision of **Prof. Dr. RAMAZAN KARAKUZU** and we certify that in our opinion it is fully adequate, in scope and in quality, as a thesis for the degree of Doctor of Philosophy.

Prof. Dr. Ramazan KARAKUZU

Supervisor

Prof. Dr. Onur SAYMAN

Assist. Prof. Dr. Mustafa TOPARLI

Committee Member

Committee Member

Prof. Dr. Alaeddin ARPACI

Prof. Dr. Sami AKSOY

Jury Member

Jury Member

Prof. Dr. Cahit HELVACI

Director

Graduate School of Natural and Applied Sciences

ACKNOWLEDGEMENTS

First of all, I would like to thank my supervisor Professor Ramazan KARAKUZU, for providing, excellent guidance and constant encouragement throughout this work.

Special thanks are also extended to the members of my thesis committee, Professor Onur SAYMAN and Assistant Professor Mustafa TOPARLI for their help with valuable suggestions.

I am grateful to the TÜBİTAK (The Scientific and Technical Research of Turkey), for providing me with the necessary funding to complete my doctoral study at Michigan State University in USA, in scope of the NATO Science Fellowships Programme.

I want to thanks to Professor Dashin Liu, for his guidance, assistance and hospitality during my stay at Michigan State Univesity.

I am also thankful to my colleagues for their ideas, assistance and moral support throughout this study.

Finally, I wish to thank my family members, especially my wife and my son, for their patience and understanding.

Bülent Murat İÇTEN

DAMAGE IN LAMINATED COMPOSITE PLATES SUBJECTED TO LOW-VELOCITY IMPACT

ABSTRACT

The aim of the study is to investigate the impact response of laminated composites were constructed from orthotropic layers containing collimated unidirectional fibers or woven fabrics made of glass fabrics and an epoxy matrix. The effects of the following parameters on the impact resistance of composite plates were studied: the angle between adjacent layers, weaving gaps, the curing pressure, the size of weaving cell, the stitching reinforcement through the composite thickness and the weaving angle between fill and warp yarns.

An instrumented drop-weight impact testing machine was used in the investigations. Because of the special fiber geometries involved in the study, all woven composites were fabricated manually. Some of the composite prepregs were stitched after stacking together by hand, using a needle. The perforation threshold, peak force and bending stiffnesses were identified to be the primary impact characteristics of the composites.

Experimental results reveal that weaving with gap and curing with low pressure increases the perforation threshold. The perforation thresholds increases as the angles between adjacent layer and the weaving angle between fill and warp yarns decrease. Since the fill and warp yarns constrain the damage propagation, the cell size plays an important role in the damage process. Damage size and perforation threshold reduce with stitching.

A numerical evaluation was carried out by using a finite element code. The contact force history between impactor and the composite plate consist of unidirectional plies was found for the specimens which occurred no fiber breakage in experiments. The experimental results and numerical results are reasonable.

Keywords: impact behavior, laminated composites, cell size, stitching, weaving angle, perforation threshold

DÜŞÜK HIZLI DARBEYE MARUZ TABAKALI KOMPOZİT PLAKLARDA HASAR ANALİZİ

ÖZ

Bu çalışmanın amacı, cam lifi ve epoksiden imal edilmiş, tek yönlü fiberlerin yan yana yerleştirilmesi ile oluşturulmuş ortotropik tabakalardan veya örülü kumaşlardan üretilmiş tabakalı kompozitlerin darbe cevabını incelemektir. Kompozit plakaların darbe dirençleri üzerine çalışılan parametreler: tabakalar arası açı değişimi, örgüdeki boşluklar, pişirme basıncı, örgü hücresinin boyutu, kompozit kalınlığı boyunca dikiş ile güçlendirme ve atkı ve çözgü iplikleri arasındaki örme açısıdır.

Araştırmada ağırlık düşürme cihazı kullanılmıştır. Çalışmada kullanılan özel fiber geometrilerinden dolayı bütün örgülü kompozitler elle üretilmiştir. Bazı kompozit prepregler üst üste sıralandıktan sonra bir iğne vasıtası ile elle dikilmiştir. Delme eşiği, maksimum kuvvet ve eğilme rijitliği, kompozitlerin temel darbe özelliklerini tanımlamada kullanılmıştır.

Deneysel sonuçlar, boşluklu örme ve düşük basınçla pişirmenin delme eşiğini yükselttiğini göstermiştir. Delme eşiği ardışık tabakalar arası açının ve atkı ve çözgü iplikleri arasındaki örgü açısının azalması ile artmıştır. Atkı ve çözgü ipliklerinin hasar ilerlemesini sınırlandırmasından dolayı, hücre boyutu hasar mekanizmasında önemli bir rol oynar. Hasar boyutu ve delme eşiği dikme ile azalmıştır.

Sonlu elemanlar metodu ile yazılmış bir programla nümerik bir değerlendirme yapılmıştır. Tek yönlü fiberlerden oluşan tabakalardan teşekkül etmiş kompozit plaklarla darbe ucu arasındaki temas kuvvetleri, deneylerde fiber kırılması oluşmayan numuneler için bulunmuştur. Deneysel sonuçlar ile nümerik sonuçlar birbirine uyumlu çıkmıştır.

Anahtar kelimeler: darbe davranışı, tabakalı kompozitler, hücre boyutu, dikme, örme açısı, delme eşiği

CONTENTS

	Page
THESIS EXAMINATION RESULT FORM.....	ii
ACKNOWLEDGEMENTS.....	iii
ABSTRACT.....	iv
ÖZ.....	v
CHAPTER ONE – INTRODUCTION.....	1
1.1 Overview.....	1
1.2 Objectives of the Present Research.....	6
CHAPTER TWO - IMPACT ON COMPOSITE PLATES.....	8
2.1 Introduction.....	8
2.2 Composite Laminates.....	8
2.2.1 Unidirectional Fabric.....	9
2.2.2 Woven Fabric.....	9
2.3 Material.....	11
2.4 Impact on Composite Plates.....	12
2.5 Failure Modes	13
2.6 Impact Testing Methods.....	16
CHAPTER THREE - EXPERIMENTAL METHOD.....	18
3.1 Introduction.....	18
3.2 Material.....	18
3.3 Manufacturing	18
3.3.1 Laminated Plates with Unidirectional Laminas.....	19
3.3.2 Two Dimensional Woven Laminas.....	21
3.3.3 Stitched Laminates.....	24
3.4 Curing	25

3.5 Design of the Composite Plate.....	27
3.6 Impact Testing	29
3.7 Analysis of the Impact Test Results.....	32
3.8 Absorbed Energy.....	35
3.9 Energy Profile	36
CHAPTER FOUR - NUMERICAL PROCEDURE.....	39
4.1 Introduction.....	39
4.2 Stress Analysis.....	40
4.3 Failure Analysis.....	42
4.3.1 Critical Matrix Cracking Criterion.....	42
4.3.2 Impact Induced Delamination Criterion.....	44
CHAPTER FIVE - RESULTS AND DISCUSSION.....	49
5.1 Introduction.....	49
5.2 $[90/0]_6$ Composites.....	49
5.3 Stacking Sequence Effect.....	55
5.4 Pressure and Gaps between Cells Effect.....	60
5.5 Cell Size Effect.....	65
5.6 Stitching Effect.....	69
5.7 Angle between Fill and Warp Effect.....	76
5.8 Numerical Results.....	79
CHAPTER SIX – CONCLUSIONS.....	87
REFERENCES.....	89
APPENDIX.....	96

CHAPTER ONE

INTRODUCTION

1.1 Overview

Laminated composite materials are used extensively in the various fields of structural engineering because of their excellent in-plane mechanical properties, such as stiffness and strength, with low density. The composite materials, however, are highly susceptible to transverse loading. In aircraft applications the components have to survive in low velocity impacts from dropped tools and rough handling during maintenance, in intermediate velocity impacts from runway stones and bird strike, and in high velocity weapon attack for military aircraft. The out of plane impact loading is considered potentially dangerous mainly because the damage may be left undetected and because the loading itself acts in the through-the-thickness direction of the laminated composite plate. This direction is the weakest in the composite since no fibers are present in that direction. The impact loading can lead to damage involving three modes of failure: matrix cracking, delamination and eventually fiber breakage for higher impact energies. Even when no visible impact damage is observed at the surface on the point of impact, matrix cracking and delamination can occur. This damage can alter the structural response during impact and reduce subsequent structural performance. Therefore, the problem of low velocity impact of laminated composite materials has been received much attention in recent years. Many experimental and numerical studies on the impact response of composite laminates can be found in the literature (Abrate, 1991, 1994, 1998; Cantwell, 1991)

Delamination has been a major concern in damaged composite laminates because it appears to be the major cause of composite disintegration. A few techniques have been developed to improve delamination resistance by applying through-thickness reinforcement to composite laminates, e.g. stitching and z-pinning. Another way to reduce the risk of delamination is perhaps to use woven composites, rather than laminated composites. When a crack takes place in a woven composite layer, it tends to

propagate into the composite thickness as the surrounding fill and warp yarns hinder the advancement of the crack and suppress the growth of delamination (Hosur et al., 2003). Besides higher delamination resistance, easier to handle is also an advantage of woven fabrics over unidirectional layers. Plain-weave fabrics are especially common as they provide balanced in-plane properties (Naik et al., 2000).

There have been quite some studies on impact response of woven composites (Baucom et al., 2004; Baucom & Zikry, 2005; Curtis & Bishop, 1984; Gillespie et al., 2003; Jenq et al., 1994; Kim & Sham, 2000; Naik & Sekher, 1998; Naik et al., 2002; Shioh & Shim, 1998; Sutherland & Soares, 1999). Naik & Sekher (1998) have investigated the behavior of unidirectional composite laminates and woven composite laminates under low-velocity impact by using a three-dimensional transient finite element code. They have observed that the failure function is lower for woven composite laminates than for unidirectional composite laminates, implying that woven composite laminates have higher resistance to impact loading. Kim and Sham (2000) have found that woven fabric composite laminates have higher fracture toughness, higher residual compression after impact, lower maximum load and smaller damage area than cross-ply composite laminates. Similarly, Curtis and Bishop (1984) have shown that woven composites have higher residual strength after impact and less damage than non-woven laminated composites. Owing to the advantages of woven composites in resisting impact loading, the present study is focused on woven composites.

In an effort to improve impact resistance by reducing delamination, composite laminates with small angle between adjacent lamina have been investigated. Liu (2004) has studied $[0_5/\theta_5/0_5]$ composite laminates, where $\theta = 15, 30, 45,$ and 90 , and found that the penetration and perforation thresholds increase as the fiber orientation in the middle lamina decreases. That is, the $[0_5/15_5/0_5]$ composite has the highest penetration and perforation thresholds among the four cases. Since delamination is caused by the high interlaminar stress resulting from mismatch of bending stiffness between adjacent laminae, a smaller angle between adjacent laminae should give a smaller bending

stiffness mismatch and leads to a lower interlaminar stress (Liu, 1988). As conventional fabrics utilize orthogonal weaving between fill and warp yarns, the present study is to explore the feasibility of extending the advantage of using small angle between adjacent laminae in laminated composites to small weaving angle between fill and warp yarns in woven composites.

Stitching has been commonly used in reinforcing laminated composites through thickness (Chen et al., 2004; Hosur, Adya et al., 2004; Hosur, Vaidya et al., 2004; Kang & Lee 1994; Larsson, 1997; Lopresto et al., 2006; Mouritz & Cox , 1997 ; Reeder, 1995; Sharma & Sankar, 1997). However, mixed results seem to exist in different research articles. For example, stitching seems to improve delamination resistance while it also adversely affects the compressive strength of composite laminates due to fiber misalignment (Reeder, 1995). Mouritz & Cox (1997) have performed a critical appraisal on a large amount of published data of mechanical properties. Their appraisal reveals that stitching usually reduces the stiffness, strength and fatigue resistance of a laminate by 10 to 20% although in a few cases the mechanical properties remain unchanged or increase slightly.

Besides laminated composites, stitching has also been applied to woven composites. Hosur, Vaidya et al. (2004) have investigated the response of stitched and unstitched woven carbon/epoxy composite laminates subjected to high-velocity impact. Their study has indicated that damage can be well constrained within the stitching grids though ballistic limit is higher in the unstitched composites. Lopresto et al (2006) have shown that the presence of stitches does not substantially affect the composite behavior in terms of force-displacement curve, first failure load and indentation. However, the stitched composites exhibit penetration energy about 30% lower than the unstitched ones. The advantage of stitching in terms of impact resistance is evident only in thick composites. Kang and Lee (1994) have studied the mechanical properties as well as the impact properties of stitched woven composites. They have found that the mechanical properties of woven composites are improved if they are stitched with an optimum density and the energy absorption capacity of the stitched composites is higher than that

of unstitched ones. The damaged areas caused by the penetration are far smaller in the stitched composite than in the unstitched one. A 10% improvement in ballistic efficiency has been identified. Sharma and Sankar (1997) have shown that the stitching does not affect the onset of impact damage. However, stitching leads to significant improvement in impact damage tolerance in terms of compression after impact strength and impact damage area. They have also found that stitched laminates have higher Mode I and Mode II fracture toughness values than the unstitched laminates. Due to the mixed results from stitching, the present study also investigates the stitching effect in woven composites with small weaving angle and various cell sizes.

Besides delamination, perforation is another important damage mode in composite materials because it is the ultimate damage of composite materials subjected to impact loading. Prior to perforation, impact characteristics, such as peak force, contact duration, maximum deflection and absorbed energy, can be identified from load-deflection curves. They are important parameters to understanding the damage process of composite materials. Other indirect parameters including residual compressive force and residual energy absorption after perforation have also been used in evaluating the impact response of composite materials (Liu, 1988, 2004; Liu & Raju, 2000; Liu et al, 2000). In this study, the impact characteristics, energy absorption capability and the damage process are used to evaluate the woven composites.

In order to predict the impact behavior of the composite materials, many investigators performed numerical and analytical study. Wu & Chang (1989) performed a transient dynamic finite element analysis for studying the response of laminated composite plates due to transverse foreign object impact. The analysis can be used to calculate displacements of composite plate during impact and the transient stress and strain distributions through the laminate thickness. An 8 point brick element with incompatible modes was developed in the analysis, and the direct Gauss quadrature integration scheme was used through the element thickness to account for the change in material properties from layer to layer within the element. The Newmark scheme was adopted to perform time integration from step to step. A contact law incorporated with the Newton

Rapson method was applied to calculate the contact force during impact. A computer code was developed based on the analysis. The results of calculations from the code were compared with the existing analytical solutions.

Choi, Downs et al. (1991) and Choi, Wu et al. (1991) done an investigation consisting of both analysis and experiments on impact damage mechanisms and mechanics of laminated composites subjected to low-velocity impact. In order to fundamentally understand the impact damage of laminated composites, a unique test program was developed and performed by using a specially designed line loading impactor. A design of line-nose impactor was chosen in that study to simplify the impact damage mechanisms from three-dimensional to two-dimensional. Choi and Chang (1992) was developed a model based on the study of the line loading impact (Choi, Wu et al., 1991), for predicting the impact damage of graphite/epoxy laminated composites resulting from point-nose impact. Lee et al. (1984) made a three dimensional finite elements and dynamic analysis for a layered fiber-reinforced composite laminate subjected to impact loading. Central difference method was employed in this analysis. Naik et al. (2000) studied on the behavior of woven-fabric laminated composite plates under transverse central low-velocity point impact by using a modified Hertz law and a 3D transient finite-element analysis code. A failure function based on Tsai-Hill quadratic failure criterion was used to evaluated the in plane failure behavior of the composite. A method for simple prediction of the impact force history on composite laminates subjected to low-velocity impact was proposed by Choi & Hong (1994). Frequency characteristics of the numerical impact force history were investigated from modal analysis and compared with the natural frequencies of the system in which the mass of an impactor was lumped with the plate. Finite element procedure were used in conjunction with a numerical algorithm to compute the impact response of a graphite-epoxy laminated beam subjected to tensile initial stresses by Sankar & Sun (1985). The effect of initial stresses on the contact duration, impact force, coefficient of restitution, and bending and shear stresses were evaluated.

Low velocity impact response of laminated plates was investigated analytically (Abatan et al. 1998; Kim & Kang, 2001; Pierson & Vaziri, 1996; Ramkumar & Chen, 1982). An analytical model for the impact response of laminated composite plates presented by Pierson & Vaziri (1996). The governing equation which apply to small deflection elastic response of special orthotropic laminates, include the combined effects of shear deformation, rotary inertia, and the nonlinear Hertzian contact law.

Ferites et al.(2000) carried out a study to determine the mechanisms of the damage growth of impacted composite laminates. For this purpose a series of impact tests and numerical evaluation were done. Hou et al. (2000) gave the details of the implementation of improved failure criteria for laminated composite structures into LS-DYNA3D. Out-of-plane stresses had been taken into consideration. Aslan & Karakuzu (2002) studied on the transient response of composite laminates subjected to low velocity impact. The numerical evaluation carried out by using 3DIMPACT transient finite element analysis code. Aslan et al. (2002) and Aslan et al. (2003) examined the size effects including both in plane dimensional and thickness effects for laminated woven E-glass-epoxy composite subjected to heavy mass impact.

1.2 Objectives of the Present Research

The objective of the present study is to improve the impact resistance of laminated composites which consist of unidirectional layers and woven layers. To evaluate the impact behavior, the composites should be produced same conditions such as the same volume fraction, curing temperature and pressure. The laminated composite consist of unidirectional layers prepared from the prepreg tapes made of unidirectional E-glass fibers and an epoxy matrix, namely glass/epoxy tape. Woven composites with various cell sizes and weaving angles were also produced from the same prepreg tape by hand.

At the beginning of the study, the effect of angle between adjacent layers on impact is investigated. Following, to determine some weaving parameter such as gaps between the cells, the composite are woven with gap and without gap. Prepared composites cured

under low pressure and high pressure. After determining the weaving and curing condition, cell size effect on impact behavior of composite materials is studied. Cell size can affect the damage growth. Damage growth is critical to the impact-induced damage process and is also of interest in this study. As stitching is a common technique for reinforcement through thickness and its effect on impact resistance is relatively mixed, it is also investigated. Finally, the effect of small weaving angle, between fill and warp yarns, on impact resistance is studied.

A numerical evaluation of laminated composite consist of unidirectional laminas were performed using 3DIMPACT transient dynamic finite element code from F. K. Chang. The computer code was made by H. Y. Choi & F. K. Chang at the Department of Aeronautics and Astronautics in Stanford University and modified by Seng Guan Lee & Iqbal Shadid.

CHAPTER TWO

IMPACT ON COMPOSITE PLATES

2.1 Introduction

Among the modern structural materials, the history of fiber reinforced composites is only four decades old. However, in this short period of time, there has been a tremendous advancement in the science and technology of this new class of materials. Fiber- reinforced polymers are now used in the applications ranging from spacecraft frames to ladder rails, from aircraft wings to automobile doors, from rocket motor cases to oxygen tanks (Mallick, 1993).

However, their behavior under impact loading is one of the major concerns, since impacts do occur during manufacture, normal operations maintenance, etc. Impact loading can induce significant internal damage that causes reductions in the strength and the stability of the laminated composite. Therefore, the effect of foreign object impacts on the structures made of laminated layers must be understood, and proper measures should be taken in the design process.

2.2 Composite Laminates

Laminated composites are constructed from orthotropic plies containing collimated unidirectional fibers or woven fabrics (Carlsson, 1997). Laminated composites made of unidirectional tape layers have been popular and the focus of much research for a long time. However, woven fabric composites have been recognized as more competitive than unidirectional composites in many structural applications. Woven fabric composites offer better dimensional stability over a large range of temperatures and reduced cost of manufacturing. Therefore, in this study, woven fabric composites have been utilized, extensively.

2.2.1 Unidirectional Fabric

In unidirectional (UD) fabrics, the fibers run in one direction only. A small amount of fiber or other material may run in other directions for holding the primary fibers in position. In prepreg unidirectional tapes where there is no secondary material at all holding the unidirectional fibers in place. In these prepreg products only the resin system holds the fibers in place.

2.2.2 Woven Fabric

Woven fabrics are fabricated by the interlacing of warp fibers and fill fibers in a regular pattern or weave style. The fabric's integrity is maintained by the mechanical interlocking of the fibers. Drapability (the ability of a fabric to conform to a complex surface), surface smoothness and stability of a fabric are controlled primarily by the weave style. Each weave style has some advantages and disadvantages together. The most commonly used weave styles are shown in Figure 2.1 (Netcomposites, nd).

In the plain weave, yarns are interlaced in an alternating fashion over and under every other yarn. This provides the thinnest, lightest weight fabrics with maximum stability, firmness and minimum yarn slippage. However, it is the most difficult of the weaves to drape, and the high level of fiber crimp imparts relatively low mechanical properties compared with the other weave styles. It is the primary weave for the coating industry. Basket weave is fundamentally the same as plain weave except that two or more warp fibers alternately interlace with two or more fill fibers. Basket weave is flatter, and, through less crimp, stronger than a plain weave, but less stable.

In twill weave, one or more warp fibers alternately weave over and under two or more fill fibers in a regular repeated manner. This weave permits a greater number of yarns per unit area than a plain weave, while preserving good fabric stability. With reduced crimp, the fabric also has a smoother surface and slightly higher mechanical properties. Satin weaves are fundamentally twill weaves modified to produce fewer intersections of warp and fill. Satin weaves are very flat, have a high degree of drape.

The low crimp gives good mechanical properties. Satin weave is ideal for the reinforced plastic field, particularly prepregs for aircraft and missiles.

Leno weave improves the stability in ‘open’ fabrics which have a low fiber count. A form of plain weave in which adjacent warp fibers are twisted around consecutive fill fibers to form a spiral pair, effectively ‘locking’ each fills in place. Grinding wheel reinforcement, lightweight membrane and laminating fabrics use the leno weave to good advantage. Mock leno is a version of plain weave in which occasional warp fibers, at regular intervals but usually several fibers apart, deviate from the alternate under-over interlacing and instead interlace every two or more fibers. The comparison of weaving style is given in Table 2.1(Netcomposites, nd).

In this investigation, it is necessary to take a weave which have good stability, good balance and symmetrical properties. However, the smoothness, the crimp and porosity properties were not taken as parameters. Additionally, drape property is not important for planer plate. Therefore, plane weave was selected for current study.

Table 2.1 The properties comparison of weaving style

Property	Plain	Twill	Satin	Basket	Leno	Mock leno
Good stability	****	***	**	**	*****	***
Good drape	**	****	*****	***	*	**
Low porosity	***	****	*****	**	*	***
Smoothness	**	***	*****	**	*	**
Balance	****	****	**	*****	**	****
Symmetrical	*****	***	*	***	*	****
Low crimp	**	***	*****	**	*****	**

***** =excellent, ****= good, ***= acceptable, **=poor, *=very poor

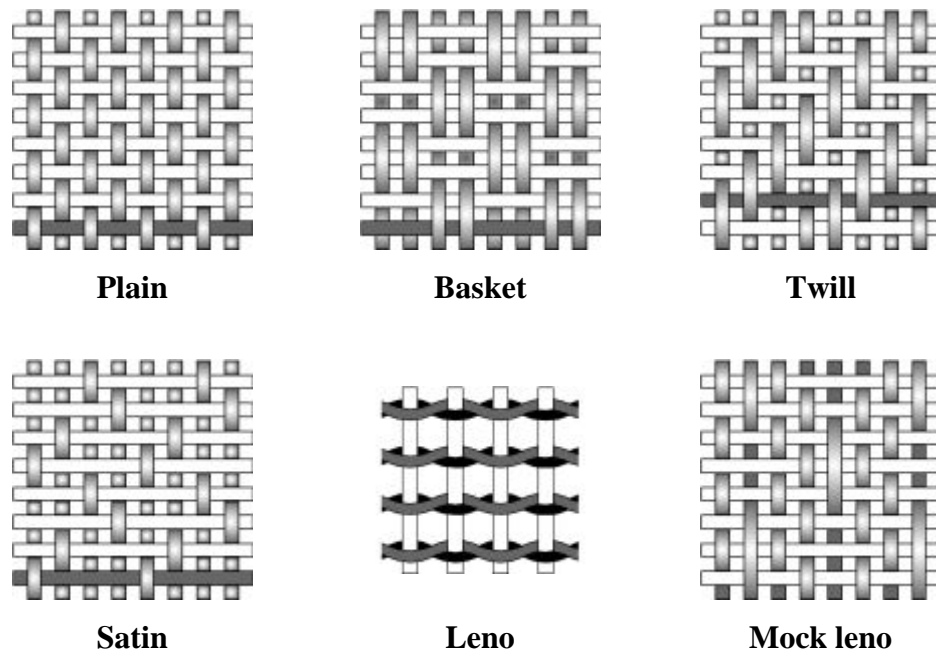


Figure 2.1 Some of the commonly used weave styles

2.3 Material

Glass fiber was selected as reinforcing of the composite. By variation of the recipe, different types of glass fiber can be produced. The types of glass used for structural reinforcements are follows:

- E-glass (electrical) has good tensile and compressive strength and stiffness, good electrical properties and relatively low cost, but impact resistance relatively poor. E-glass is the most common reinforcing fiber used in polymer matrix composites.
- C-glass (chemical) is the best resistance to chemical attack. Mainly used in the form of surface tissue in the outer layer of laminates used in chemical and water pipes and tanks.
- S-glass has higher tensile strength and modulus than E glass. It is developed for aerospace and defense industries, and used in some hard ballistic armor applications. This factor, and low production volumes mean relatively high price.

There are many different types of resin in use in the composite industry. The majority of structural parts are made with three main types, namely polyester, vinylester and epoxy.

Epoxy resins represent some of the highest performance resins of those available at this time. Epoxies generally out-perform most other resin types in terms of mechanical properties and resistance to environmental degradation, which leads to their almost exclusive use in aircraft components. As a laminating resin their increased adhesive properties and resistance to water degradation make these resins ideal for use in applications such as boat building (Netcomposites, nd). Epoxy matrix, as a class, has the following advantages over other thermoset matrices such as wide variety of properties, absence of volatile matters during cure, low shrinkage during cure, excellent resistance to chemicals and solvents, and excellent adhesion to a wide variety of fillers, fibers, and other substrates. The principal disadvantages are its relatively high cost and long curing time (Mallick, 1993).

In this investigation, the E-glass fiber and epoxy resin were selected in form of prepreg tapes. The plain weave composite layers were produced from the unidirectional prepregs with various parameters.

2.4 Impact on Composite Plates

The subject of impact on composite structures has been studied especially during last decade by many researchers. Review articles on the subject covering contact laws, impact dynamics, stress analysis, damage initiation and propagation, failure modes, damage tolerance, and improvements in damage resistance and tolerance can be found in literature (Abrate, 1991, 1994, 1998; Cantwell & Morton, 1991).

Impact event is generally divided into three main categories as low velocity, high velocity and hyper velocity impact. However, there is no clear definition to determine the limits of these categories. Sjoblom et al. (1988), Shivakumar (1985) and Cantwell & Morton (1991) have defined the low velocity impact as up to 10 m/sec. However, Abrate

(1991) in his review article determined the low velocity impact as the impactor speed is less than 100 m/sec. Liu & Malvem (1987) and Joshi & Sun (1987) have suggested that type of impact can be classified according to the damage occurrence. Low velocity is characterized by delamination and matrix cracking while high velocity is by penetration induced fiber breakage.

When the impact event leads to complete pulverization of the projectile and target materials, in the immediate vicinity of the contact, then the impact event is named as hyper velocity impact. Generally, hyper-velocity impacts are said to occur for impactor speeds larger than 1 km/sec (Abrate, 1991).

In the current study, although penetration or perforation took place, all of the velocities were less than 5 m/sec in experiments. Because of the confusion in determination of impact, the first definition by Cantwell & Morton (1991) mentioned above is selected. It means, all of the experiments in this study were assumed as low velocity impact. The main objective of the study is to improve the energy absorption capacity of laminated composite plate not determination of limits of impact event.

2.5 Failure Modes

The damage modes can be described as macroscopic and microscopic viewpoint. In macroscopic viewpoint, the damage modes due to impact can be classified as indentation, penetration, perforation, and bending fracture. **Indentation** is damage of matrix smash in the impacted zone. **Penetration** is sticking and **Perforation** is making a hole into composite plate by impactor nose. Penetration and perforation refers to the damage surrounding the contact point and the hole. **Bending fracture** has damage shape more like a line. In microscopic viewpoint, the damage modes can be specified as matrix cracking, delamination and fiber breakage.

Delamination is the debonding between adjacent laminas. They significantly reduce the strength of the laminate. Experimental studies report that delaminations occur only at interfaces between plies with different fiber orientations. The delaminated area resulting

from point nose impact appears generally in a peanut shape for laminated composite with its longitudinal axes oriented in the direction of the fibers in the lower ply at that interface. In general, once a delamination is initiated from a critical matrix crack, it can grow much more extensively along the fiber direction than in the transverse direction of the bottom layer at the interface. Hence, delamination appears to be in a peanut shape in laminated composites. The delaminations in a laminated composite are illustrated schematically in Figure 2.2. If two adjacent plies have the same fiber orientation, no delamination will be introduced at the interface between them (Abrate, 1998).

Two simple models (Liu, 1988 and Lesser & Filippov, 1991) have been put forward to explain why delaminations appear when laminates are subjected to localized load. Both approaches are based on the fact that the laminate is made up of several orthotropic layers. Each layer tends to deform in a particular way and transverse normal and shear stresses applied at the interface constrain the lay-up to behave as one plate. When this interlaminar stresses become too large under concentrated contact loads delaminations are introduced. The orthotropic behavior of each ply and the mismatch in their bending stiffnesses is thought to be the basic cause of delaminations, and the study of these mismatch yields important information regarding the locations, orientations, and size of delamination of laminate.

The damage process is initiated by matrix cracks which then induce delaminations at ply interfaces. In general, two types of matrix cracks are observed: tensile cracks (bending cracks) and shear cracks (Figure 2.3). Tensile cracks occur when in plane normal stresses exceeded the transverse tensile strength of the ply. Shear cracks are at an angle from the midsurface which indicates transverse shear stresses play a critical role in their formation.

Matrix cracks are first induced either in the top layer or in the bottom layer depending on the thickness of the laminate. With thick laminates, matrix cracks are first layer because of the high localized contact stresses. Damage progression is in such laminates from the top to down (Figure 2.4 a). In thin laminates, matrix cracks resulting

from bending stresses are in the bottom layer of the laminate and lead to a reversed pine tree pattern shown in (Figure 2.4 b).

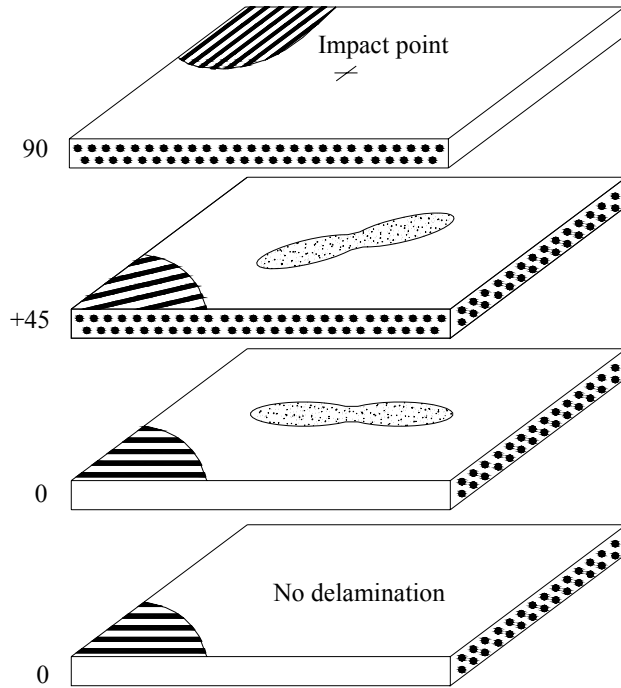


Figure 2.2 Delaminations in a laminated composite

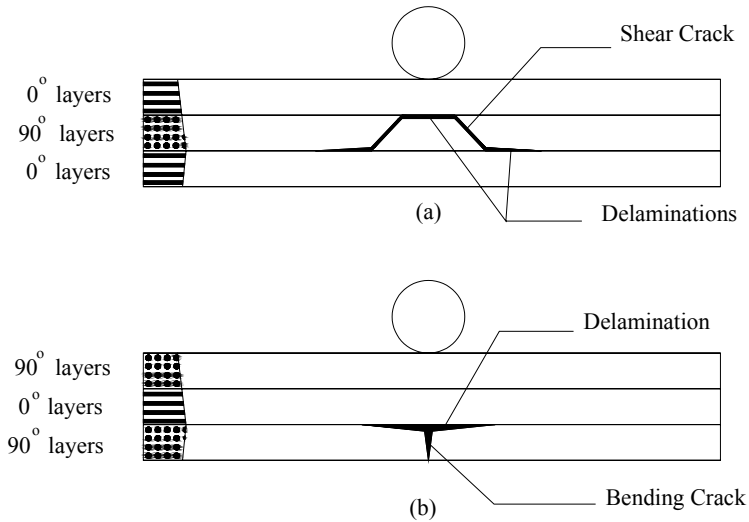


Figure 2.3 Delamination induced by a) inner shear cracks. b) a surface bending crack

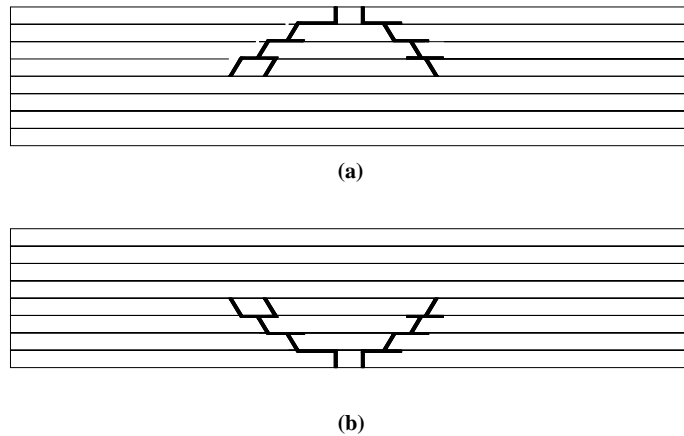


Figure 2.4. Pine tree (a) and reverse pine tree (b) damage patterns

2.6 Impact Testing Methods

During the first part of the 20th century a metallurgist named Izod investigated an impact test for determining the impact fracture toughness of various metals. The test later modified by Charpy. These test methods proved to be very useful, providing reliable, qualitative impact data until the early 70's. Within last two decades advances in strain gage technology, data acquisition, and computers have allowed impact test results to become more quantitative in nature (e.g. force and energy data in digital form).

To determine the impact response and damage mechanisms of composite materials several impact methods have been developed. It is very important to select a test method appropriate to the actual impact conditions. For example, an impact from a debris flying from the runway to the aircraft component is a situation of small mass and high velocity impact and best simulated using a gas gun. Another example, a tool is dropped on a structure, is a larger mass and low velocity impact and mostly simulated using a drop weight tester.

Gas gun impact testing is used for ballistic tests. A projectile pushed by compressed air travels through the gun barrel and passes a speed-sensing device and impacts to the target. A simple speed-sensing device consists of a single light-emitting diode (LED)

and a photo detector. The projectile, which has a known length, interrupts the light beam, and the duration of that interruption in signal produced by the sensor is used to calculate the projectile velocity.

With conventional drop weight impact tests, the specimen is impacted in a direction normal to its surface. Heavy impactors are usually guided by a rail during their free fall from a given height. Usually, a sensor activates a device designed to prevent multiple impacts after the impactor bounces back up. Next section gives the details of drop weight tester and test procedure.

CHAPTER THREE

EXPERIMENTAL METHOD

3.1 Introduction

This chapter deals with the production method of the composite laminates consist of unidirectional or woven laminas, impact testing on the laminates. All of the composite plates were prepared from prepreg tapes which have unidirectional E-glass fibers and epoxy resin. To obtain same fiber volume fraction and desired cell size and shape in the composite layers, the prepreg tapes were cut into strips, weaved and some of them stitched by hand. 1 mm glass- epoxy prepreg tapes were used as the stitching thread.

Stacked composite plate is put in a bag for curing under desired temperature and pressure. Cured composites cut into specimens and impact testing is performed by using a drop testing machine. All the data are collected and discussed at the end of this chapter.

3.2 Material

All composite laminates constructed for this study were made from unidirectional fiberglass tape pre-impregnated (prepreg) with an epoxy matrix and can be seen in Figure 3.1. The prepreg tape came on a 300 mm wide roll with a total length of 66 m. When not being used, the prepreg roll must be sealed inside a plastic bag and stored in a freezer. The sealed plastic bag containing the prepreg tape was removed from the freezer and allowed to warm for approximately one hour prior to use. Leaving the prepreg tape in the sealed plastic bag while warming prevented condensation on the composite material.

3.3 Manufacturing

Two types of composites which were laminated plates with consist of unidirectional laminas with various orientation angles and laminated plates with two dimensional woven laminas were manufactured. Some of the composite laminas were stitched with thread.



Figure 3.1 Unidirectional prepreg tape

3.3.1 Laminated Plates with Unidirectional Laminas

The laminated composite plates were constructed from twelve unidirectional prepreg tapes which have dimensions of 300 mm x 300 mm with various fiber orientation angles. The prepreg tape roll which has 300 mm short edge is shown in Figure 3.1 has unidirectional fibers along the long edge. For this reason, there is no problem with cutting 0° and 90° plies from the prepreg tape. However, the cutting of angled prepreg tapes is not as easy as that plies. Special tailoring is required for the angled plies. Figure 3.2 gives an example of tailoring method for $\theta = 45^\circ$. The length of the unidirectional prepreg can be calculated by using geometry. The length of the tape was found as approximately 461 mm. The dashed lines are used for determining the cutting edges from the unidirectional tape. The pieces, labeled A and B, are taken and the leftover pieces are thrown away. The piece labeled B is used to fill the gap to create 300 mm x 300 mm, 45° angled ply. The fiber continuity is important when creating the angled plies. Only certain pieces of the pattern can be used to fill gaps.

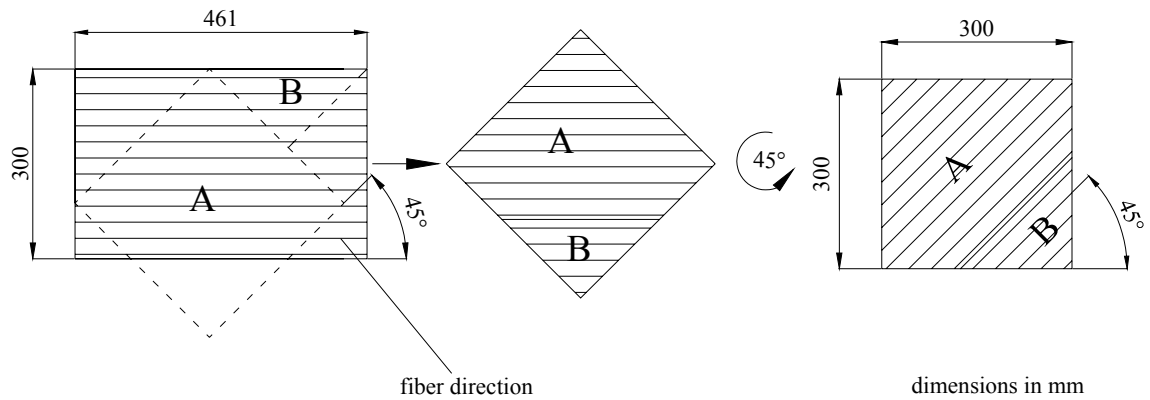


Figure 3.2 Preparing the angled ply from the unidirectional prepreg

The plies then stacked together with desired sequences to create the laminated plates. Figure 3.3 presents the construction of $[\theta/0]_6$ composite using unidirectional prepregs which have θ° and 0° fiber orientation angles. They are unsymmetric and have dimensions of 300 mm x 300 mm.

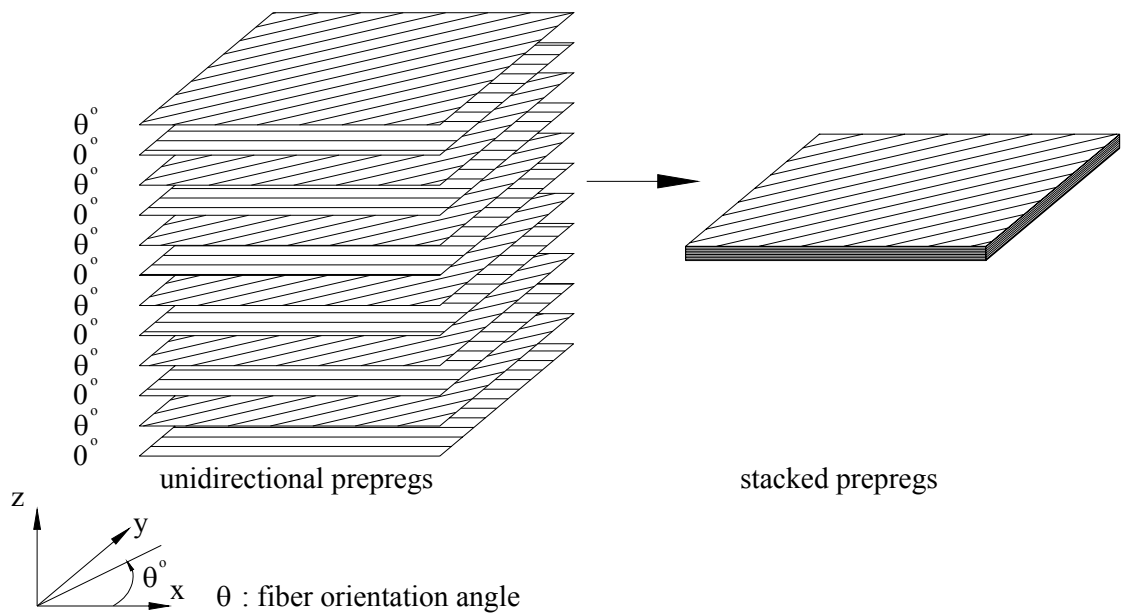


Figure 3.3 Construction of a composite plate with composite layers

3.3.2 Two Dimensional Woven Laminas

The two dimensional woven plate consisted of six pieces of plain weave prepreg. In order to obtain similar fiber volume fraction for various cell sizes, the woven plates were manufactured from the prepreg tape rather than from prefabricated woven fabric. Each of the woven is weaved by hand. As an example, the manufacturing method of a woven lamina which consists of 25.4 mm warp and 25.4 mm fill strips is presented below:

The strips are cut from the prepreg by dimension of 25.4 mm and 360.0 mm . The long edge of the strips must be parallel to the fiber direction of the prepreg. Woven pattern is drawn on a blank paper which has been stuck on the aluminium base with a tape. A transparent nylon layer is stuck on the aluminium base and the paper as can be seen in Figure 3.4-a,b. The strips are placed side by side on the nylon layer with assistance of the warp direction of the drawn paper (Figure 3.5-a). The strips consist of unidirectional fibers and a paper in back of them. The papers of the end of the strips are removed and the start points of the strips are stuck on the nylon layer by using a tape as can be seen in the Figure 3.5-b. In order to prevent the fibers to damage during the weaving process, the paper backing should be removed from strips only required parts.

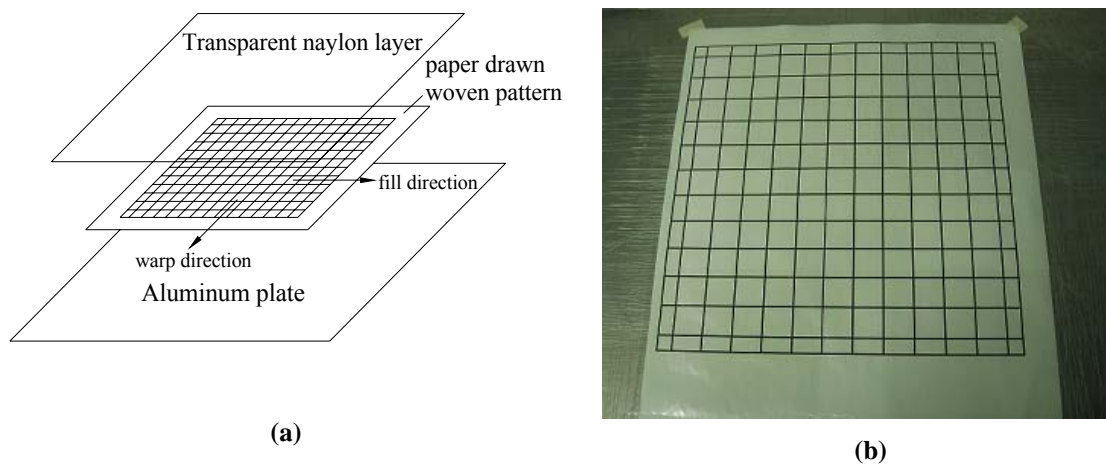


Figure 3.4 (a) Drawing and (b) photo of Aluminum plate with woven pattern paper and transparent nylon layer stuck on.

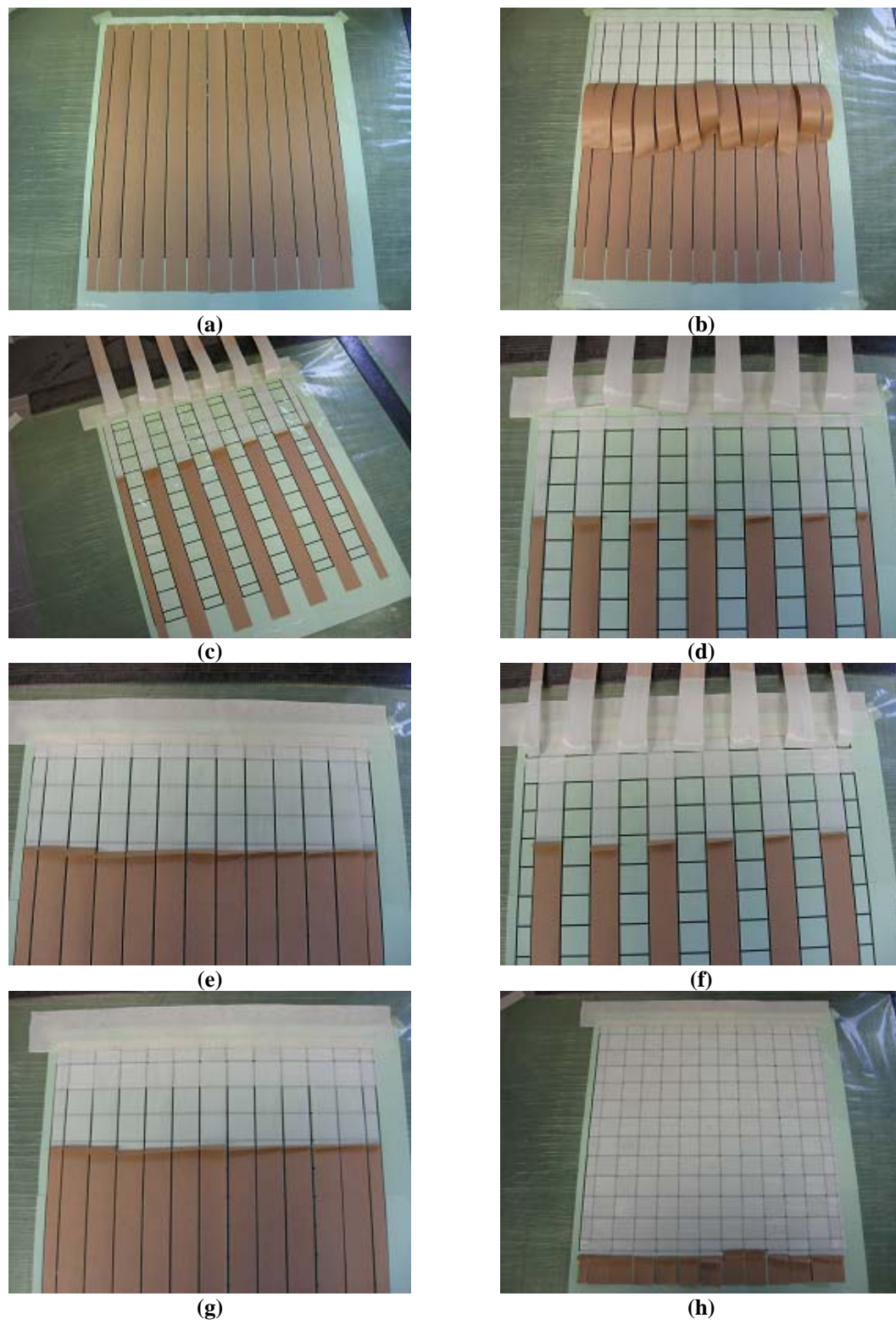


Figure 3.5 Production method of a woven layer

If the warp strips are numbered consecutively, the even numbered strips are lift up (Figure 3.5-c) and a fill strip is placed on the odd numbered strips (Figure 3.5-d). The even numbered strips then are released (Figure 3.5-e). Following, the odd numbered strips are lift up and a fill strip is placed on the even numbered strips (Figure 3.5-f). The even numbered strips then are released (Figure 3.5-g). The weaving procedure continues until to finishing point of the warp strips as can be seen in Figure 3.5-h. Finally, The woven prepreg is removed from the transparent nylon layer after cutting the excessive warp strips. Figure 3.6 a and b gives the photos of woven prepreg which have 25.4 mm and 6.4 mm wide strips, respectively. The woven prepreps should be sealed inside a plastic bag and stored in a freezer. The sealed plastic bag containing the woven prepreg is removed and allowed warm for approximately one hour prior to prepare the curing bag which will be mentioned after. Leaving the woven prepreg in the sealed plastic bag while warming prevented condensation on the composite material. The six woven layers with identical cell size are then stacked together with cell boundaries well aligned through the thickness. The stacked woven prepreps are put into the vacuum bag. Figure 3.7 shows the stacked woven composite plate before putting the bag for curing.

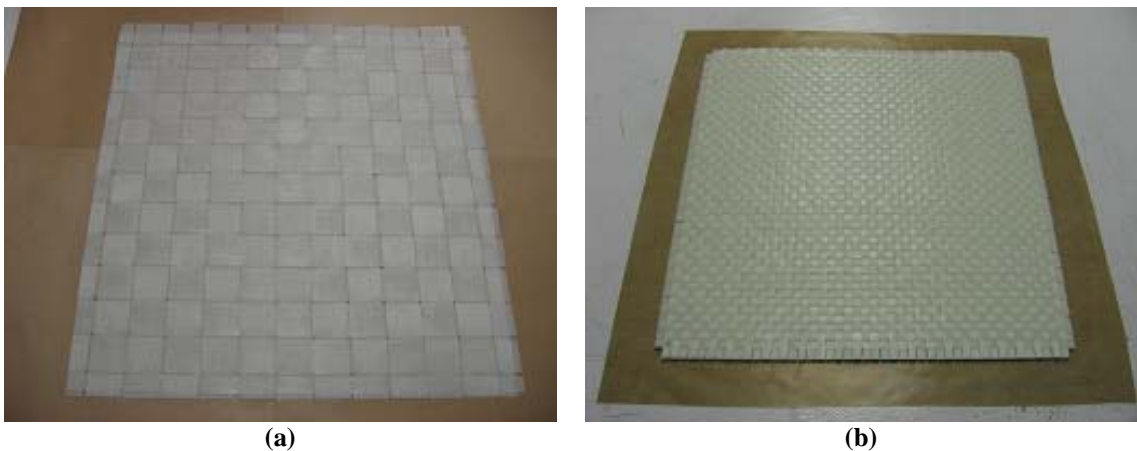


Figure 3.6 Two woven composite with different cell sizes

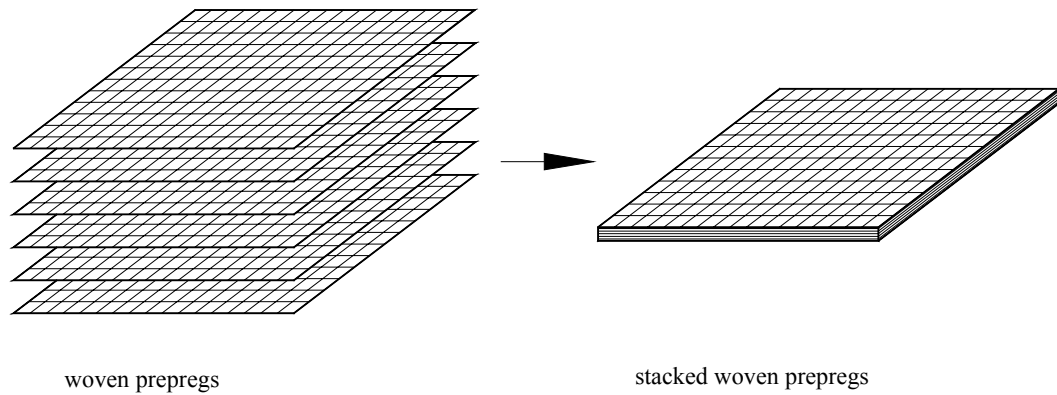


Figure 3.7 Construction of a composite plate with woven composite layers

3.3.3 *Stitched Laminates*

In order to investigate the stitching effect on impact behavior of the composite materials, some of the composites preregs were stitched after stacking together by hand using a needle. A special apparatus as seen in Figure 3.8 was used for stitching. 1 mm glass- epoxy prepreg tapes were used as the stitching thread. The stitching pattern has square grids of 12.7 mm x 12.7 mm with the stitching threads across the diagonal of the grids. Stitched plates are then put into the curing bag.



Figure 3.8 Construction of a composite plate with woven composite layers

3.4 Curing

Before curing, the prepared composite plate was put into a vacuum bag. The bag includes a strong polyester film having a good heat resistance, bleeder made of a thick cloth with a good absorption of resin, porous Teflon and composite plate. Porous Teflon is a layer which does not stick the composite plate and allows passing resin from composite to bleeder. The bag is closed by using a bag sealant tape. The bag construction is shown in Figure 3.9.

The composite laminates were cured in a hot press without vacuum condition. The pressure value was 0.24 MPa for low pressure and 2.88 MPa for high pressure. The temperature was increased from the room temperature to 160 °C by increasing ten degrees per minute. It was hold at this temperature and pressure for 45 minutes. Following, the temperature was decreased to room temperature by increasing rate, and finally pressure was released. The cure cycling is shown in Figure 3.10.

The cured composite plate was extracted from the bag. The thickness, the density and the fiber volume fraction of all of the composite plates produced should be almost equal. Thickness can be measured by a micrometer. The density can be calculated dividing the weight to the volume of the composite. To find the fiber volume fraction the epoxy absorbed by bleeder should be known. To find the epoxy absorbed by bleeders, the bleeders were weighted before and after curing with sensitive weighting device. The absorbed epoxy was found the weight differences of these values. The exact fiber volume fraction of the cured composite material calculated by the assistance of the absorbed epoxy value was found as 56%.

The specimen edges are drawn on the cured composite plate by using a permanent board marker. Figure 3.11-a gives a drawn and numbered composite plate. The plates are cut into specimens with a diamond blade circular saw. The specimens which dimensions are 100 mm x 100 mm are given in Figure 3.11-b.

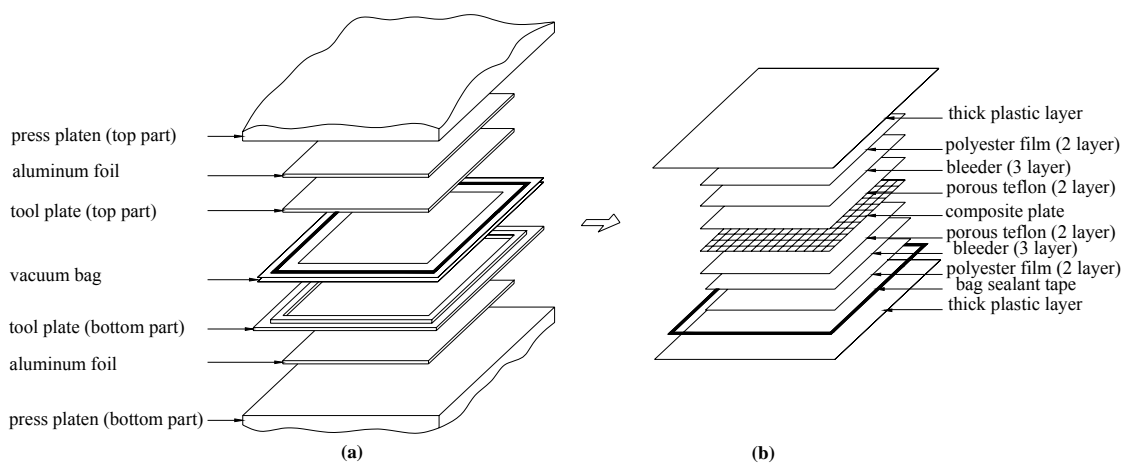


Figure 3.9 (a) Detail view of tool plate designed, (b) vacuum bag preparation for curing of the composite plate

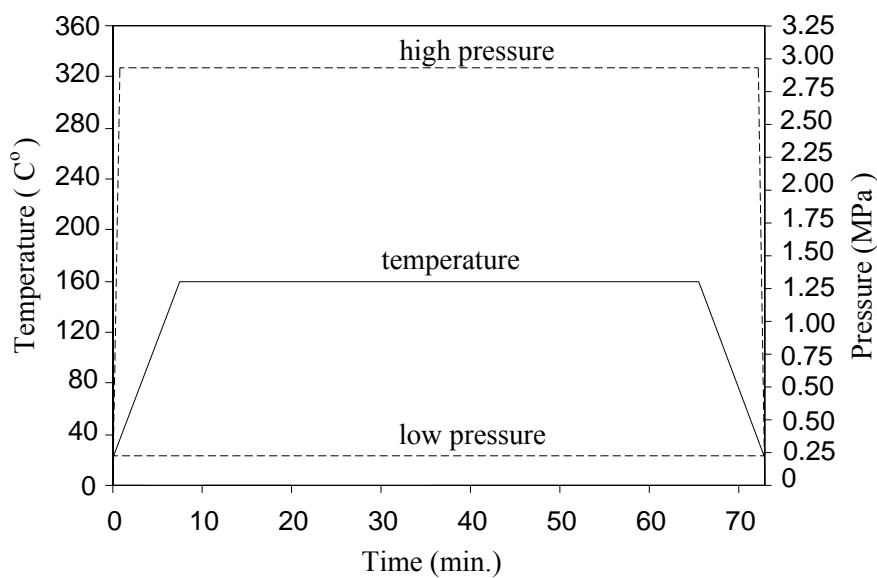


Figure 3.10 Cure cycle for glass-epoxy composite processing

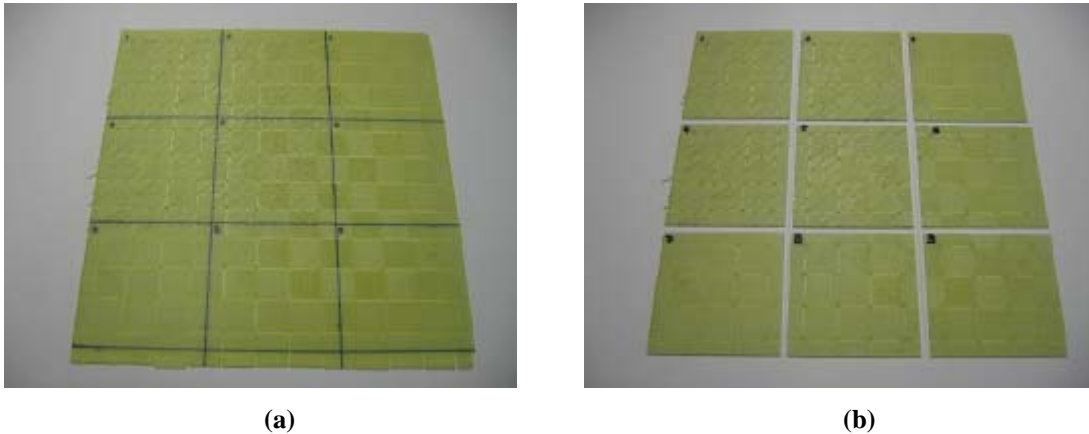


Figure 3.11 (a) Drawing and numbering of cured composite plate (b) cutting of the composite plate

3.5 Design of the Composite Plate

In this thesis, following design parameters are investigated:

- stacking sequence,
- pressure,
- gaps between the cells,
- cell size,
- stitching and
- the angle between warp and fill strips.

There were lots kind of specimen prepared. In writing, it is very difficult to define the specimen specifications. For this reason, an easy special code is used. Some examples are given below. The code of the laminated specimen is same as in the literature (Gibson, 1994).

$$[\theta/0]_n^{wxf}, S[\theta/0]_n^{wxf}, S[\theta/0]$$

$[\theta/0]$: woven structure has a θ° angle between warp and fill strip

$[\theta/0]$: laminated structure has a θ° angle between adjacent layers

S: stitched plate

n : number of layers.

w : wide of the warp strips in mm.

f : wide of the fill strips in mm.

The nomenclature of the woven composite is given in Figure 3.12. The produced specimens, numbers of specimens, their thickness and density can be found in Table 3.1.

Table 3.1 The specimen produced for impact testing

Specimen	Thickness (mm)	Density (gr/cm ³)	Number of specimen
$[30/0]_6$	2.89	1.79	6
$[15/0]_6$	2.89	1.76	5
$[90/0]_6$	2.82	1.76	6
$[90/0]_6^{25.4 \times 25.4}$	2.84	1.68	5
$[90/0]_6^{12.7 \times 12.7}$	2.92	1.71	5
$[90/0]_6^{6.4 \times 6.4}$	3.20	1.53	5
$S[90/0]_6$	2.89	1.83	3
$S[90/0]_6^{25.4 \times 25.4}$	2.84	1.75	4
$S[90/0]_6^{12.7 \times 12.7}$	2.92	1.76	4
$S[90/0]_6^{6.4 \times 6.4}$	3.20	1.63	4
$[60/0]_6^{12.7 \times 12.7}$	2.95	1.66	8
$[45/0]_6^{12.7 \times 12.7}$	3.09	1.54	9
$[30/0]_6^{12.7 \times 12.7}$	2.87	1.65	9
$[15/0]_6^{12.7 \times 12.7}$	2.82	1.67	5

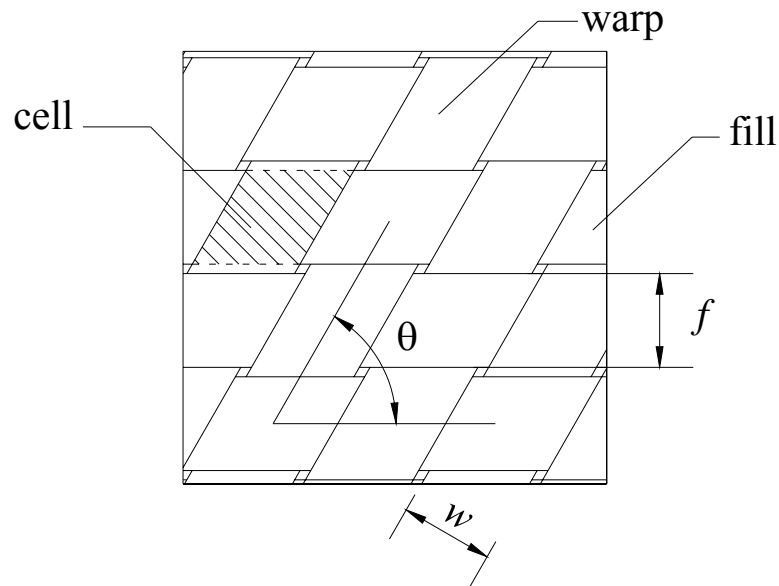


Figure 3.12 Nomenclature of woven composites.

3.6 Impact Testing

The composite plates were tested by using a DYNATUP GRC 8200 drop weight testing machine shown in Figure 3.13. This machine consists of three main parts which are dropping crosshead include drop weight box, impactor rod and force transducer, two steel guide rails for traveling the dropping part smoothly, and the steel frames for fixing the specimen. The crosshead is held by a height adjustment latch. When the crosshead is released, it slides with negligible friction along the guide rails. The diameter of the steel impact rod has a hemispherical nose at the end is 12.7 mm.

The force transducer has a capacity of 22.24 kN mounted between steel rod and the crosshead. The total mass of the dropping part is 5.03 kg. However to increase the impact energy, extra 1 kg was added in the crosshead box. It means that the total dropping mass in this study was 6.03 kg and held constant. To change the impact energy, the dropping height was increased or decreased. A pneumatic air cylinder was used for arresting rebounds. All of the edges of the specimen were fixed by a steel frame can be seen in Figure 3.14. The dimensions of the specimen after extracting the area of the fixing part were 76 mm x 76 mm.

The contact – impact load history is taken from the force transducer by a computer. The computer has a software program based on Newton's second law and kinematics converted the time-load history to velocity and displacement histories. The instantaneous impact velocity right before the impact is needed for calculating process is detected by an infrared emitter detector.

The force values at each time step, $F(t)$, are recorded at a sampling rate of $25 \mu s$ by computer. The acceleration, $a(t)$, could be calculated by dividing the $F(t)$ values to total mass of the crosshead, m .

$$a(t) = F(t)/m \quad (3.1)$$

The velocity values, $v(t)$, are calculated by integrating the acceleration, $a(t)$, as can be seen in Equation (2.2). In this equation, the initial velocity v_i can be taken the impact velocity value detected by the infrared emitter detector.

$$v(t) = v_i + \int_0^t a(t) dt \quad (3.2)$$

The deflection history, $\delta(t)$, can be found by integrating the velocity, $v(t)$.

$$\delta(t) = \int_0^t v(t) dt \quad (3.3)$$

The relation between the force and the deflection determined by the function, $F(\delta)$, which is used for finding the absorbed energy, E_a , given in Equation (3.4).

$$E_a = \int_0^{\delta_i} F(\delta) d\delta \quad (3.4)$$

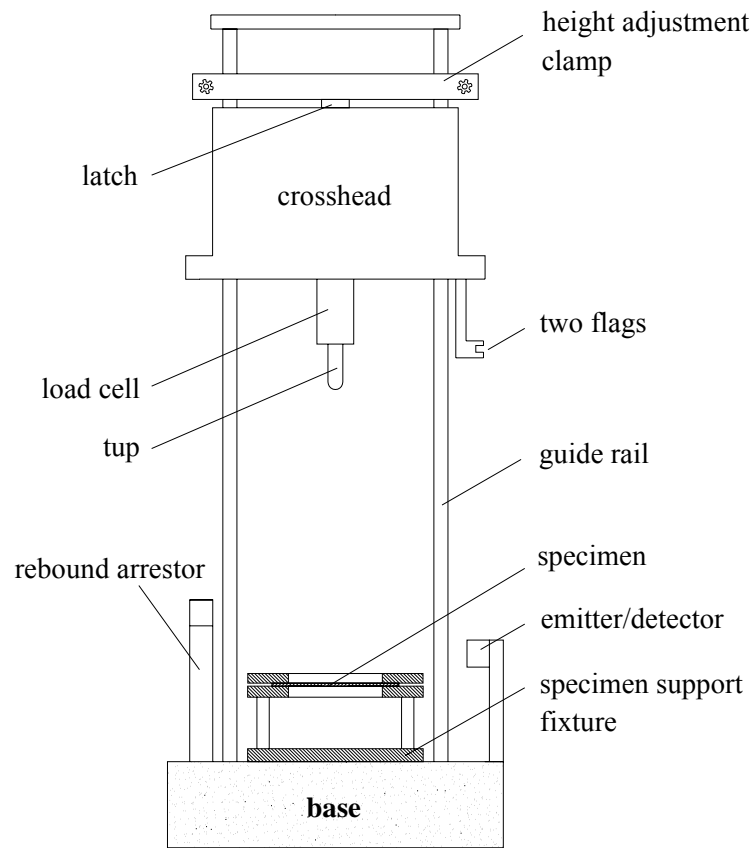


Figure 3.13 Schematic illustration of drop weight impact machine

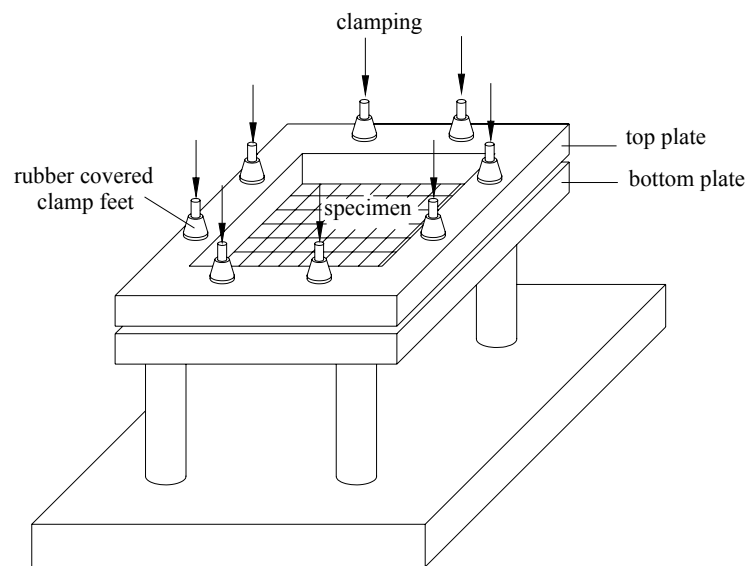


Figure 3.14 Schematic illustration of clamping fixture

3.7 Analysis of the Impact Test Results

In order to understand the impact behavior of the composite plates, the impact energy was gradually increased for consecutive tests until perforation took place. The instrumented impact test machine gives the time versus load, velocity, deflection and absorbed energy histories. Three special tests results including *Rebounding*, *Penetration* and *Perforation* situation are given in Figure 3.15.

Contact force- time curves for the three situation are shown in Figure 3.15-a. As can be seen in this figure *maximum contact force*, which can be defined as the maximum reaction force applied by the specimen to the impactor nose, increases with increasing impact energy. The penetration and perforation situation have similar maximum contact force. The *contact duration*, which can be determined as the contact time between impactor nose and the specimen, decrease with increasing impact energy. At the situation of rebounding the force reaches the zero and the curve has a mountain-like shape. For penetration and especially perforation situation the force does not reach zero immediately after the descending section of the curve and remains nearly constant value. The main result of this behavior is the friction between impactor nose and the specimen.

Figure 3.15-b gives the information about the velocity histories for three main situations. The velocity values decrease after the first contact. In the rebounding situation the velocity has negative values indicating the up direction motion of the impactor. It means the impactor reach has positive velocities until the maximum deflection of the specimen. After the maximum deflection the specimen pushes the impactor along the up direction. However, at the penetration situation the velocity has only few negative values indicates little amount of rebound after sticking. At the perforation the velocity does not reach zero value. After a certain value it decreases linearly because of the friction during the post perforation motion. The beginning point of the linear part of velocity-time curve can be taken the beginning of the perforation. Absorbed energy for perforation can be calculated until the time of the beginning of the

linear part. This method named as velocity method and detailed information can be found in Coppens' thesis (2004).

The deflection- time curves of three special cases are shown in Figure 3.15-c. At the rebounding curve, the deflection decreases after the maximum deflection and reaches the zero value which depicted that the specimen reaches the initial position. The maximum deflection of the composite remains constant value for the penetrated specimen. Because, the velocity value of the impactor reaches to zero at that point. In the situation of perforation the velocity does not reach zero. As a result of this the deflection continues to increase which indicates the motion of the impactor nose during the post perforation motion.

The absorbed energy versus time curves of the three special cases are given in Figure 3.15-d. The absorbed energy values are increased with increasing the time until a certain value. For rebounding situation, the absorbed energy decreases with increasing time and reach a constant value. The reason of this decreasing is the specimen expends some of the absorbed energy for pushing the impactor along the down direction. The penetrated specimen absorbs all of the impact energy. While the time increase the absorbed energy increase at the situation of the perforation. The absorbed energy calculated includes the friction energy after perforation takes place. In order to find the absorbed energy for perforation, the energy consumed for friction must be extracted the total absorbed energy given by computer program.

The absorbed energy during the impact event can be found by using the force-deflection curves. Figure 3.16 shows three typical curves: *rebounding*, *penetration* and *perforation*. Returning toward the origin of the diagram after descending from the maximum force or the peak force indicates the rebounding of the impactor from the specimen surface after impact. Stopping almost right after the impact force becomes zero, implying the penetration of the impactor into the composite specimen. The forces reach a relatively constant value at the very end due to the friction between the impactor and the composite specimens in the situation of perforation.

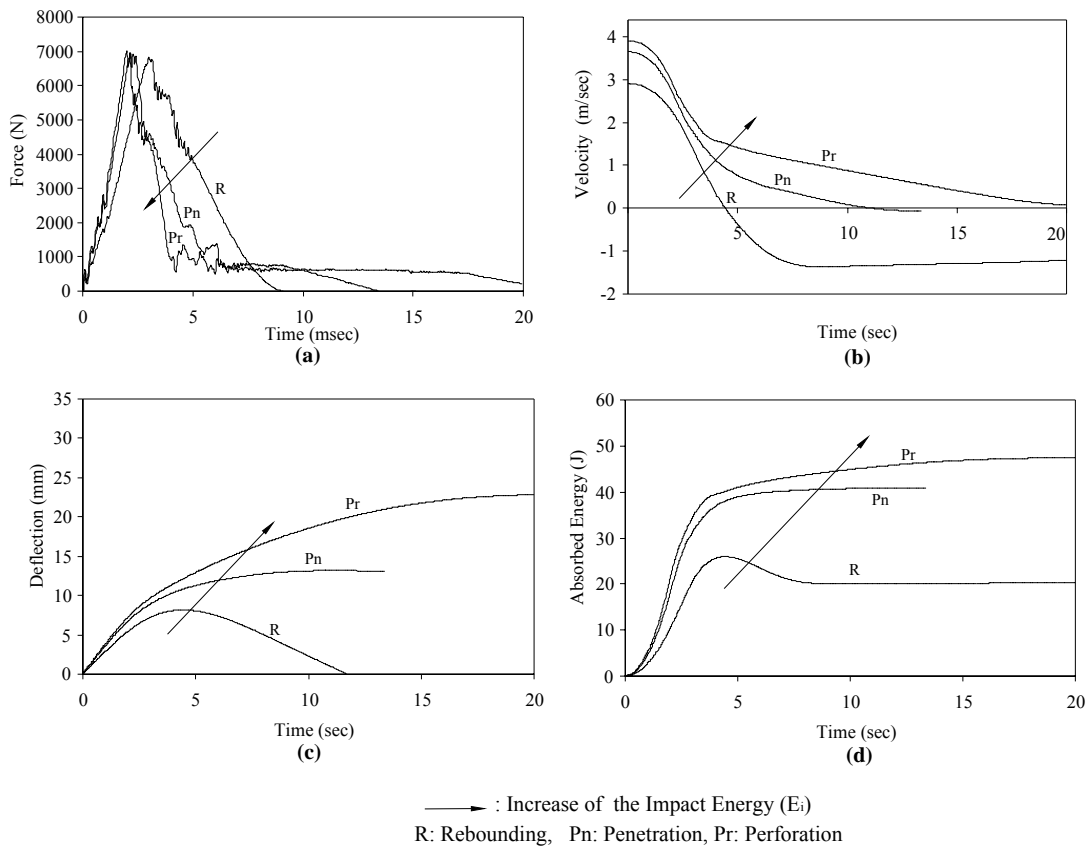


Figure 3.15 Time versus (a) Force, (b) Velocity, (c) Deflection, (d) Absorbed energy curves

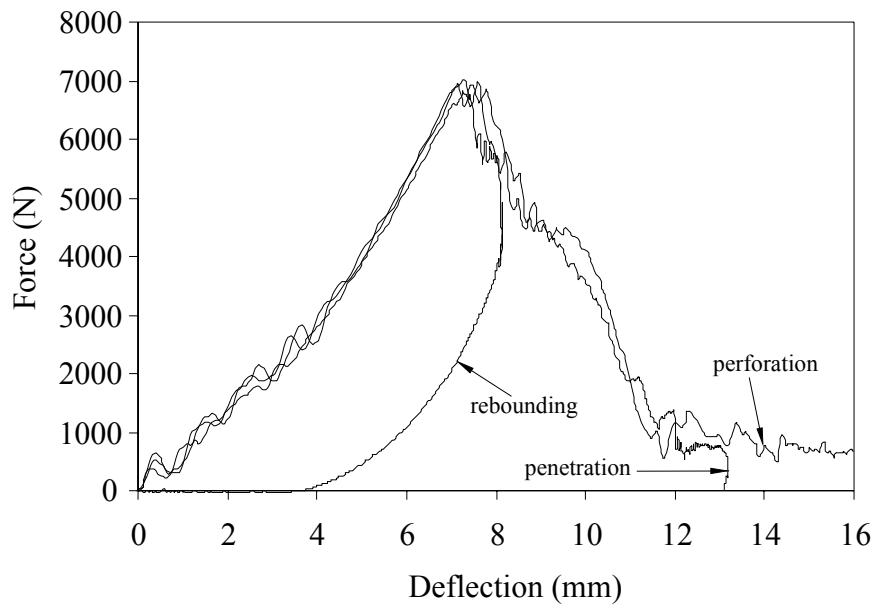


Figure 3.16 Typical force-deflection curves of the composite plates subjected to impact loading

3.8 Absorbed Energy

The impact energy E_i during an impact event is considered as the energy introduced to a specimen from the impactor. It is equal to the potential energy of the impactor in the drop-weight impact testing and can be expressed as

$$E_i = mgh + mg\delta_{\max} \quad (3.5)$$

where h is the initial height of the impactor above the specimen surface and δ_{\max} is the maximum deflection of the specimen surface from its initial position. During the impact event, the impact energy is transformed into (a) the absorbed energy E_a in terms of specimen damage and friction between the impactor and the specimen, (b) the non-conservative energy E_{nc} in forms of vibration of the testing system and the specimen and (c) the residual kinetic energy of the impactor, i.e.

$$E_i = E_a + E_{nc} + \frac{1}{2}mv^2 \quad (3.6)$$

where v is the velocity of the impactor, with respect to the specimen, rebounding from the specimen or perforating through the specimen. Combining Eqs. (3.5) and (3.6), it yields

$$mgh + mg\delta = E_a + E_{nc} + \frac{1}{2}mv^2 \quad (3.7)$$

Right before contact-impact takes place, $\delta = 0$, $h = 0$, $E_a = 0$ and $E_{nc} = 0$, Equation 3.7 reduces to

$$mgh = \frac{1}{2}mv^2 \quad (3.8)$$

This equation shows that the potential energy of the impactor is completely transformed into kinetic energy. Once impact takes place, the composite specimen starts

to consume the impact energy. When the impact energy is low, the impactor rebounds from the specimen surface with a velocity opposite to the impacting direction. As the impact energy increases, penetration takes place and the impactor sticks with the specimen, i.e. $v=0$. Eq. (3.7) then becomes

$$mgh + mg\delta = E_a + E_{nc} \quad (3.9)$$

Apparently, the impact energy is consumed by forming the damage in the composite specimen and dissipated away by vibrating the testing system and the specimen. As the impact energy continues to increase, perforation eventually takes place in the composite specimen. In that, the excessive impact energy is used to drive the impactor through the specimen with a velocity as described in Equation 3.7.

The absorbed energy of a composite specimen can be calculated from the area enveloped by the closed curves for non-perforated specimen (Figure 3.17-a) and area bounded by the associated force-deflection curve and the horizontal axis for penetrated or perforated specimen (Figure 3.17-b). In order to identify the penetration threshold of a specimen, the pure-friction portion, i.e. the nearly constant tail portion of the descending section of the force-deflection curve, is neglected. A line tangent to the end portion of the descending section is then added to the curve as shown in Figure 3.17-b. The penetration threshold of the composite specimen is equal to the modified mountain-shaped area. This method is called extended method (Ataş, 2004; Coppens, 2004). The absorbed energy is used for drawing the energy profile of the composite.

3.9 Energy Profile

An energy profile is a diagram showing the relationship between impact energy and absorbed energy. It consists of all testing results and an equal energy line for comparison.

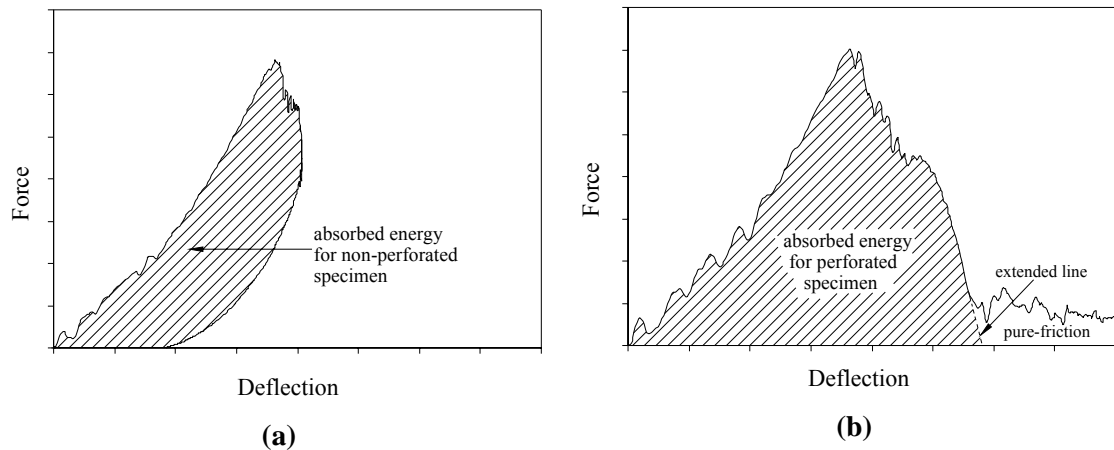


Figure 3.17 Force- deflection curves for calculating the absorbed energy for (a) non-perforated specimen, (b) perforated specimen

The energy profile of a composite is given in Figure 3.18 as an example. It can be roughly divided into three zones. The absorbed energy of each of the first four experimental data points are smaller than the corresponding impact energy so each data point is located below the equal energy line. The excessive impact energy is retained in the impactor and is used to rebound the impactor from the specimen surface at the end of the impact event.

As the impact energy increases, the data points become closer to the equal energy line. For point 5, the impact energy is almost equal to the absorbed energy. It indicates that the impactor almost penetrates into the composite. The impact energy required to cause penetration is called *the penetration threshold*. The small difference between the impact energy and the absorbed energy for point 5 is likely to be attributed to the non-conservative energy (E_{nc}) in forms of vibration of the testing system and the specimen. As the impact energy continues to increase, the corresponding absorbed energy increases linearly and data points e.g. points 6, 7 and 8, travel on the equal energy line called as equal energy interval. However, this interval can be formed by only one data point related to the thickness of the composite and diameter of the impactor nose.

At the end of the interval the impactor nose penetrates the composite entirely and following perforates. After the data point 8 which is named as *the perforation threshold*, absorbed energy does not increase as the impact energy continues to increase. The impact energies of those data points, e.g. 9, 10 and 11, are again higher than the corresponding absorbed energies. The excessive impact energies in these three cases are retained in the impactor for post-perforation motion.

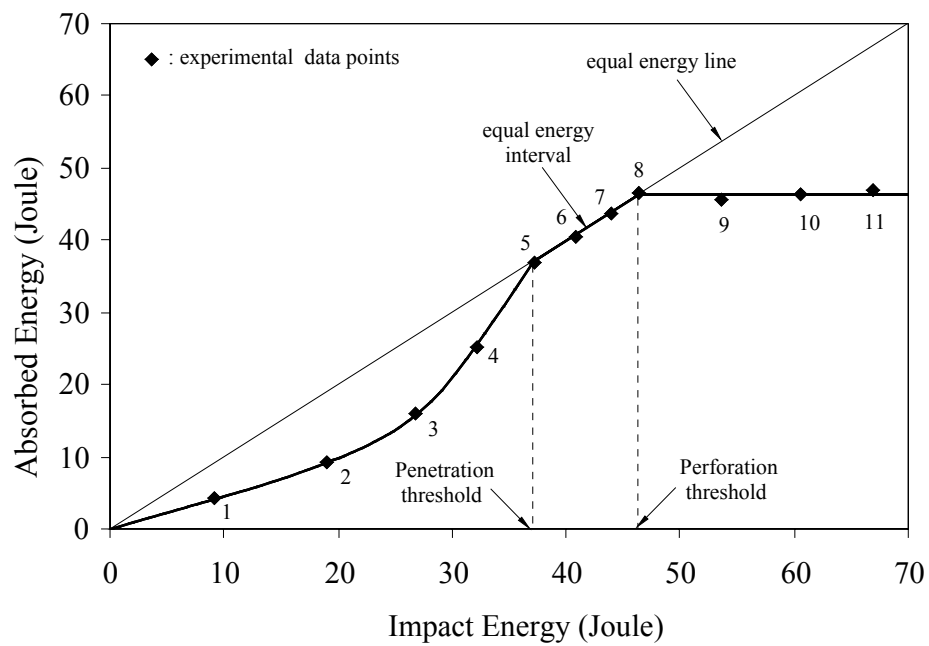


Figure 3.18 Energy profile of a composite plate under impact loading

CHAPTER FOUR

NUMERICAL PROCEDURE

4.1 Introduction

The numerical investigation is performed in current study by using the 3DIMPACT code. The program based on transient dynamic finite element analysis capable to solve response of laminated composite plate subjected to transverse impact loading by foreign object.

The code is capable to calculate

- the history of the contact force between impactor and the composite,
- displacement and velocities of the impactor,
- displacement and velocity histories through the composite plate and
- delamination in the interfaces of the composite plate.

Moreover the code allows finding delamination in adjacent layers by means of suitable stress analysis and damage criteria.

An 8-point brick element with incompatible modes is used in the analysis and the direct Gauss quadrature integration scheme is applied through the element thickness to account for the change in material properties from layer to layer within the element. The Newmark scheme is adopted to perform time integration from step to step. A contact law incorporated with the Newton-Rapson method is used to calculate the contact force during impact.

The information regarding finite element procedures was given extensively in paper prepared by Wu & Chang (1989). In the failure analysis, a matrix failure criterion and an impact- induced delamination criterion were proposed for predicting the initial impact damage and extent of the delaminations due to impact, respectively.

4.2 Stress Analysis

The analysis is based on a three dimensional linear elastic theory. The materials in each layer are considered homogeneous and orthotropic. The equilibrium equations at instant time in a variational form can be written as (Zienkiewicz, 1977)

$$0 = \int_{\Omega} w_i \rho u_{i,tt} dv + \int_{\Omega} e_{ij} E_{ijkl} \varepsilon_{kl} dv + \int_{\Gamma} w_i \sigma_{ij} n_j dA \quad (4.1)$$

where w_i are the arbitrary variational displacements, ρ is the density, $u_{i,tt}$ are the accelerations ($u_{i,tt} = \partial u_i / \partial t^2$), e_{ij} are the strains from the arbitrary variational displacements, E_{ijkl} are the material properties of the laminate, ε_{kl} are the strains, σ_{ij} are the stresses, n_j is the outward unit normal vector on the plate surface, Ω is the entire plate volume and Γ is the surface of the plate.

The distribution of the contact force F between the impactor and the target must be known for solving the Equation 4.1. The projectile was modeled as an elastic body with a spherical nose. The contact force distribution can be determined according to loading and unloading process.

In case of loading, the contact force distribution can be determined using the Hertzian contact law (Hertz, 1982). The contact force F can be determined as

$$F = x\alpha^{1.5} \quad (4.2)$$

where α is the indentation dept can be expressed as the distance between the center of the projectile's nose and the mid-surface of the plate and x is the modified constant of the Hertz contact theory proposed by Sun & Yang (1980) and Tan & Sun (1985).

$$x = \frac{4}{3} \sqrt{r} \frac{1}{\left[\frac{(1-\nu_s^2)}{E_s} + 1/E_{yy} \right]} \quad (4.3)$$

where r , ν_s , and E_s are the local radius, the Poisson's ratio and Young's modulus of the impactor, respectively. E_{yy} is the transverse modulus (normal to the fiber direction) in the uppermost composite layer.

In case of unloading, the contact force can be determined as (Sun & Yang, 1980 and Tan & Sun, 1985).

$$F = F_m \left[\frac{\alpha - \alpha_0}{\alpha_m - \alpha_0} \right]^{2.5} \quad (4.4)$$

where F_m is the maximum contact force just before unloading, α_m is the maximum indentation corresponding to F_m , α_0 is the permanent indentation during the loading/unloading process. (Sun & Yang, 1980 and Tan & Sun, 1985) determined the following expression for α_0 ,

$$\begin{aligned} \alpha_0 &= 0 && \text{when } \alpha_m < \alpha_{cr} \\ \alpha_0 &= \alpha_m \left[1 - \left(\frac{\alpha_{cr}}{\alpha_m} \right)^{2/5} \right] && \text{when } \alpha_m \geq \alpha_{cr} \end{aligned} \quad (4.5)$$

where α_{cr} is the critical indentation, and is approximately 0.1 mm for glass-epoxy composite material.

An eight-node brick element incorporating incompatible modes was used in finite element calculations. A direct Gaussian quadrature integration scheme was adopted through the element thickness to account for the change in material properties from layer to layer within the element. Therefore, plies with different ply orientations could be grouped into an element, resulting in a significant reduction in computational time for three dimensional analyses.

4.3 Failure Analysis

The failure mechanism of composite laminates subjected to impact loading is very complicated phenomenon. Choi & Chang (1992) determined the mechanism in laminated composite with brittle matrix. In their description, the failure initiates with critical matrix cracks in a lamina of laminated composites subjected to transverse impact. Matrix cracks cause delamination in bottom or upper interface of the lamina depending on the position of the lamina in the laminate. Additional matrix cracks and delamination can occur subsequently in the other layers as the duration of the impact proceeds.

Critical matrix cracking criterion and impact induced delamination criterion are used in 3DIMPACT computer code. The initiation of matrix cracks and extension of delamination can be found by this code.

4.3.1 Critical Matrix Cracking Criterion

The matrix cracking criterion proposed by Choi et al. (1991) can be expressed as

$$\left(\frac{{}^n\bar{\sigma}_{yy}}{{}^nY} \right)^2 + \left(\frac{{}^n\bar{\sigma}_{yz}}{{}^nS_i} \right)^2 = e_M^2 \quad \begin{array}{l} e_M \geq 1 \text{ Failure} \\ e_M < 1 \text{ No failure} \\ \bar{\sigma}_{yy} \geq 0 \Rightarrow {}^nY = {}^nY_t \\ \bar{\sigma}_{yy} < 0 \Rightarrow {}^nY = {}^nY_c \end{array} \quad (4.6)$$

where the subscripts of x , y and z are the local coordinates of the n^{th} layer indicate the parallel and normal direction of the fiber in plane and the direction of the out of plane, respectively. S_i is the interlaminar shear strength, Y_t is the transverse tensile and Y_c is the transverse compressive strengths of the ply. The values of Y_t and S_i of the ply are determined in 3DIMPACT code from the empirical expression proposed by Chang & Lessard (1991) with the following forms:

$$\begin{aligned}
{}^n Y_t &= Y_t^0 \left(1 + A \frac{\sin(\Delta\theta)}{M^B} \right) \\
{}^n S_i &= S^0 \left(1 + C \frac{\sin(\Delta\theta)}{M^D} \right)
\end{aligned} \tag{4.7}$$

where $\Delta\theta$ is the minimum angle between the n^{th} ply or ply group and adjacent plies with different ply orientations, and M is the number of the layers in ply group that is considered. The ply group defines as the adjacent plies with the same ply orientations. Y_t^0 and S^0 are the transverse tensile strength of a $[0]_{ns}$ composite ($n \geq 6$) and the shear strength of a $[0]_{ks}$ composite ($k \geq 4$), respectively. A , B , C and D are the empirical parameters determined by Chang & Lessard (1991). $\bar{\sigma}_{yz}$ and $\bar{\sigma}_{yy}$ are the averaged interlaminar and in-plane transverse stresses, respectively, within the n^{th} ply which can be expressed as

$$\begin{aligned}
{}^n \bar{\sigma}_{yz} &= \frac{1}{h_n} \int_{t_{n-1}}^{t_n} \sigma_{yz} dz \\
{}^n \bar{\sigma}_{yy} &= \frac{1}{h_n} \int_{t_{n-1}}^{t_n} \sigma_{yy} dz
\end{aligned} \tag{4.8}$$

where t_n and t_{n-1} are the upper and lower interface of the n^{th} ply in the laminate and h_n is the thickness of the ply.

The initial impact damage is found, whenever the calculated averaged stresses in any one of the plies in the laminate first satisfy the criterion ($e_M = 1$) during analysis. The matrix cracks then propagates through the thickness of the ply group which contained the cracked ply. The time corresponding to the initial damage is determined as t_M . Delaminations can be induced from the locations of the matrix cracks along the interfaces of the ply group. As the time increases additional matrix cracks could be occurred in the other layers. Therefore, the criterion should continuously be applied to the other layers for determining any additional matrix cracks. If any additional matrix

cracking is found at any other layers during impact, then the impactor's velocity associated with the first matrix cracking is referred to as the impact velocity threshold which is the velocity required to just cause the initial impact damage of the laminate.

4.3.2 Impact Induced Delamination Criterion

Delamination propagation is very difficult and complicated, involving multiple dynamic crack propagation and delamination surfaces interaction. Hence, a semi-empirical model was proposed to estimate the extent of delamination in the composites resulting from impact.

Basically, there are two types of critical cracks initiating delamination resulting from impact (Choi et al., 1991): one can be referred to as the shear crack generating within the laminates and the others is referred to as the bending crack production from the bottom surface of the laminates as can be seen in Figure 2.3. In order to effectively estimating the extent of the delamination growth, it would be necessary to include in the model the basic governing parameters controlling the delamination propagation.

For the shear-crack induced delamination, the interlaminar longitudinal shear stress σ_{xz} in the layer right below the interface and the interlaminar transverse shear stress σ_{yz} in the layer right above the interface governing the delamination growth. A schematic determination of the delamination growth mechanism induced by a shear crack is shown in Figure 4.1. However, for a bending crack induced delamination, the interlaminar longitudinal shear stress σ_{xz} in the layer right below the interface and the in-plane bending stress σ_{yy} in the layer right below the interface would advance the delamination propagation in the secondary direction (normal to the fiber direction). A schematic determination of the delamination growth mechanism induced by a bending crack is shown in Figure 4.2.

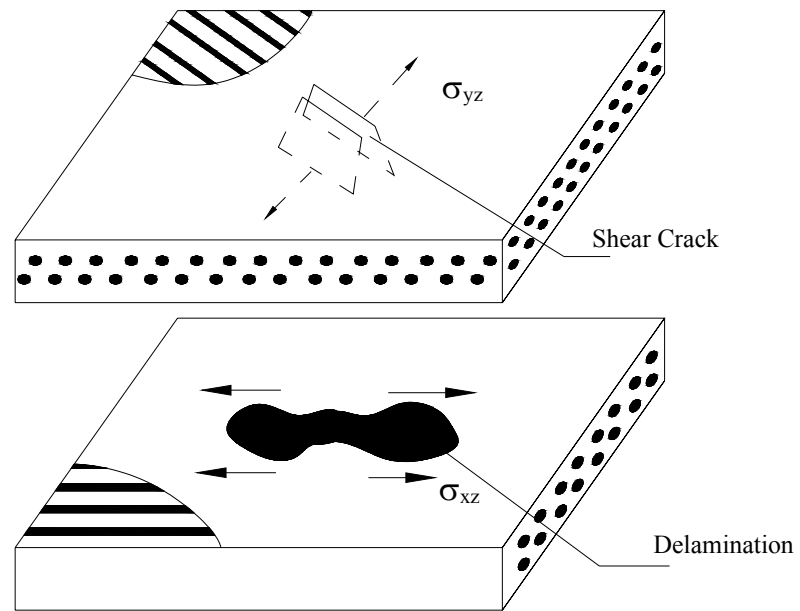


Figure 4.1 A schematic determination of the delamination growth mechanism induced by a shear crack in laminated composite

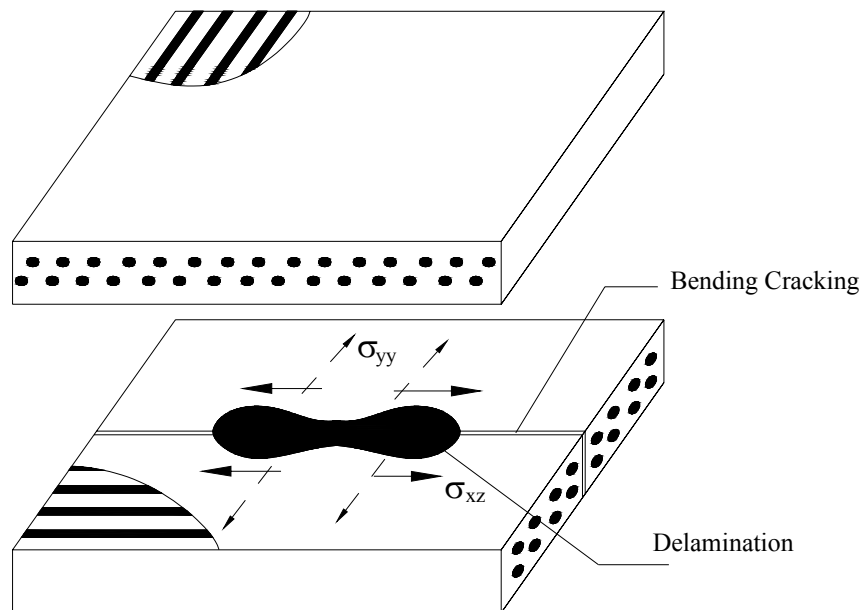


Figure 4.2 A schematic determination of the delamination growth mechanism induced by a bending crack in laminated composite

The distribution of the interlaminar longitudinal shear stress σ_{xz} and transverse in-plane stress σ_{yy} through the thickness of the bottom layer of the interface and the interlaminar transverse shear stress σ_{yz} in the upper layer contribute significantly to the delamination growth resulting from point-nose impact. If one of the ply groups intimately above or below the considered interface has failed due to matrix cracking and if the combined stress governing the delamination growth mechanisms through the thickness of the upper and lower ply groups of the interface reaches a critical value, delamination can growth due to low-velocity impact. Accordingly, impact-induced delamination growth criterion for low-velocity impact is given by Choi & Chang (1992) as follows:

$$D_a \left[\left(\frac{{}^n\bar{\sigma}_{yz}}{{}^nS_i} \right)^2 + \left(\frac{{}^{n+1}\bar{\sigma}_{xz}}{{}^{n+1}S_i} \right)^2 + \left(\frac{{}^{n+1}\bar{\sigma}_{yy}}{{}^{n+1}Y} \right)^2 \right] = e_D^2 \quad (4.9)$$

$$e_D \geq 1 \quad \text{Failure}$$

$$e_D < 1 \quad \text{No failure}$$

$$\bar{\sigma}_{yy} \geq 0 \Rightarrow {}^{n+1}Y = {}^{n+1}Y_t$$

$$\bar{\sigma}_{yy} < 0 \Rightarrow {}^{n+1}Y = {}^{n+1}Y_c$$

where D_a is an empirical constant which has to be determined from experiments. The subscripts x, y and z are the local material coordinates of an individual ply orientation and thickness of the laminates, and the superscripts n and n+1 correspond to the upper and lower plies of the n^{th} interface, respectively. $\bar{\sigma}_{yz}$ and $\bar{\sigma}_{yy}$ are the averaged interlaminar and in-plane transverse stresses within the n^{th} and $(n+1)^{\text{th}}$ ply, respectively. $\bar{\sigma}_{xz}$ is the averaged interlaminar longitudinal stress within the $(n+1)^{\text{th}}$ ply which can be expressed as

$${}^{n+1}\bar{\sigma}_{xz} = \frac{1}{h_{n+1}} \int_{t_n}^{t_{n+1}} \sigma_{xz} dz \quad (4.10)$$

where t_{n+1} and t_n are the upper and lower interfaces of the $(n+1)^{\text{th}}$ ply in the laminate and h_{n+1} is the thickness of the ply.

In order to determine the sensitivity of the empirical constant D_a to laminate configuration, the delamination lengths of the laminates with three tested ply orientations are calculated from the values of D_a varying in a wide range. The calculated lengths are then compared with the corresponding data from the experiments. The measured delamination sizes and shapes from X-radiographs are used for determining the value of D_a . An error formula is selected to estimate the discrepancies between the predictions and measurements based on various values of D_a . The error formula can be expressed as

$$Err^2 = \frac{1}{L^2 N} \sum_{i=1}^N (L_c^i - L_t^i)^2 \quad (4.11)$$

where

L_c : calculated delamination length

L_t : tested delamination length

L : specimen length

N : number of test data

Once a critical matrix crack is predicted in a layer, the delamination criterion is then applied to estimate the extent of the delamination along the interface of the cracked ply in the laminate. It is noted that only the delaminations along the bottom interface induced by bending cracks or along the upper interface induced by a shear crack are included in the analysis. The small, confined delamination along the upper interface induced by shear cracks is ignored in the 3DIMPACT code.

The procedure for determining the extent of the impact damage can be described as follows:

1. Calculating transient dynamic stresses within each layer as function of time

2. Applying the matrix failure criterion for predicting the critical matrix cracks in each layer for determination of the extent of delamination
3. If matrix cracking is predicted in a layer of the laminate, then applying the delamination criterion subsequently in the upper and bottom layer of the interface during the entire period of impact.

The sequence of the above impact damage mechanism is essential for predicting the impact damage. The procedure has to be repeated at the other layers during impact for determining any additional matrix cracking and delaminations. The final size of each delamination is determined by the area within which the stress components satisfy the delamination failure criterion during the entire duration of impact. No material degradation is considered in the model and it is also noted that the model doesn't take into account the delamination interaction during impact which may be important for multiple delaminations (Choi & Chang, 1992).

CHAPTER FIVE

RESULTS AND DISCUSSION

5.1 Introduction

Fiber geometry of the composite is very important parameter for determining the impact behavior of the material. Especially stacking sequence effect and stitching effect are investigated in many studies (Abrate, 1991, 1994, 1998; Cantwell, 1991, Mouritz, 1997). However, there is no study published in open literature related to the cell geometry especially cell size and non orthogonal cells. Cell is determined as the intersection region of the fill and warp strips of the woven composites.

In this study, the stacking sequence effect, gaps between the cells effect, pressure effect, cell size effect, stitching effect and weaving angle effect have been investigated. Impact response of the composite specimen has been detected by means of the force-deflection curves, energy profiles and failure images of the composite specimens. Firstly, the experimental result of the laminated composite $[90/0]_6$ and some important definition on it are presented below.

5.2 $[90/0]_6$ Composites

In this section, each specimen numbered as the same number in all of the Figures. For example, the first specimen subjected to impact loading is shown in the Figure 5.1, Figure 5.3 and Figure 5.4 as numbered 1.

Six force-deflection curves of the $[90/0]_6$ composite are shown in Figure 5.1. Each curve has an ascending section which reaches a maximum force and a descending section which either continues to the maximum deflection or rebounds toward the no-loading state. The highest maximum force is considered as a constant and is called the *peak force*. The ascending sections of all curves are very similar, revealing the consistency of the properties of the composite specimens and the testing conditions

involved. The ascending section is of a concave curve. It can be represented by two tangent lines, which are associated with the resistances of composite to impact loading, namely *stiffnesses*, before and after a point called the *critical point*. The fact that the stiffness after the critical point is greater than that before the critical point is believed to be attributed to the membrane force exerted on the composite from the clamped boundaries. Figure 5.2 shows the important characteristics of a typical force-deflection curve of specimen 6 given in Figure 5.1.

The six curves in Figure 5.1 can be divided into three categories: rebounding, penetration and perforation. Curves 1, 2 and 3, return toward the origin of the diagram after descending from the maximum force or the peak force, indicating the rebounding of the impactor from the specimen surface after impact. Curve 4 has no rebounding section. It stops almost right after the impact force becomes zero. It is close to the penetration point when the impactor stuck in the composite specimen without rebounding from it with the lowest impact energy. Similar to curve 4, both curves 5 and 6 do not have a rebounding section as those of curves 1, 2 and 3. Their forces reach a relatively constant of 650 N at the very end due to the friction between the impactor and the composite specimens after the occurrence of perforation.

The images of the damaged specimens 1-6 are given in Figure 5.3. From the impacted surface, it can be seen that the damage evolves from indentation to matrix crushing, matrix cracking, fiber breakage to perforation. From the non-impacted surface, matrix cracking, delamination (especially on the bottom interface) and fiber bending fracture can be identified.

The relationship between failure mechanisms and the load-deflection curves of $[90/0]_6$ composite can be determined as follows:

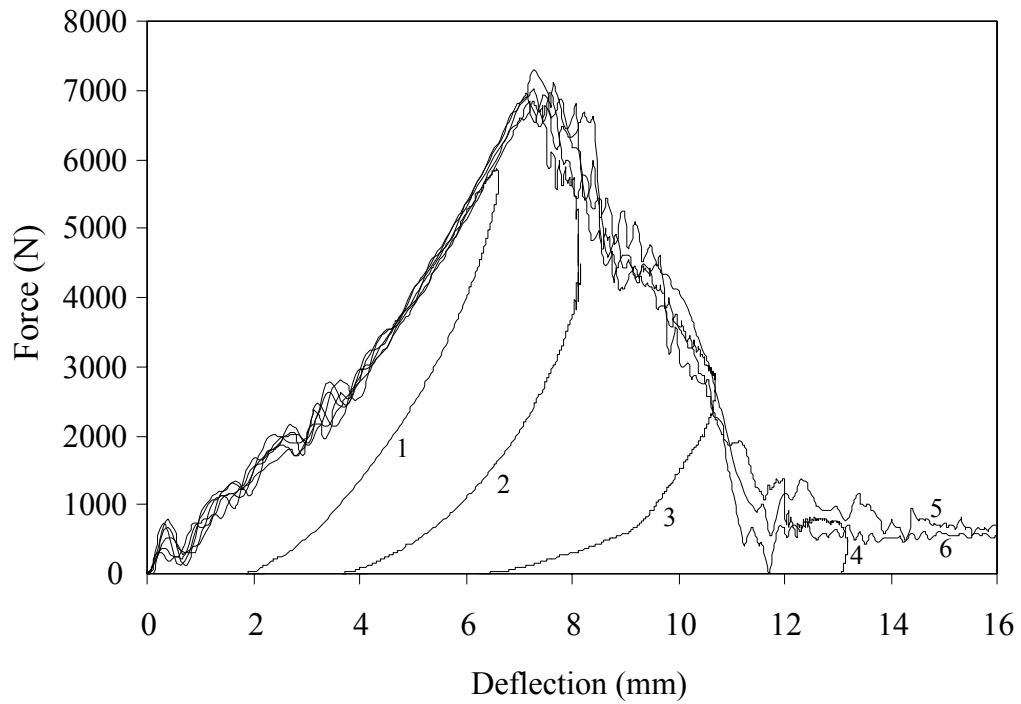


Figure 5.1 Force versus deflection curves of the $[90/0]_6$ composite plate subjected to impact loading.

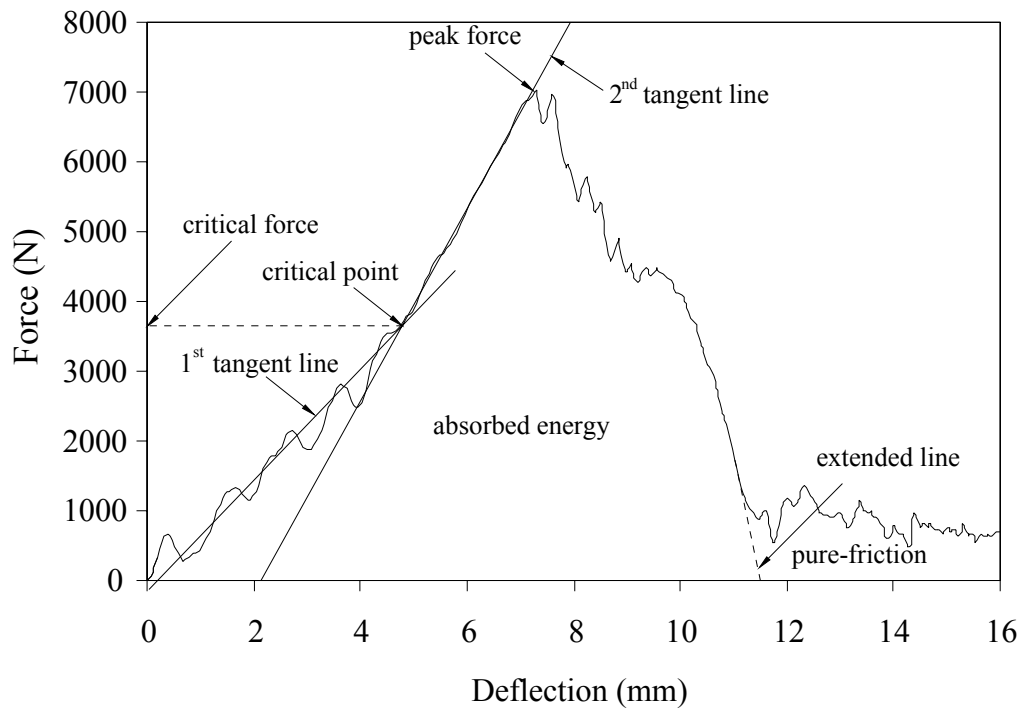


Figure 5.2 Characteristics of force-deflection curve of $[90/0]_6$ composite.

At low impact energy, such as curve 1 of Figure 5.1, the force-deflection curve turns toward the origin of the diagram after reaching a maximum force. There are minor matrix cracks on the top and bottom plies, matrix crushing in the contact-impact zone and some delaminations on the laminate interfaces. The largest delamination occurred in the bottom interface and can be seen in Figure 5.3(1).

As the impact energy is increased, such as curve 2 of Figure 5.2, the maximum force reached the peak force before the force decreasing significantly. This decrease is likely due to the formation of the central fiber breakage and its propagation through the laminate thickness. Figure 5.3(2) shows the central fiber breakages along with grown matrix cracking, matrix crushing and delamination.

As the impact energy is continuously increased, such as curve 3 of Figure 5.1, new damage such as fiber breakages on both sides of the central fiber breakage formed, as can be seen in Figure 5.3(3).

When the impact energy is high enough such as curve 4 of Figure 5.1, penetration took place. The impactor sticks in the specimen and could not rebound from the specimen as can be seen in Figure 5.3(4).

In order to perforate the composite, additional energy is required to bend and/or fracture the fibers blocking the way of the impactor. Curves 5 and 6 in Figure 5.1 give the force-deflection behavior and Figure 5.3 (5, 6) show the top and the bottom image of the perforated composite. It should be noted that some fibers in the bottom ply do not break. They are merely bent away as the impactor moved forward.

The energy profiling method is used for comparing the impact energy and absorbed energy values. Figure 5.4 shows the energy profile of the $[90/0]_6$ composite. The absorbed energies of 1, 2, and 3 numbered specimens are lower than impact energies. The excessive impact energy is used for rebounding of the impactor from the specimen surface after impact.

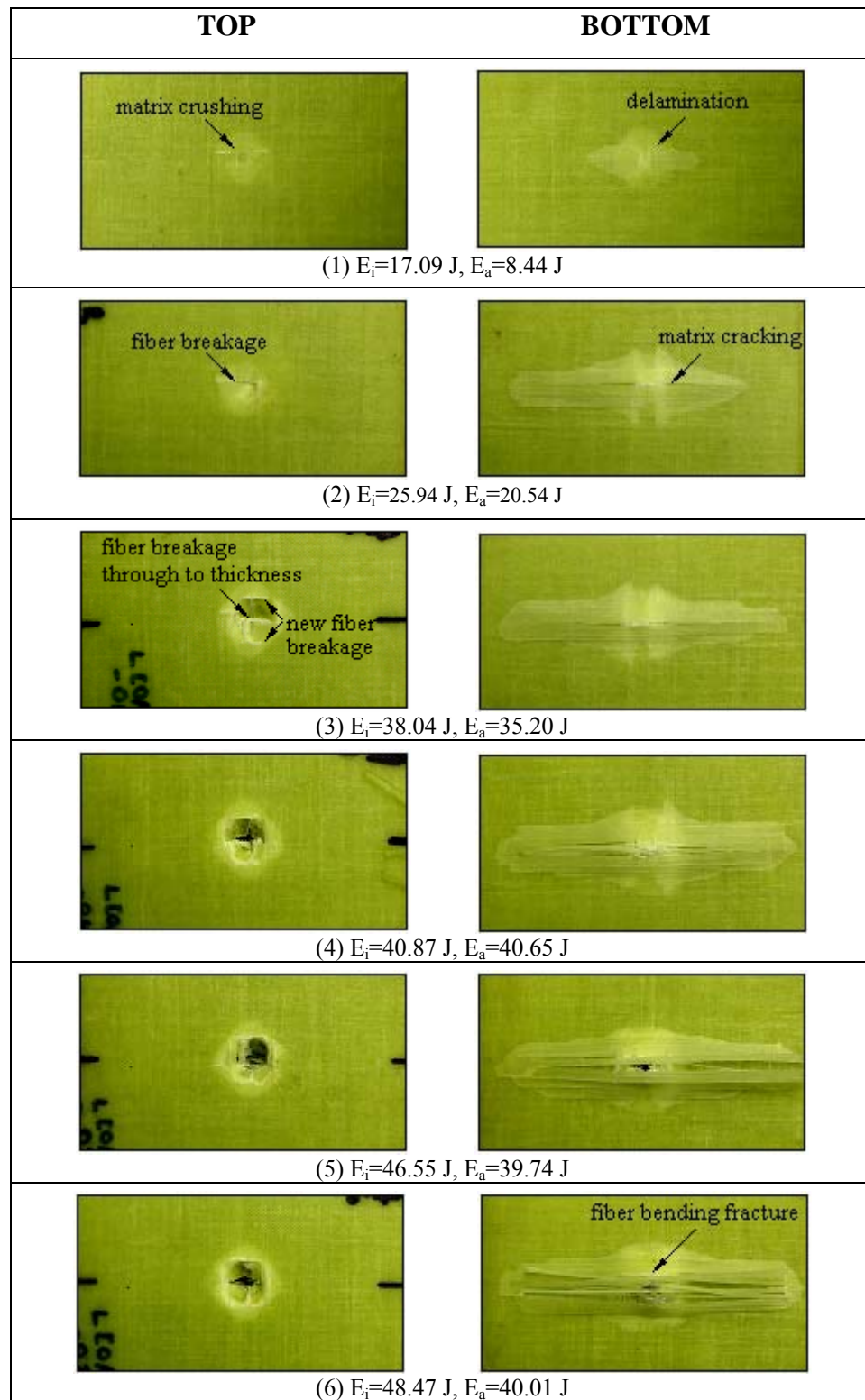


Figure 5.3 Top and bottom images of damaged $[90/0]_6$ composite specimens.

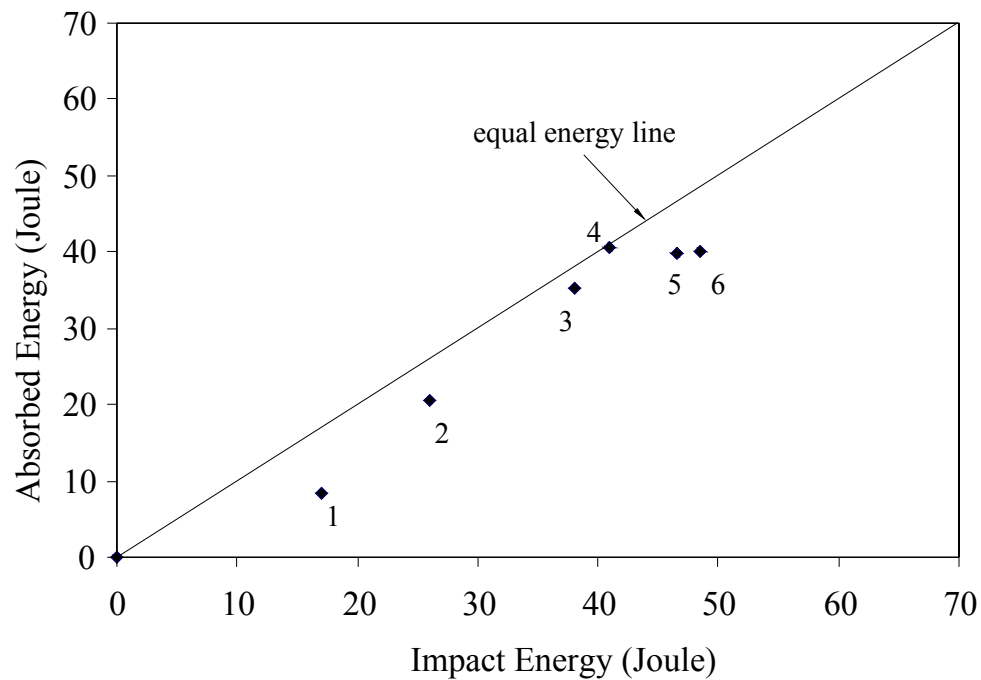


Figure 5.4 Energy profile of the $[90/0]_6$ composite.

The data point numbered 4 is nearly on the equal energy line which indicates impact energy is equal to absorbed energy. It means that the impact energy is absorbed entirely by the specimen. The absorbed energies of the 5, 6 numbered specimens again lower than the impact energies. The excessive energy is consumed by the post perforation motion.

The perforation threshold of the cross ply $[90/0]_6$ composite can be calculated by averaging the absorbed energy values of the perforated specimens. In other words, the perforation threshold value can be found the averaging absorbed energy of specimen 5 and 6 in this part of the study. The threshold is found as 39.87 J for laminated $[90/0]_6$ composite. The perforation threshold may be increased with various stacking sequences of composites.

5.3 Stacking Sequence Effect

In this study, the stacking sequence effects on impact behavior of composite laminates have been investigated. Three laminated composites designated as $[90/0]_6$, $[30/0]_6$ and $[15/0]_6$ were manufactured with the same fiber volume fraction and layer numbers. The unidirectional layers stacked together with desired fiber orientation angle and cured under the pressure of 0.24 MPa. They were then cut into 100mm x 100mm specimens for impact testing.

The typical force-deflection curves for the three laminated composites, $[30/0]_6$, $[15/0]_6$ and $[90/0]_6$, are given in Fig. 5.5 for comparison. From this figure, it is seen that the behaviors of the composite with various stacking sequences are different. All of curves have two stiffnesses. The difference between first bending stiffness and second bending stiffness become small while the angle between adjacent layers decreases. The bending stiffnesses increase with increasing angle between adjacent layers of the composite. $[90/0]_6$ and the $[30/0]_6$ composites have nearly same peak force values while $[15/0]_6$ composite has the lowest one. After the peak force, the force decrease suddenly for the $[30/0]_6$ composite. This decrease becomes with less steep for the $[15/0]_6$ composite. The deflection increases by decreasing angle between adjacent layers. So the $[90/0]_6$ composite has the lowest deflection value. The $[15/0]_6$ composite curve has a large plateau around the peak force and highest deflection value, resulting in the highest perforation threshold. The $[90/0]_6$ curve has highest peak force but lowest deflection value, resulting in the lowest energy absorption capacity for perforation. The deflection value of $[30/0]_6$ is higher than the $[90/0]_6$ composite. Accordingly, $[30/0]_6$ has higher perforation threshold than the $[90/0]_6$ composite.

The energy profiling method is given in Figure 5.6 for comparison of the absorbed energy and impact energy values of the $[15/0]_6$, $[30/0]_6$ and $[90/0]_6$ composites. From Figure 5.6, it is seen that, the $[15/0]_6$ composite has the highest absorbed energy for perforation, followed by the $[30/0]_6$, and then by the $[90/0]_6$ composite. The perforation threshold of the composite can be found by averaging the absorbed energy values for perforated specimen. Calculated perforation threshold values (E_{pr}) are given in the Figure 5.7.

The bending stiffnesses S_1 and S_2 , peak force F_p , critical force F_c , and failure area A_f of $[90/0]_6$, $[30/0]_6$ and $[15/0]_6$ composites are given in Figure 5.7 for comparison. From this figure, it is seen that the first bending stiffness S_1 and second bending stiffness S_2 decrease with decreasing the angle value between adjacent layers of the laminate. The $[15/0]_6$ composite has the lowest bending stiffness values. The difference between S_1 and S_2 decreases as the angle between adjacent layers of the composite decreases. For the $[15/0]_6$ composite, S_1 and S_2 values are nearly same. The critical forces for all specimens with various stacking sequence angle are similar. The $[90/0]_6$ composite has the highest peak force value, followed by $[30/0]_6$ and then by $[15/0]_6$ composite.

The damage size can be identified by placing the specimen on a light table to find damage boundary. It can be seen through the light that the specimen has the damage boundaries which are not unique. It should be taken the darkest boundary lines, not include the boundaries formed by the delamination at the bottom interface. The damage boundaries are drawn on a transparent plastic layer and scanned by using a scanner. The damage area is then calculated from the image. The failure areas of the laminates are given in Figure 5.7. The $[90/0]_6$ laminate has the largest damage area. The $[30/0]_6$ and the $[15/0]_6$ composites have nearly same damage areas.

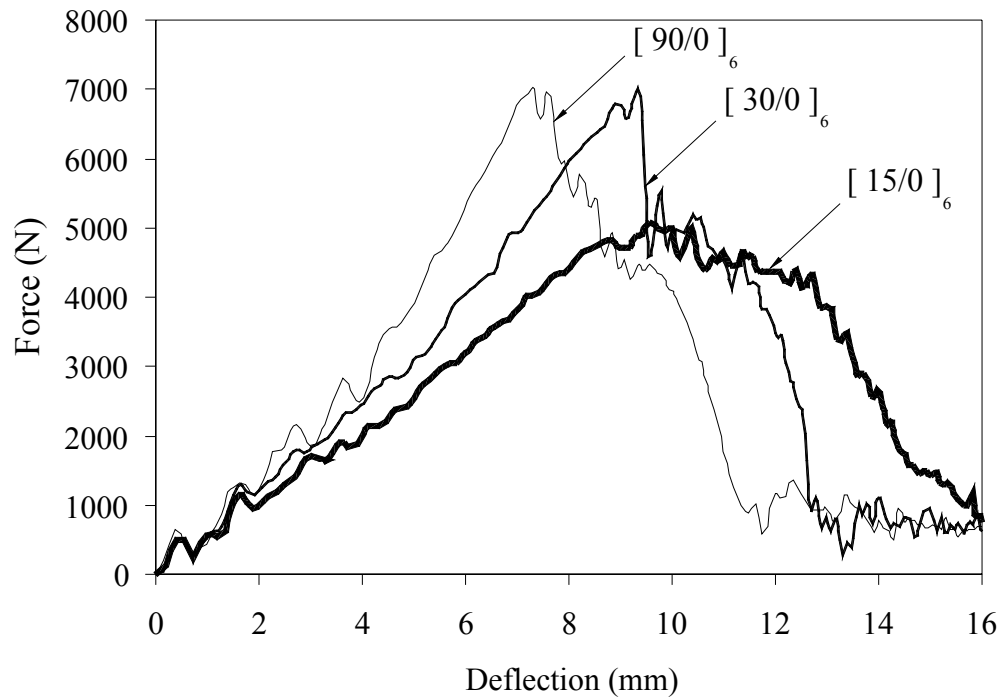


Figure 5.5 Typical force-deflection curves for $[90/0]_6$, $[30/0]_6$ and $[15/0]_6$ composites.

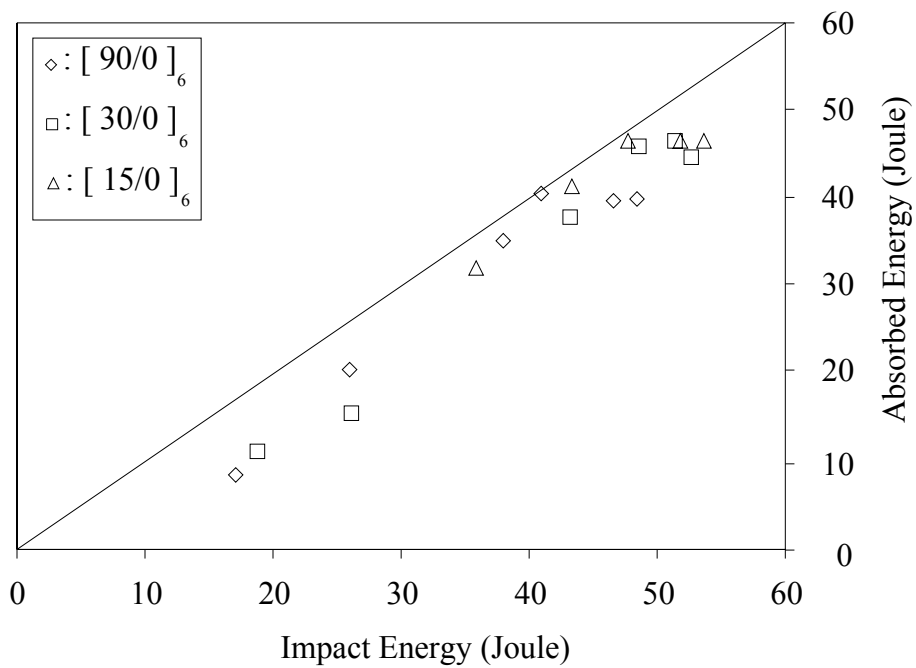


Figure 5.6 Energy profile of the composites with various stacking sequences

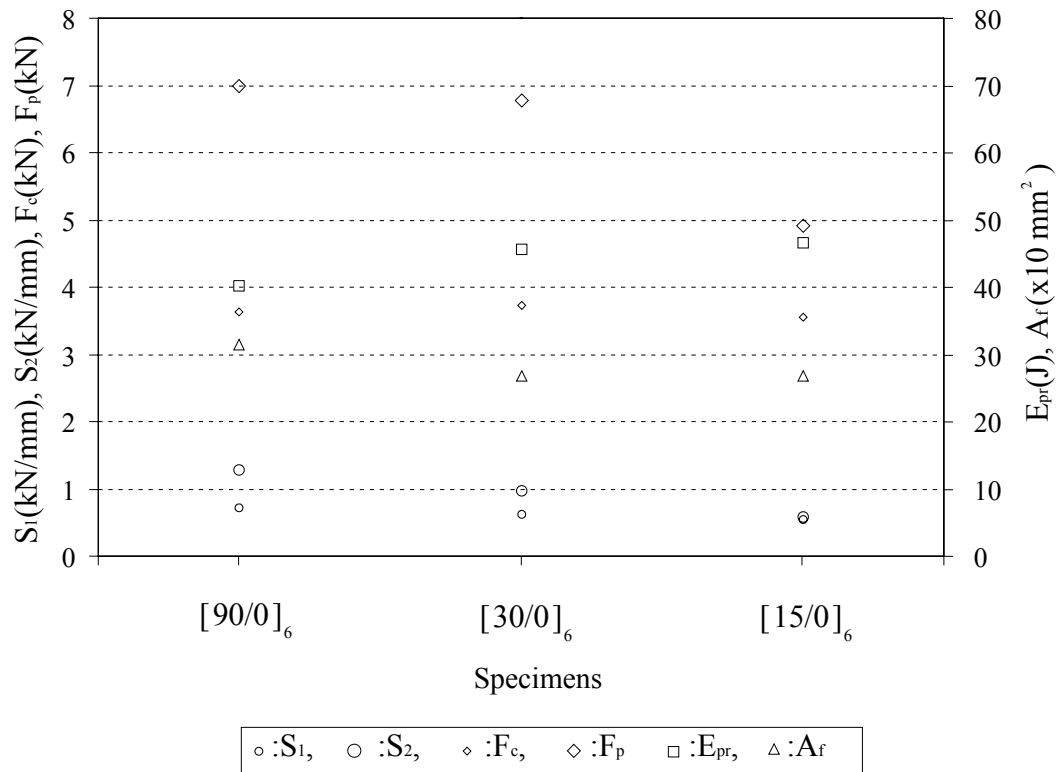


Figure 5.7 Comparison of impact response of the $[90/0]_6$, $[30/0]_6$ and $[15/0]_6$ composites.

The top and bottom image of the $[90/0]_6$, $[30/0]_6$ and $[15/0]_6$ composites are shown in Figure 5.8. The $[90/0]_6$ composite has largest delamination in bottom interface while the $[15/0]_6$ composite has smallest one. The damage becomes ellipse shape as the angle between adjacent layers decreases.

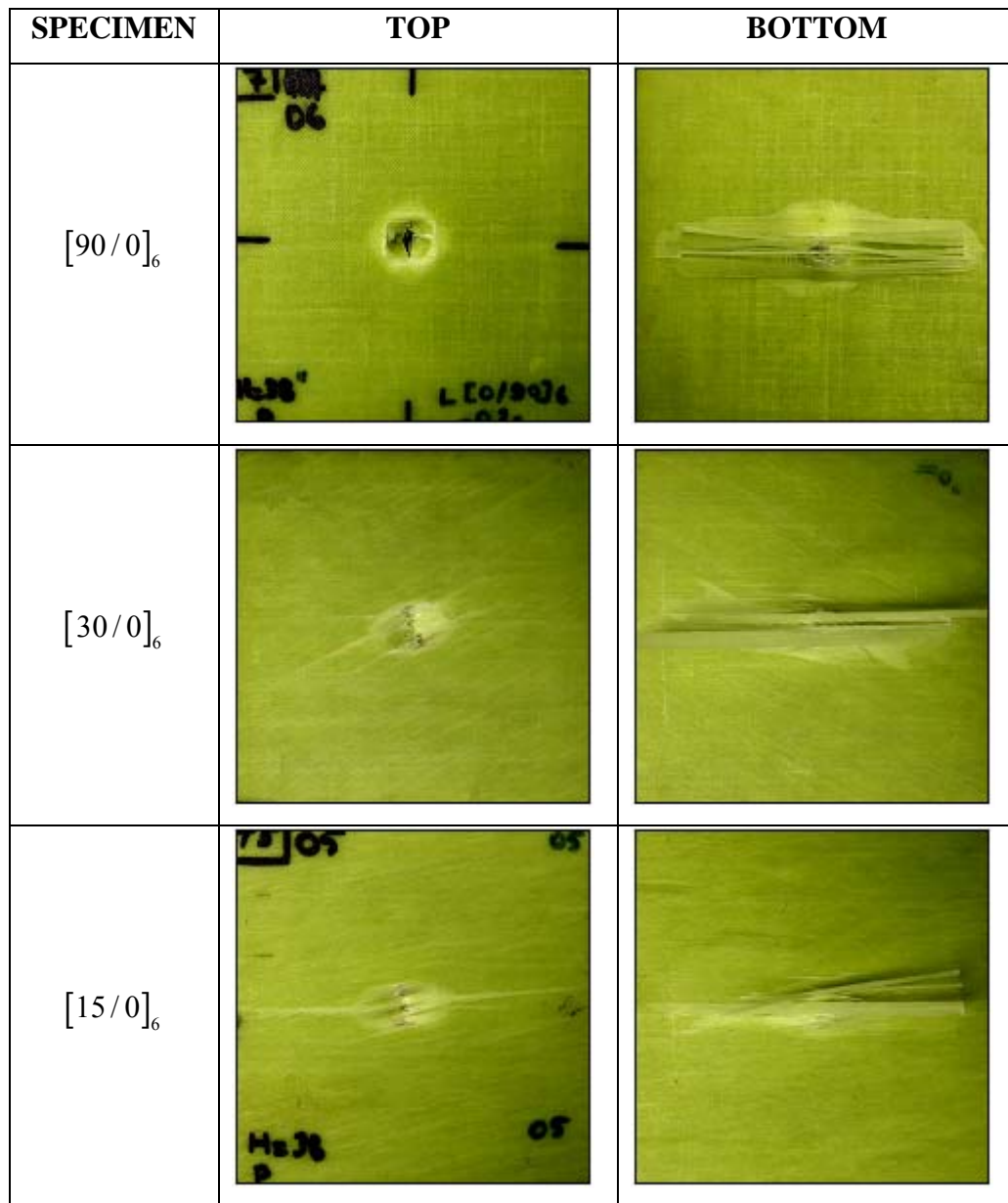


Figure 5.8 Top and bottom images of the damaged laminated composites.

5.4 Pressure and Gaps between Cells Effect

Gap is the clearance between the cells as shown in Figure 5.9. Existence of the gaps may affect the impact behavior of the composite. Additionally, the curing pressure may change the impact response of the composite. Before production of all the woven composite specimens, it is necessary to determine these two important parameters.

In this study the curing pressure effect and the gaps between the cells of the woven composite have been investigated. Because of its easy weaving procedure, the $[\underline{90/0}]_4^{25.4 \times 25.4}$ woven composite was chosen for the investigation. Two woven composites designated as $[\underline{90/0}]_4^{25.4 \times 25.4}$ with gap and $[\underline{90/0}]_4^{25.4 \times 25.4}$ without gap. The geometries of the woven composites are given in Figure 5.9. They are orthogonal plain-weave composites with the strand widths which are equal to 25.4 mm in both fill and warp directions. In making the woven composites, woven layers were first prepared from manually weaving strands sliced from the unidirectional prepreg tape. Four woven layers were then stacked together with cell boundaries well aligned through the thickness. The woven composites were subsequently cured under low pressure (0.24 MPa) which is used in production of the laminated composites mentioned in the previous sections and high pressure (2.88 MPa). They were then cut into 100mm x 100 mm specimens for impact testing.

In writing, it is difficult to determine pressure effect and gap effect for each specimen. For this reason a special code is used for determining the specimens. In order to identify the $[\underline{90/0}]_4^{25.4 \times 25.4}$ cured under low pressure and high pressure, the notation of LP and HP are used, respectively. The subscripts 1 and 2 are used for determining the production of $[\underline{90/0}]_4^{25.4 \times 25.4}$ composite with gaps and without gap respectively. For instance, the notation of HP₁ indicates the $[\underline{90/0}]_4^{25.4 \times 25.4}$ composite with gap and cured under the high pressure.

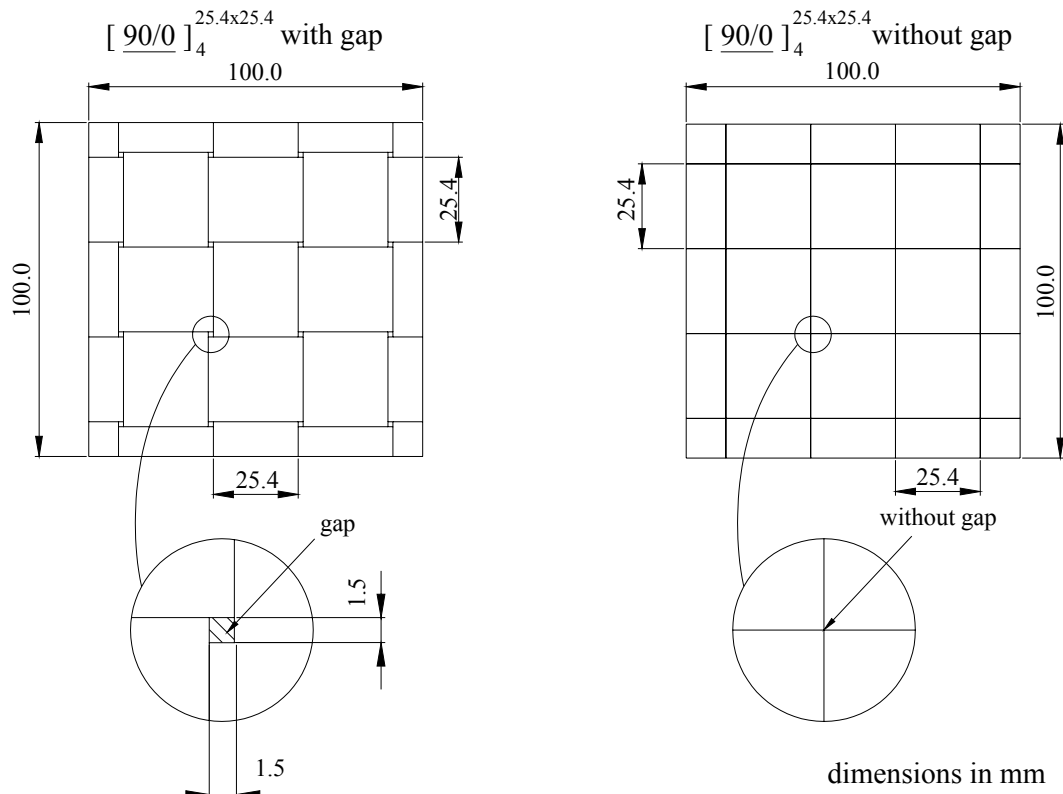


Figure 5.9 Geometry of the $[90/0]_4^{25.4 \times 25.4}$ composite with and without gap

The typical force-deflection curves of the woven composite $[90/0]_4^{25.4 \times 25.4}$ under the condition of high pressure with gap (HP₁), high pressure without gap (HP₂), low pressure with gap (LP₁) and low pressure without gap (LP₂) are given in Figure 5.10. The ascending sections of the curves except for LP₂ are nearly the same, implying similar stiffnesses and critical point. However, the peak forces are different. LP₁ has the highest peak force while the LP₂ has the lowest. LP₁ which has a wide plateau around the peak force may result highest perforation threshold. However, HP₂ which has the sharpest force-deflection curves may result the lowest absorbed energy for perforation. Composites cured under the high pressures have a similar deflection values. However, the existence of gap decreases the deflection value for the composite cured under the low pressure.

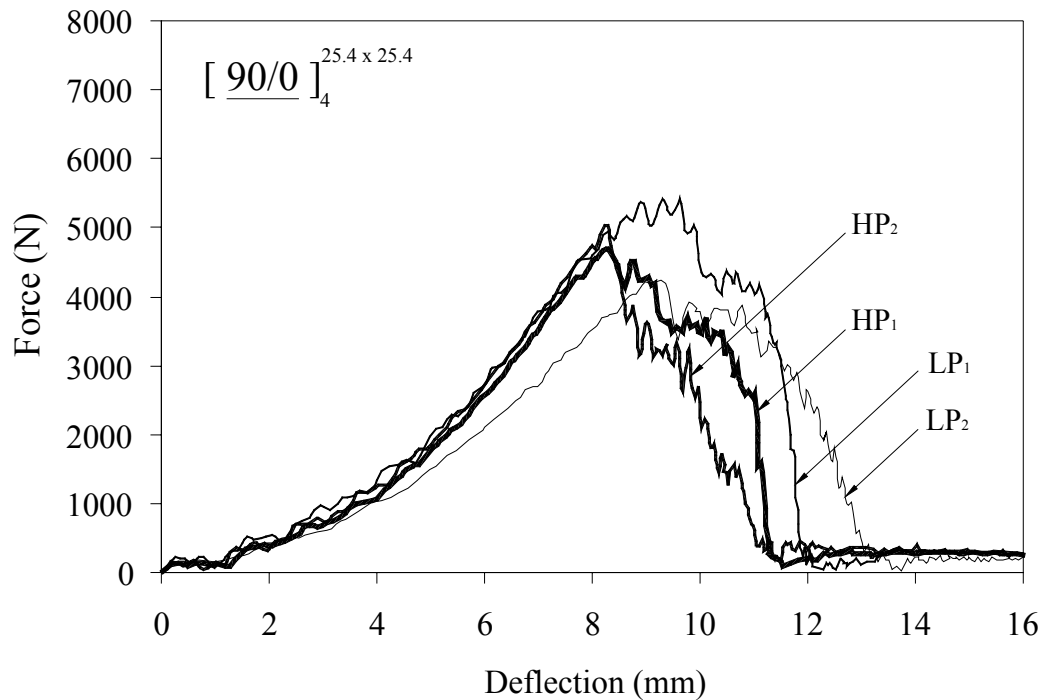


Figure 5.10 Typical force-deflection curves for woven composites with gap and without gap cured under the high pressure and low pressure.

The absorbed energy versus impact energy values of HP₁, HP₂, LP₁ and LP₂ are given in Figure 5.11. It is seen that, from the figure, the LP₁ has the highest perforation threshold, following by LP₂, and then by HP₁. The HP₂ has the lowest threshold.

The impact responses of the $[90/0]_4^{25.4 \times 25.4}$ composites are given in Figure 5.12. The first and the second bending stiffnesses of the HP₁, HP₂, and LP₁ composites are similar. The LP₂ has the low bending stiffnesses. The critical force value also is the lowest for LP₂. The LP₁ has the highest critical force value. LP₁ has also the highest peak force, perforation threshold and failure area.

The top and bottom image of the HP₁, HP₂, LP₁ and LP₂ composites are shown in Figure 5.13. The HP₁ composite has largest delamination in bottom interface while the LP₂ composite has smallest. HP₂ and LP₁ composites have similar delamination area in bottom interface.

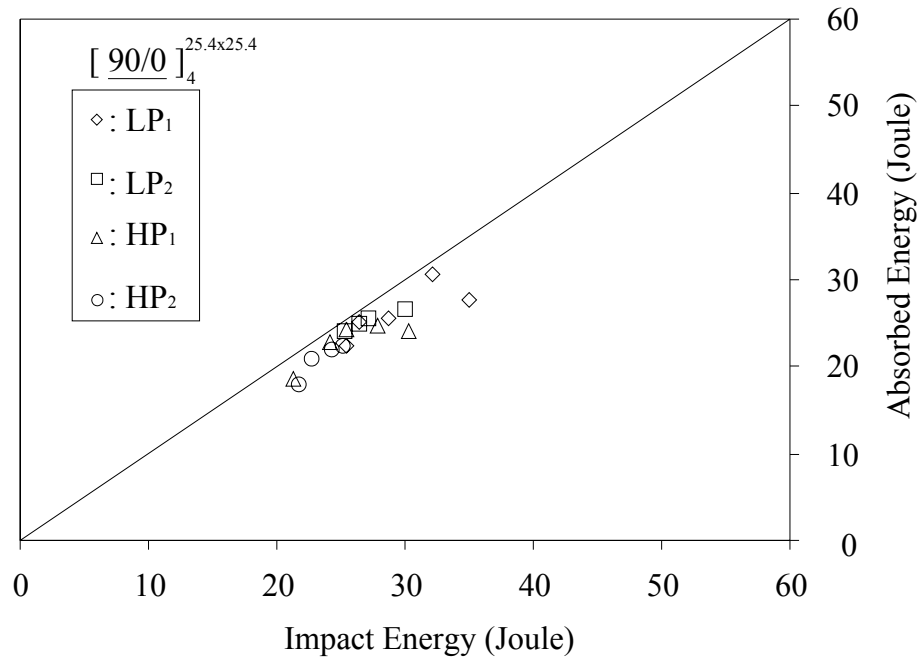


Figure 5.11 Energy profiles for the HP₁, HP₂, LP₁ and LP₂ composites.

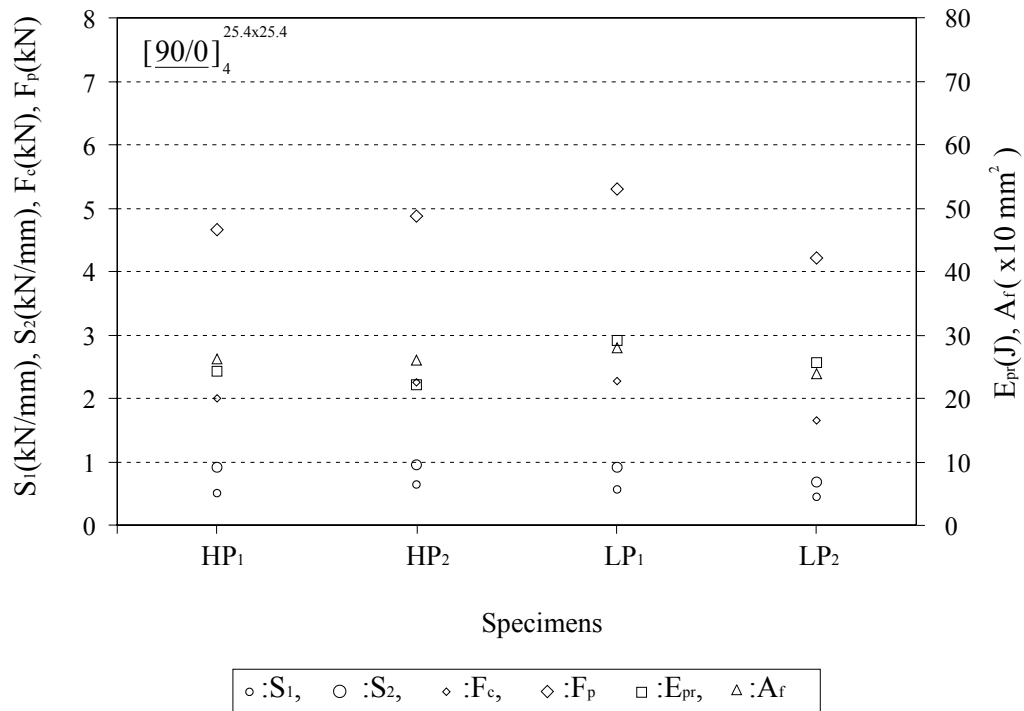


Figure 5.12 Comparison of impact response of $[90/0]_4^{25.4 \times 25.4}$ with the conditions of HP₁, HP₂, LP₁ and LP₂.

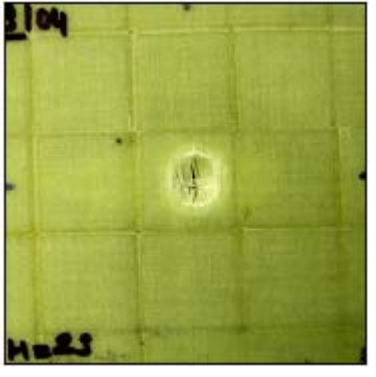
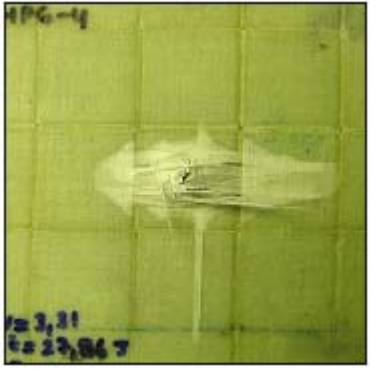
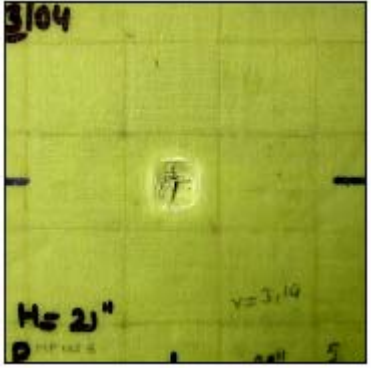

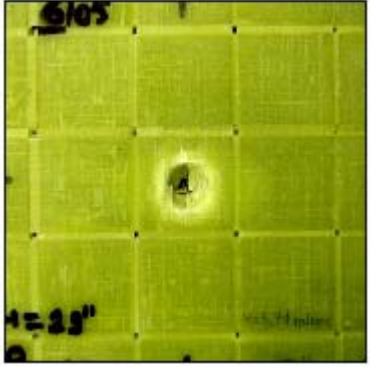
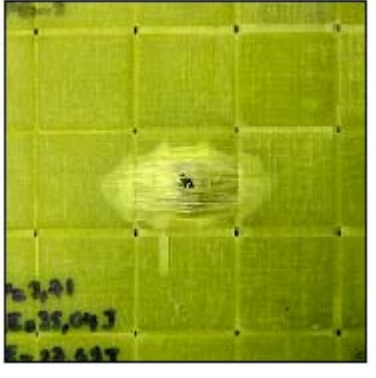
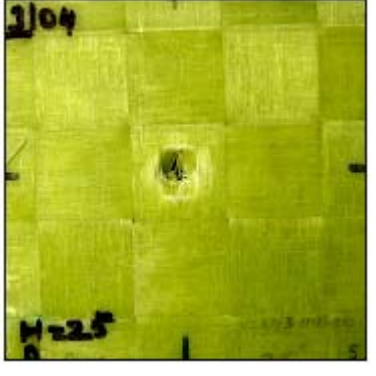

SPECIMEN	TOP	BOTTOM
$[90/0]_4^{25.4 \times 25.4}$ High Pressure With Gap (HP ₁)		
$[90/0]_4^{25.4 \times 25.4}$ High Pressure Without Gap (HP ₂)		
$[90/0]_4^{25.4 \times 25.4}$ Low Pressure With Gap (LP ₁)		
$[90/0]_4^{25.4 \times 25.4}$ Low Pressure Without Gap (LP ₂)		

Figure 5.13 Top and bottom images of damaged woven composites.

From this part of the investigation, it is concluded that the woven composites with gaps between cells and cured under low pressure have better impact properties than the other gap and pressure variations of the composites. Accordingly, the woven composites investigated in next sections were produced with these conditions.

5.5 Cell Size Effect

This study is on the effect of cell size of woven composites on impact behavior. Three woven composites designated as $[\underline{90/0}]_6^{25.4 \times 25.4}$, $[\underline{90/0}]_6^{12.7 \times 12.7}$ and $[\underline{90/0}]_6^{6.4 \times 6.4}$ were manufactured. They were orthogonal plain-weave composites with the strand widths in both fill and warp directions equal to 25.4 mm, 12.7 mm and 6.4 mm, respectively. In making the woven composites, woven layers were first prepared from manually weaving strands sliced from the unidirectional prepreg tape used for making laminated composites. Six woven layers with identical cell size were then stacked together with cell boundaries well aligned through the thickness. The woven composites were subsequently cured with the curing parameters identical to those of laminated counterparts. They were then cut into 100mm x 100mm specimens for impact testing. Fig. 5.14 shows the three woven composite specimens and the corresponding impacted areas.

The typical force-deflection curves for the three woven composites of interest, i.e. $[\underline{90/0}]_6^{25.4 \times 25.4}$, $[\underline{90/0}]_6^{12.7 \times 12.7}$ and $[\underline{90/0}]_6^{6.4 \times 6.4}$, along with that of the laminated $[\underline{90/0}]_6$ are given in Fig. 5.15 for comparison. The ascending sections of the curves are nearly the same, implying similar stiffnesses and critical point. The maximum deflections are also very similar. The peak forces, however, are different. The $[\underline{90/0}]_6^{25.4 \times 25.4}$ composite has the highest peak force, followed by $[\underline{90/0}]_6^{12.7 \times 12.7}$, while the $[\underline{90/0}]_6^{6.4 \times 6.4}$ composite has the lowest value. The similarity in stiffnesses and the difference in peak force for the three cases investigated indicate that the stiffnesses are not affected by microscopic fiber geometry while the peak force is. Woven composites

with larger cells use larger weaving strands and have larger contact-impact force, which are dependent on the local damage process, than those with smaller cells. On the contrary, the cell size does not seem to affect the global impact stiffnesses.

The area bounded by the force-deflection curve for $[\underline{90/0}]_6^{6.4 \times 6.4}$ is not as sharp as that for $[\underline{90/0}]_6^{12.7 \times 12.7}$. It has a larger plateau around the peak force, resulting in higher energy absorption than $[\underline{90/0}]_6^{12.7 \times 12.7}$.

The energy profiling method is used for comparing the impact energy and absorbed energy values. Figure 5.16 shows the energy profile of the $[\underline{90/0}]_6^{6.4 \times 6.4}$, $[\underline{90/0}]_6^{12.7 \times 12.7}$, $[\underline{90/0}]_6^{25.4 \times 25.4}$ and $[\underline{90/0}]_6$ composites. From Figure 5.16, it is seen that, the $[\underline{90/0}]_6^{25.4 \times 25.4}$ composite has highest absorbed energy for perforation, followed by the $[\underline{90/0}]_6$, and then by the $[\underline{90/0}]_6^{6.4 \times 6.4}$ composite. The $[\underline{90/0}]_6^{12.7 \times 12.7}$ composite has lowest absorbed energy for perforation. The perforation threshold of the composite can be found by averaging the absorbed energy values for perforated specimen. Calculated perforation threshold will be given in the Figure 5.17.

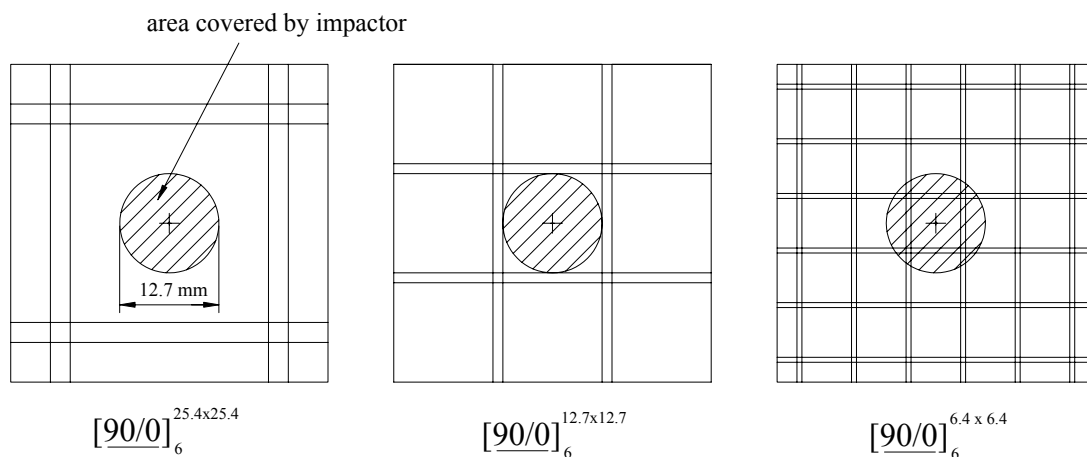


Figure 5.14 Areas covered by the impactor nose in the woven composite.

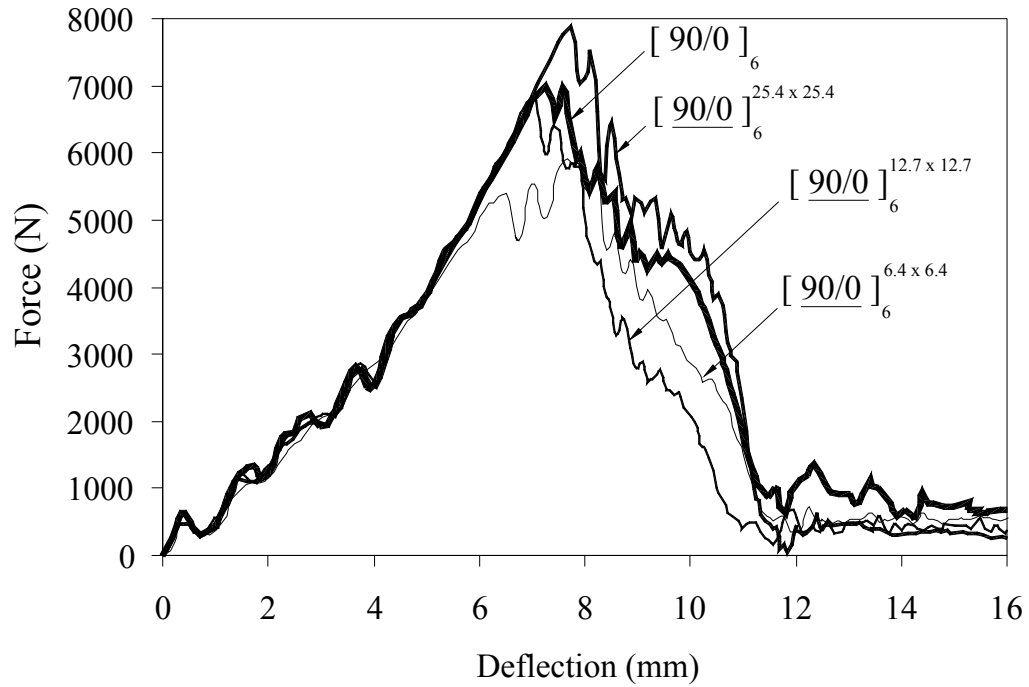


Figure 5.15 Typical force-deflection curves for $[90/0]_6$, $[90/0]_6^{25.4 \times 25.4}$, $[90/0]_6^{12.7 \times 12.7}$ and $[90/0]_6^{6.4 \times 6.4}$ composites.

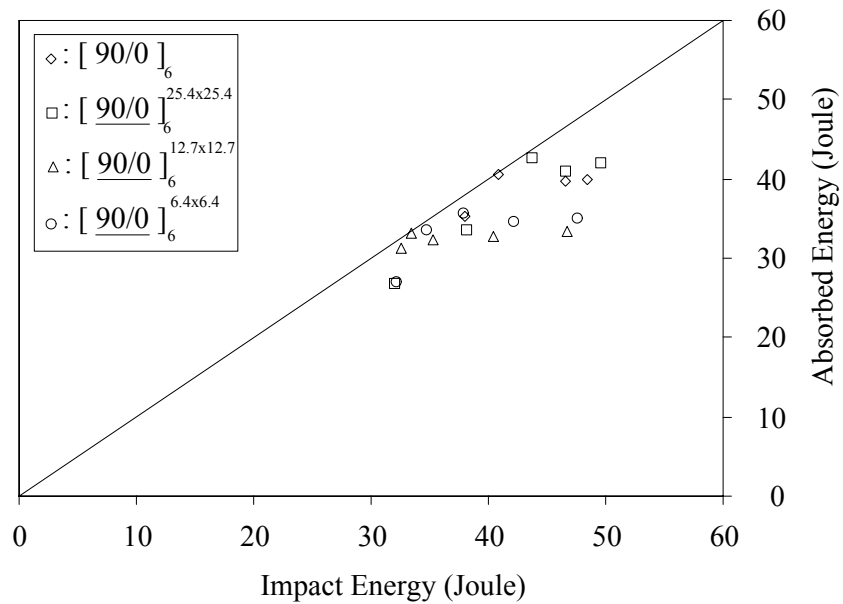


Figure 5.16 Energy profiles for the $[90/0]_6$, $[90/0]_6^{25.4 \times 25.4}$, $[90/0]_6^{12.7 \times 12.7}$ and $[90/0]_6^{6.4 \times 6.4}$ composites.

The bending stiffnesses S_1 and S_2 , peak force F_p , critical force F_c , absorbed energy for perforation E_a , failure area A_f and cell area A_c values of woven composites $[\underline{90/0}]_6^{25.4 \times 25.4}$, $[\underline{90/0}]_6^{12.7 \times 12.7}$ and $[\underline{90/0}]_6^{6.4 \times 6.4}$, and $[\underline{90/0}]_6$ laminated composite are given in Fig. 5.17 for comparison.

From the Fig. 5.17, it is seen that the peak force increases as the cell size increases except for the laminated case. The first bending stiffness S_1 is nearly same for all cell sizes. The second bending stiffness S_2 and critical force F_c are lowest for the $[\underline{90/0}]_6^{6.4 \times 6.4}$ and similar for the $[\underline{90/0}]_6$, $[\underline{90/0}]_6^{25.4 \times 25.4}$, $[\underline{90/0}]_6^{12.7 \times 12.7}$ composites. The perforation thresholds in these four cases are not proportional to the cell size. The $[\underline{90/0}]_6^{25.4 \times 25.4}$ composite has the largest threshold followed by the laminated composite $[\underline{90/0}]_6$ and then by the $[\underline{90/0}]_6^{6.4 \times 6.4}$ composite. The $[\underline{90/0}]_6^{12.7 \times 12.7}$ composite has the lowest perforation threshold. This result can be interpreted by the restriction due to the cell boundary. The $[\underline{90/0}]_6^{12.7 \times 12.7}$ composite has a cell size approximately equal to the size of the impactor nose. The cell boundary seems to restrict the extension of the damage caused by the impactor nose. In the $[\underline{90/0}]_6^{6.4 \times 6.4}$ case, the cell size of the impactor nose covers a region of 3 x 3 cells as shown in Figure 5.14. The damage of the woven composite is not confined by one single cell; it can extend in the region of 3 x 3 cells. Top and bottom image of the damaged woven composites with various cell sizes are given in Figure 5.18. The bottom layer of the laminated plate was delaminated from the specimen. There were fractures in the bottom layers of the woven plates. The $[\underline{90/0}]_6^{25.4 \times 25.4}$ plate has damage up to the cell boundary.

The failure mechanism of the woven composite plates is slightly different from that of the $[\underline{90/0}]_6$ plate. At the back side (the unimpacted side) of the woven specimens, the fill yarns were not torn away from the specimens because of the restriction posed by the warp yarns. They were broken in the middle of the cells. The delaminations, especially in the bottom interface, were smaller. When the cell size is decreased, the delamination area becomes smaller and more localized around the impactor nose.

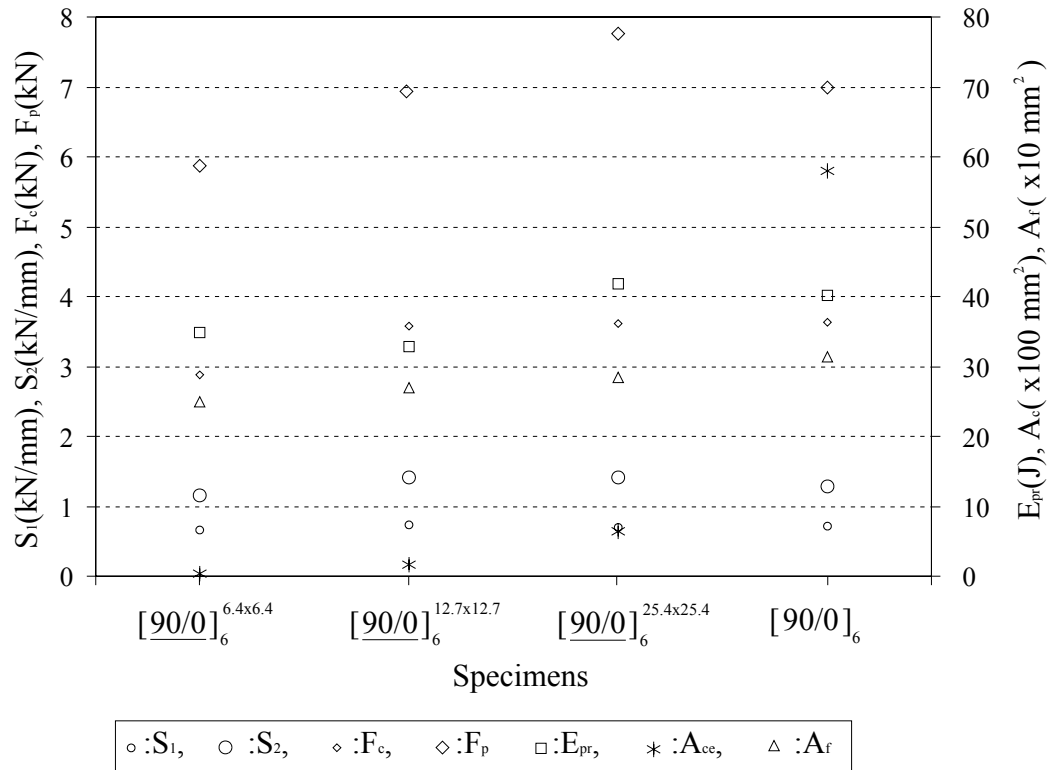


Figure 5.17 Comparison of impact response woven composites with various cell sizes.

5.6 Stitching Effect

Stitched woven composites were investigated in this study. Some woven composites were stitched with glass/epoxy threads which were sliced from the prepreg tape and had a width of 1 mm. The stitches were performed manually with the use of a needle. The stitching pattern has square grids of 12.7 mm x 12.7 mm with the stitching threads across the diagonal of the grids. The stitching patterns of the $S[90/0]_6$, $S[90/0]_6^{25.4x25.4}$, $S[90/0]_6^{12.7x12.7}$ and $S[90/0]_6^{6.4x6.4}$ composites are given in Figure 5.19. They have identical stitching density, i.e. one stitch per 12.7 mm x 12.7 mm. The stitching points for the $S[90/0]_6^{12.7x12.7}$ and $S[90/0]_6^{6.4x6.4}$ plates are located on the corners of the cells. The stitching points for the $S[90/0]_6$ and $S[90/0]_6^{25.4x25.4}$ plates, however, are not applied to the corners of the cells, resulting in additional damage to plates.

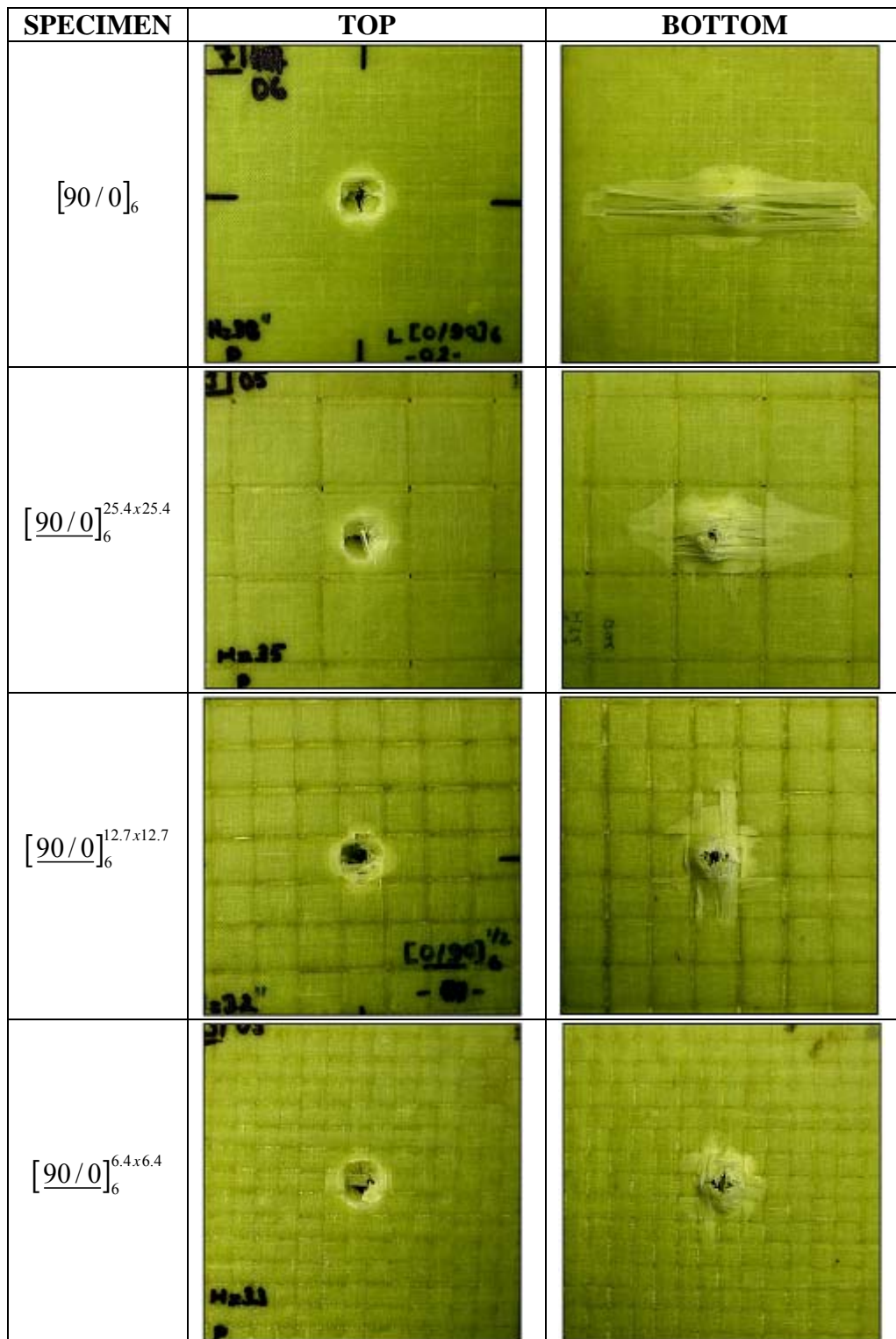


Figure 5.18 Top and bottom images of damaged woven composites with various cell size.

The typical force-deflection curves for the $S[90/0]_6$, $S[90/0]_6^{25.4 \times 25.4}$, $S[90/0]_6^{12.7 \times 12.7}$ and $S[90/0]_6^{6.4 \times 6.4}$ plates are shown in Figure 5.20. The ascending sections of the curves are very similar. The $S[90/0]_6^{12.7 \times 12.7}$ composite has the highest peak force while the $S[90/0]_6^{6.4 \times 6.4}$ composite has the lowest. The load-deflection curve of the $S[90/0]_6^{12.7 \times 12.7}$ composite is sharper around the peak force than that of the $S[90/0]_6^{6.4 \times 6.4}$ one. The deflections of all stitched composites are similar.

Figure 5.21 shows the energy profile of the $S[90/0]_6^{6.4 \times 6.4}$, $S[90/0]_6^{12.7 \times 12.7}$, $S[90/0]_6^{25.4 \times 25.4}$ and $S[90/0]_6$ composites. From Figure 5.21, it is seen that, the $S[90/0]_6$ composite has highest absorbed energy for perforation, followed by the $S[90/0]_6^{25.4 \times 25.4}$, and then by the $S[90/0]_6^{6.4 \times 6.4}$ composite. The $S[90/0]_6^{12.7 \times 12.7}$ composite has lowest absorbed energy for perforation. The perforation threshold of the composite can be found by averaging the absorbed energy values for perforated specimen. Calculated perforation threshold are given in the Figure 5.22.

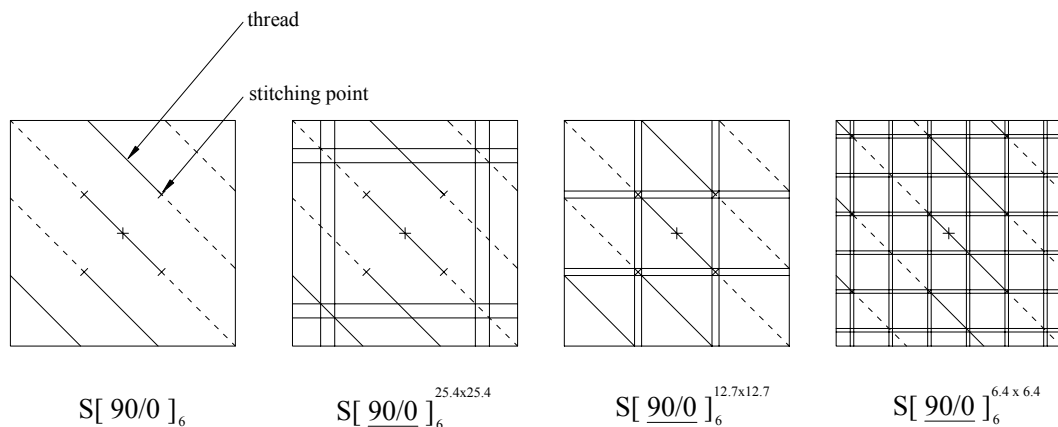


Figure 5.19 Stitching pattern of woven composite.

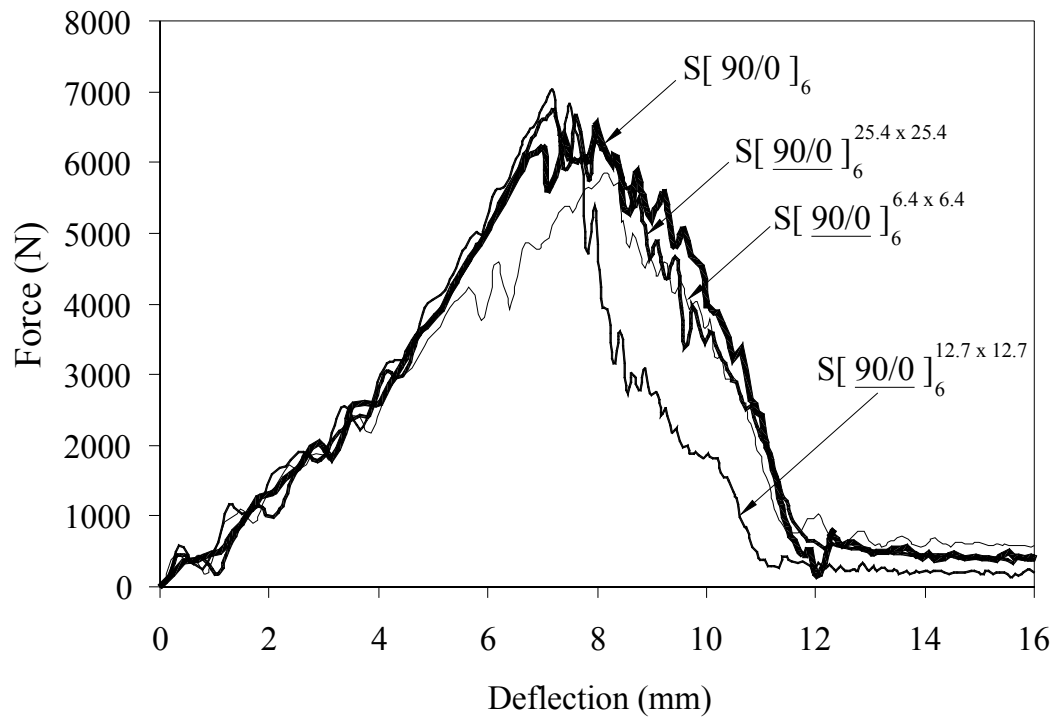


Figure 5.20 Typical force-deflection curves for stitched woven composites.

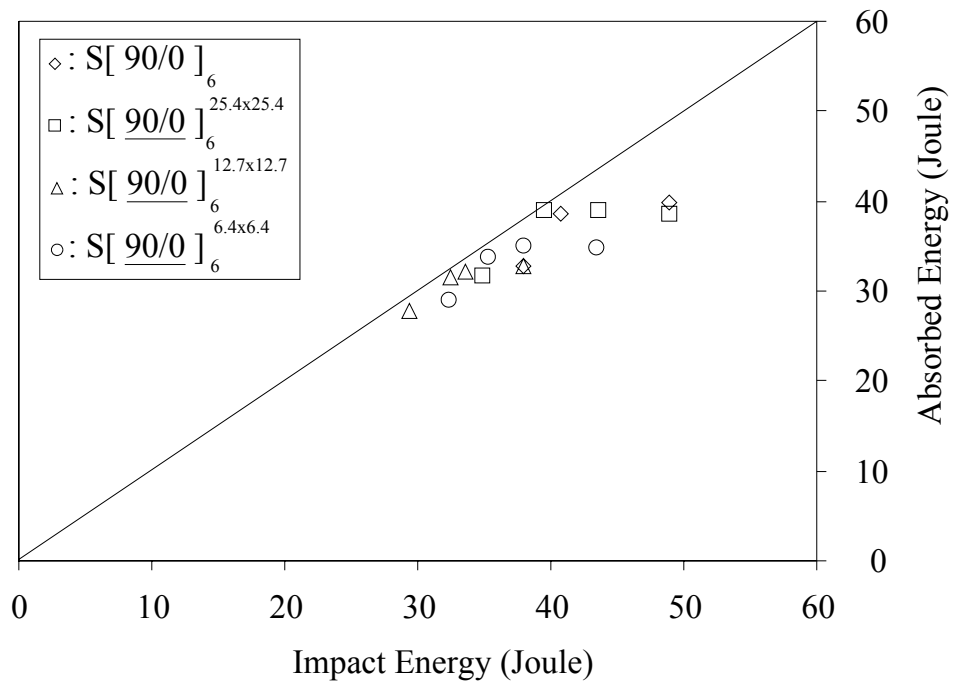


Figure 5.21 Energy profiles for the $S[90/0]_6$, $S[90/0]_6^{25.4 \times 25.4}$, $S[90/0]_6^{12.7 \times 12.7}$ and $S[90/0]_6^{6.4 \times 6.4}$ composites.

The first bending stiffness S_1 , second bending stiffness S_2 , critical force F_c , peak force F_p , failure area A_f , cell area A_{ce} and absorbed energy for perforation E_{pr} of the stitched composites are given in Figure 5.22. From this figure, it is seen that the $S[\underline{90/0}]_6^{12.7 \times 12.7}$ has the highest peak force as the $S[\underline{90/0}]_6^{6.4 \times 6.4}$ composite has lowest. The first bending stiffness S_1 is nearly same for all cell sizes. The second bending stiffness S_2 and critical force F_c are lowest for the $S[\underline{90/0}]_6^{6.4 \times 6.4}$ and similar for the $S[\underline{90/0}]_6$, $S[\underline{90/0}]_6^{25.4 \times 25.4}$, $S[\underline{90/0}]_6^{12.7 \times 12.7}$ composites. The perforation thresholds E_{pr} in these four cases are not proportional to the cell size. The $S[\underline{90/0}]_6$ composite has the largest threshold followed by the $S[\underline{90/0}]_6^{25.4 \times 25.4}$ and then by the $S[\underline{90/0}]_6^{6.4 \times 6.4}$ composite. The $S[\underline{90/0}]_6^{12.7 \times 12.7}$ composite has the lowest perforation threshold.

From the comparison the Figure 5.17 and Figure 5.22 for stitching effect, it is seen that the peak force and absorbed energy for perforation are generally lower for the $S[\underline{90/0}]_6^{25.4 \times 25.4}$ and $S[\underline{90/0}]_6$ cases than for the corresponding unstitched cases. However, the peak force and absorbed energy are nearly same in the stitched and the unstitched for the $S[\underline{90/0}]_6^{6.4 \times 6.4}$ and $S[\underline{90/0}]_6^{12.7 \times 12.7}$ composites. This difference between the group with the large cell size, i.e. $S[\underline{90/0}]_6$ and $S[\underline{90/0}]_6^{25.4 \times 25.4}$ and the group with the small size, i.e. $S[\underline{90/0}]_6^{12.7 \times 12.7}$ and $S[\underline{90/0}]_6^{6.4 \times 6.4}$ again can be explained by the cell size. In the larger cell size group, the stitches were not performed on the cell corners, resulting additional damage to the composites. However, the stitches were performed on the cell corners of $S[\underline{90/0}]_6^{12.7 \times 12.7}$ and $S[\underline{90/0}]_6^{6.4 \times 6.4}$ cases and no additional damage was introduced to the composites. The additional damage might reduce peak force and absorbed energy values. The first bending stiffness value does not change but the second bending stiffness and the critical force values become lower with stitching for all cell sizes.

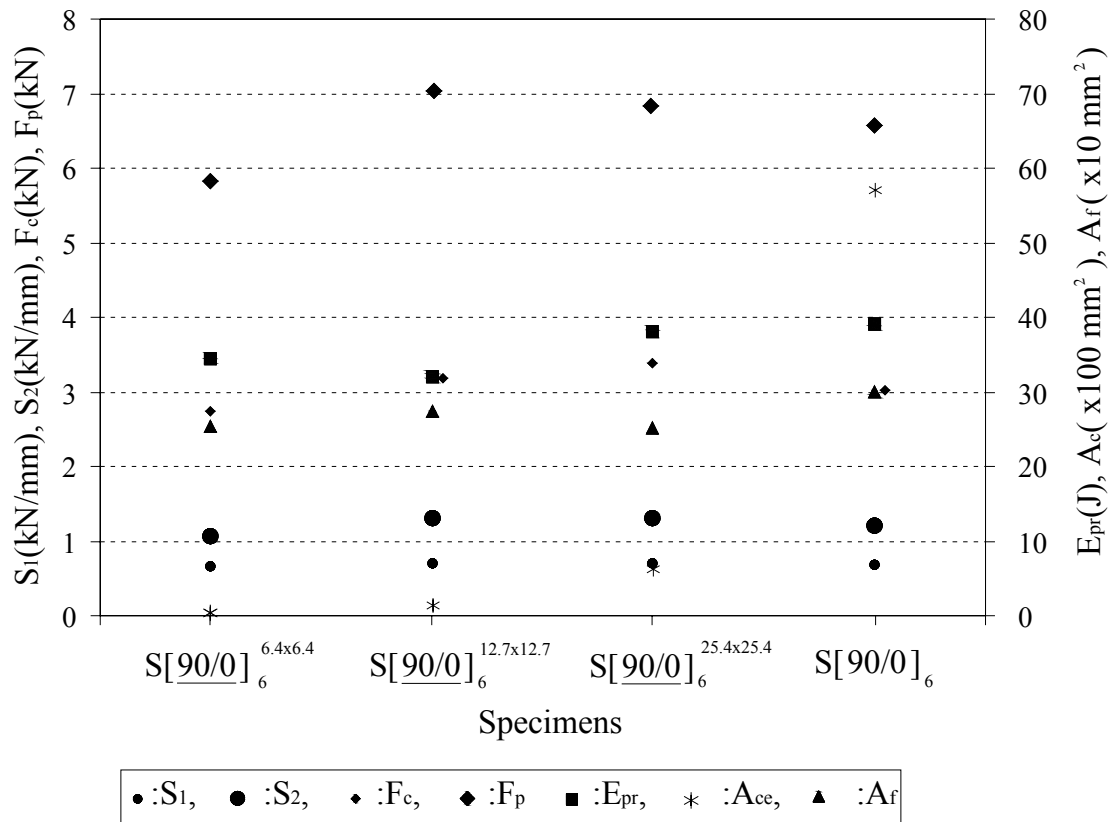


Figure 5.22 Comparison of impact response of stitched composites with various cell sizes.

The failure mechanism of the stitched composites is similar to the unstitched composites with the same cell size. However, the bottom layer of the $S[90/0]_6$ composite is held by the stitching thread and is not torn away from the composite. There are some fiber breakages as can be seen in Fig. 5.23. The damage of the $S[90/0]_6^{25.4 \times 25.4}$ composite is also localized by stitches. The delamination area of this composite is smaller than the corresponding unstitched ones. The damage size of the $S[90/0]_6^{12.7 \times 12.7}$ and $S[90/0]_6^{6.4 \times 6.4}$ composites are increased by stitching. Among the stitched composites, the delamination size in the bottom interface is the largest in the $S[90/0]_6$ composite, follows by $S[90/0]_6^{12.7 \times 12.7}$ and then by $S[90/0]_6^{25.4 \times 25.4}$ and $S[90/0]_6^{6.4 \times 6.4}$ composites.

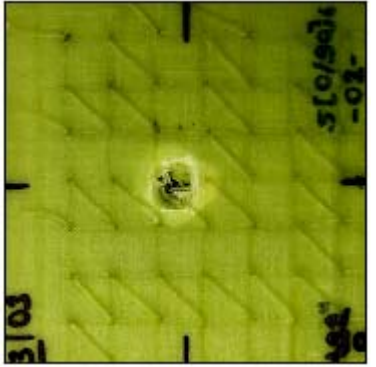

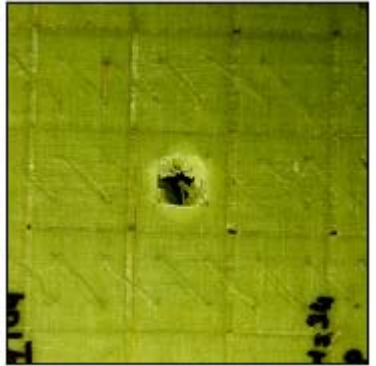

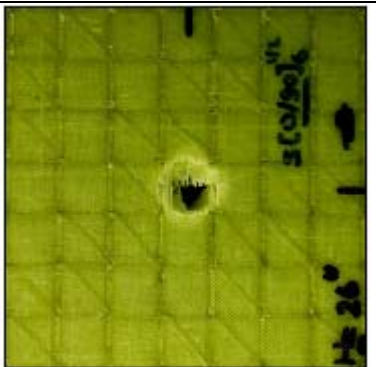
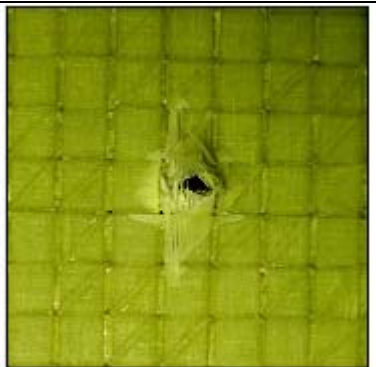
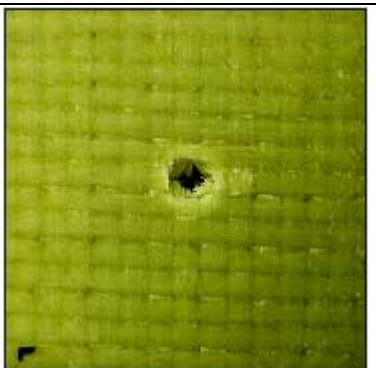

SPECIMEN	TOP	BOTTOM
$S[90/0]_6$		
$S[90/0]_6^{25.4 \times 25.4}$		
$S[90/0]_6^{12.7 \times 12.7}$		
$S[90/0]_6^{6.4 \times 6.4}$		

Figure 5.23 Top and bottom images of damaged woven composites.

5.7 Angle between Fill and Warp Effect

Two dimensional weaving using 25.4 mm and small angle between the fill and the warp directions such as 15°, posed some challenge. Because warp strips could slide easily between fill strips and distort the weaving pattern. For this reason, 12.7 mm strips were selected for weaving with an angle. The composites were woven with the following angles 60°, 45°, 30° and 15°.

The typical force-deflection curves of the $[\underline{60}/0]_6^{12.7 \times 12.7}$, $[\underline{45}/0]_6^{12.7 \times 12.7}$, $[\underline{30}/0]_6^{12.7 \times 12.7}$ and $[\underline{15}/0]_6^{12.7 \times 12.7}$ composites with that of the $[\underline{90}/0]_6^{12.7 \times 12.7}$ composite are given for comparison in Figure 5.24. From this figure, it is seen that, the first bending stiffness, the second bending stiffness and critical force increase with increasing angle between fill and warp strips of the composite. When the angle decreases, peak force value also decrease except for the $[\underline{90}/0]_6^{12.7 \times 12.7}$. The $[\underline{60}/0]_6^{12.7 \times 12.7}$ composite has the highest peak force while the $[\underline{15}/0]_6^{12.7 \times 12.7}$ composite has the lowest. The $[\underline{60}/0]_6^{12.7 \times 12.7}$ composite has the sharpest force-deflection curve. A sudden decrease in force occurred right after the peak force. This decrease become less steep as the angle between the fill and the warp strips become smaller. In fact, the force-deflection curve of the $[\underline{15}/0]_6^{12.7 \times 12.7}$ seems to have double peaks. Besides, it is found that the deflection at perforation increases with the decrease of angle between the strips.

The energy profiles of the $[\underline{90}/0]_6^{12.7 \times 12.7}$, $[\underline{60}/0]_6^{12.7 \times 12.7}$, $[\underline{45}/0]_6^{12.7 \times 12.7}$, $[\underline{30}/0]_6^{12.7 \times 12.7}$ and $[\underline{15}/0]_6^{12.7 \times 12.7}$ composites are shown in Figure 5.25. From this Figure, the $[\underline{15}/0]_6^{12.7 \times 12.7}$ composite has highest absorbed energy for perforation, followed by the $[\underline{30}/0]_6^{12.7 \times 12.7}$, and then by the $[\underline{45}/0]_6^{12.7 \times 12.7}$ composite. The $[\underline{90}/0]_6^{12.7 \times 12.7}$ and $[\underline{60}/0]_6^{12.7 \times 12.7}$ composites have similar absorbed energy for perforation values. The perforation threshold values are given in the Figure 5.26.

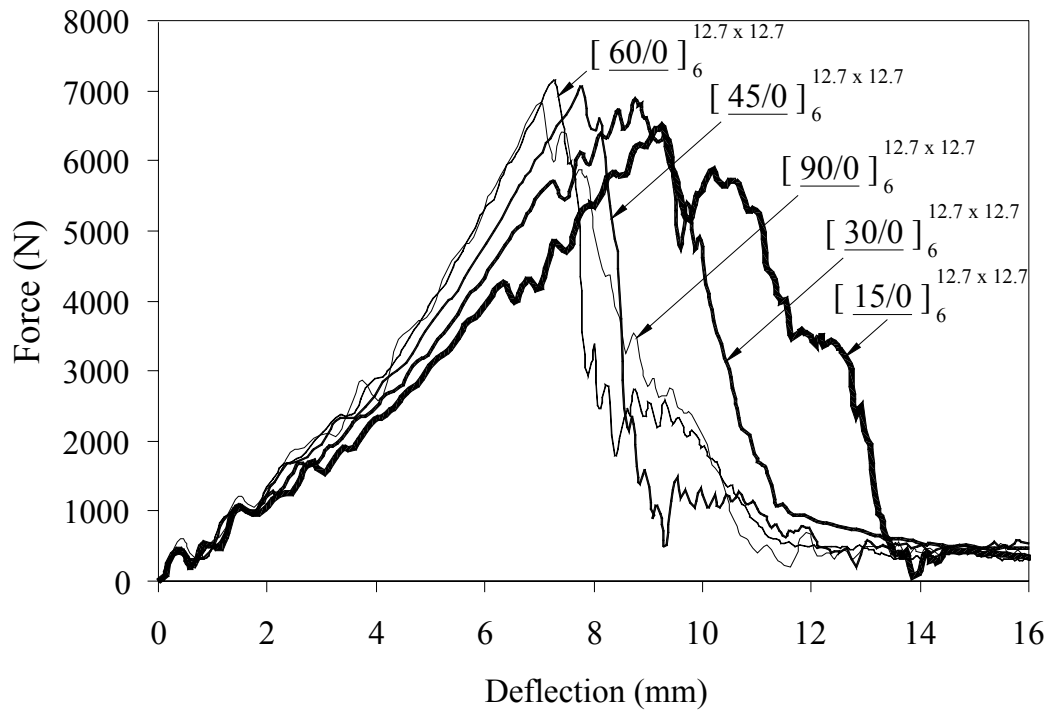


Figure 5.24 Typical force-deflection curves for woven composites with various weaving angles.

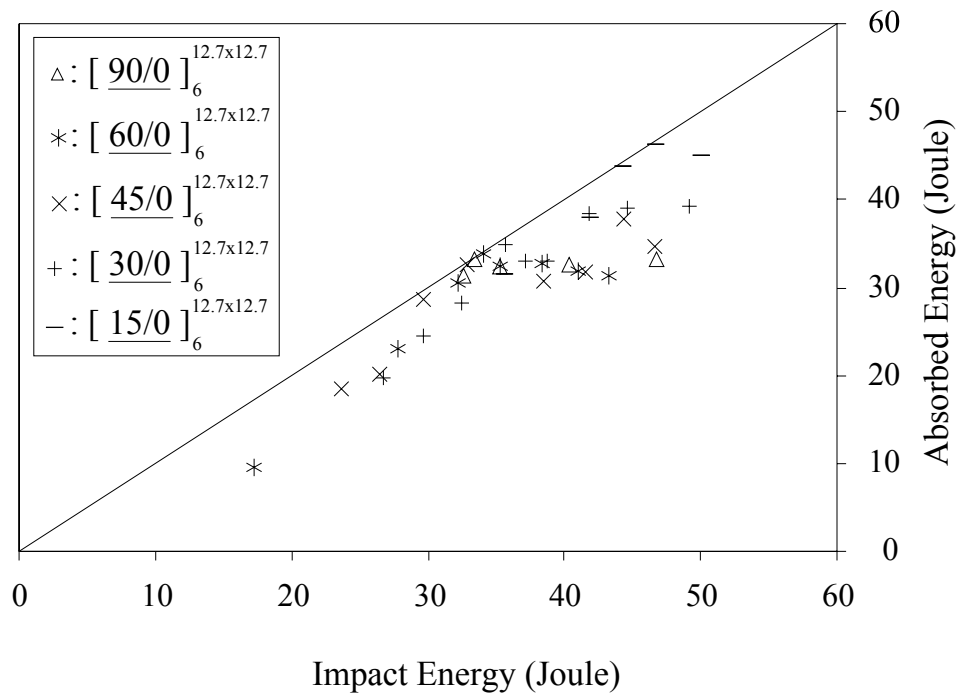


Figure 5.25 Energy profiles for the $[\underline{90/0}]_6^{12.7 \times 12.7}$, $[\underline{60/0}]_6^{12.7 \times 12.7}$, $[\underline{45/0}]_6^{12.7 \times 12.7}$, $[\underline{30/0}]_6^{12.7 \times 12.7}$ and $[\underline{15/0}]_6^{12.7 \times 12.7}$ composites.

The bending stiffnesses, critical force, peak force, perforation threshold, impacted cell area, failure area values of all woven composites with various weaving angle are given in Figure 5.26 for comparison. When the angle between the fill and the warp strips of the woven composite decrease the first and second bending stiffnesses, critical force, and subsequently the peak force also decrease. Because the composite become more polarized along the fill strips, i.e. 0° -direction. The perforation threshold is also dependent on the angle between the fill and the warp strips.

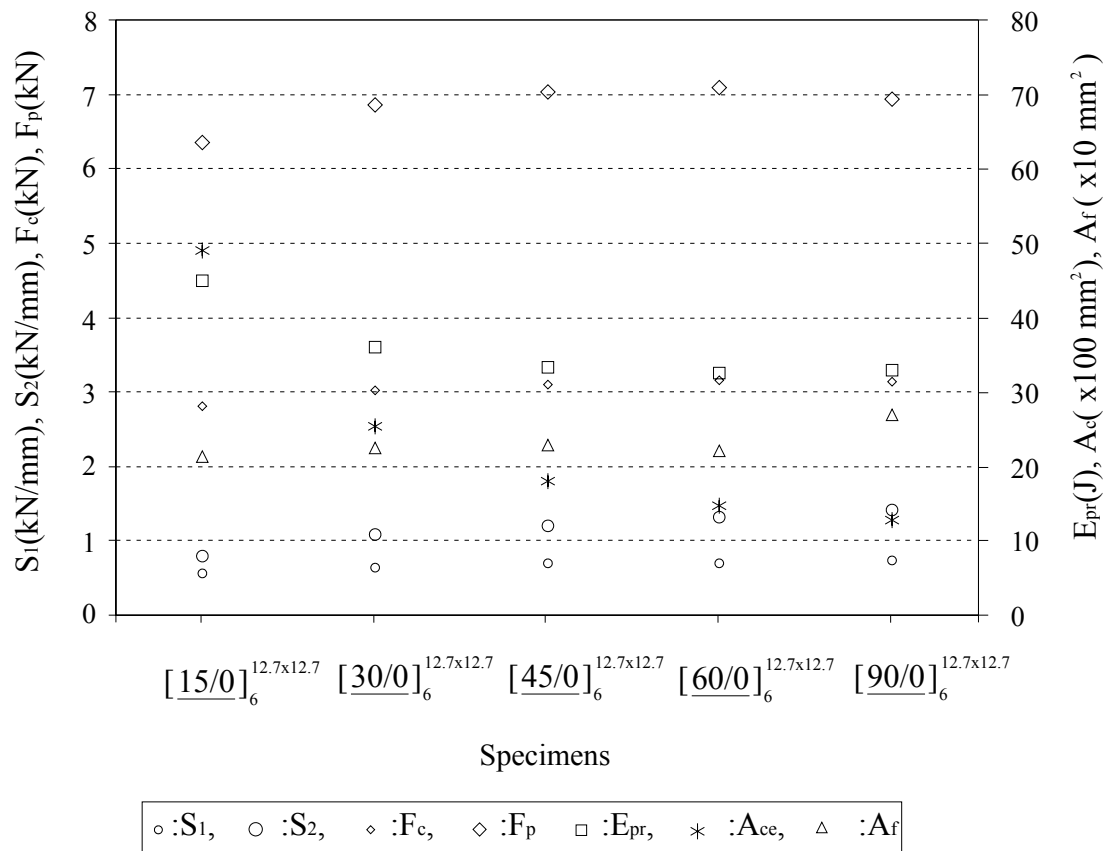


Figure 5.26 Comparison of impact response of composites with various angles between fill and warp.

The failure mechanisms in these composites are similar. The minor matrix cracks occurred on the top and bottom lamina under low impact energy. There are delaminations in the interfaces, especially in the bottom. As the impact energy increase the fibers are broken along the short diagonal of the impacted cell through the thickness can be seen in Figure 5.27. With additional impact energy, new matrix cracks and fiber cracks occur. The cell edges especially near the two corners which are the ends of the short diagonal confine the improvement of the failure. The failure of the $[60/0]_6^{12.7 \times 12.7}$ composite is smallest because of the smallest area of the cell. The $[15/0]_6^{12.7 \times 12.7}$ composite has the largest failure area.

5.8 Numerical Results

The finite element code can be used for determining the contact force between impactor and the composite, the deflection of the composite, stress and strains values of the composite and the delamination in the composite materials. However the code cannot find the fiber breakage of the specimen. It means that, the penetrated, perforated and rebounded specimens in which fiber breakage occurred can not be solve with this finite element code. Additionally, the code is capable for solving the laminated composite with consists of unidirectional laminas not woven.

As can be seen in Section 5.3 and Appendix, two specimen of the $[90/0]_6$ composite and two specimen of the $[30/0]_6$ composite can be used for comparison of the experimental and numerical study under the conditions mentioned above. None of the specimens of $[15/0]_6$ were convenient for applying code.









SPECIMEN	TOP	BOTTOM
$[15/0]_6^{12.7 \times 12.7}$		
$[30/0]_6^{12.7 \times 12.7}$		
$[45/0]_6^{12.7 \times 12.7}$		
$[60/0]_6^{12.7 \times 12.7}$		

Figure 5.27 Top and bottom images of damaged woven composites with various weaving angle.

The three dimensional finite element mesh of a laminated composite plate is given in Figure 5.28. An eight point brick element is used for meshing. The laminate is divided into $N \times M \times Q$ elements. The laminate thickness divided Q elements and the other dimensions divided N and M elements. The finer mesh was used for the impact region. Choi & Chang (1992) investigated on the effect of finite element mesh size on the stability of the numerical prediction based on the model. They found that the propose failure analysis did not require the use of an extensive fine mesh. Hence, $N=14$, $M=14$ and $Q=4$ were selected for finite element mesh. Total number of element is 784 can be calculated by using the formula $N=14 \times M=14 \times Q= 4$.

In experiment, the dimensions of the composite were 100 mm x 100 mm. However, as can be seen in Figure 3.14, some areas are used for clamping. Remaining area for impact on composite plate is 76.2 mm x 76.2 mm. These dimensions were used for finite element modeling shown in Figure 5.28. All of the edges of the plate were clamped.

The mechanical properties of the unidirectional composite layer used in experimental study are given in Table 5.1.

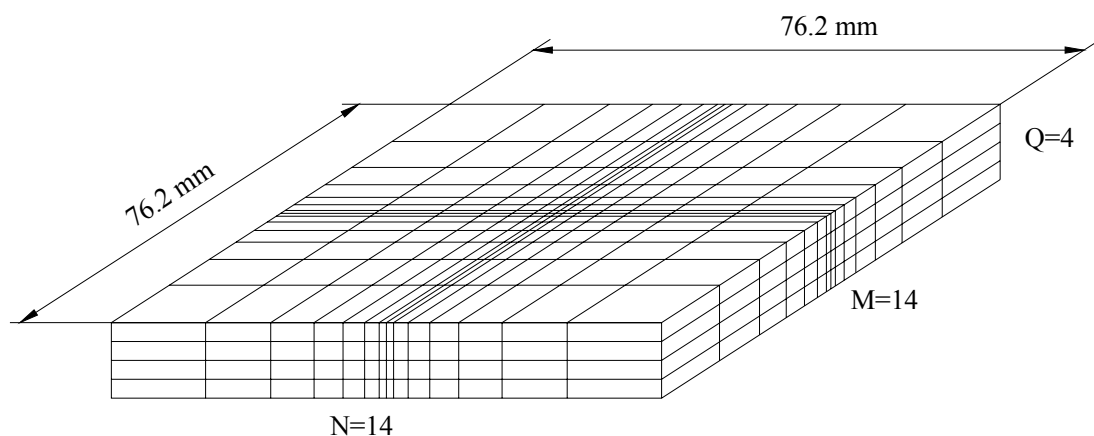


Figure 5.28 Finite element mesh of the composite plate

Table 5.1 Mechanical properties of a unidirectional layer

Property	Symbol	Value
Fiber volume fraction	V_f	55 %
Density	ρ	1.76 gr/cm ³
Longitudinal modulus	E_1	39.0 GPa
Transverse modulus	E_2	8.6 GPa
In-plane shear modulus	G_{12}	3.8 GPa
Poisson's ratio	ν_{12}	0.28
Longitudinal tensile strength	X_t	1080 MPa
Longitudinal compressive strength	X_c	620 MPa
Transverse tensile strength	Y_t	39 MPa
Transverse compressive strength	Y_c	128 MPa
In-plane shear strength	S	89 MPa
Interlaminar shear strength	S_i	35 MPa

The numerical force versus time curve of the $[90/0]_6$ composite subjected to impact loading with experimental curve for comparison is given in Figure 5.29. The velocity of the impactor right before the contact between composite and impactor nose was 2.35 m/sec. From this figure, it is seen that the general behaviors of the curves are similar. However, the peak force of numerical curve is higher than experimental curve while the contact time is smaller.

The force-time curves of the $[90/0]_6$ composite impacted by impactor with 2.91 m/sec velocity are given in Figure 5.30. The ascending sections of the curves are similar to the ascending section of the curves given in Figure 5.29. After the ascending section the experimental force decreases suddenly. The specimen has fiber breakage in the experiment. However numerical study investigates only matrix cracking and delamination. Therefore the numerical solution is not convenient for comparison with the experimental results under this impactor velocity.

The delamination in each interface of the $[90/0]_6$ composite impacted by impactor with 2.91 m/sec velocity are given in Figure 5.31-a. There are no delamination in

interface of 4, 5, 6 and 7. From this figure, it is seen that, the largest delamination in the bottom interface. The longitudinal axis of the delamination in each interface tends to orient itself in the direction parallel to the fiber direction of the layer below interface. The total delamination is shown in Figure 31-b. The total delamination can be compared with the photos given in Figure 32.

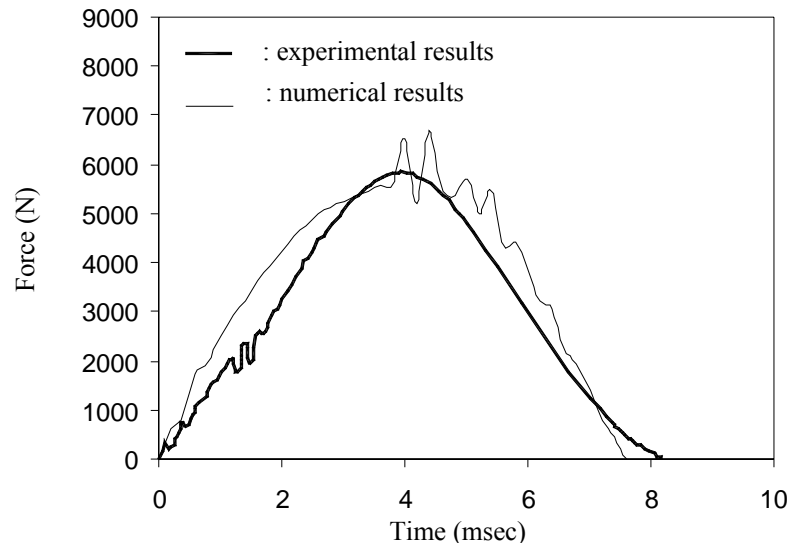


Figure 5.29 Experimental and numerical force-time curves of the $[90/0]_6$ composite plates (impactor velocity=2.35 m/sec)

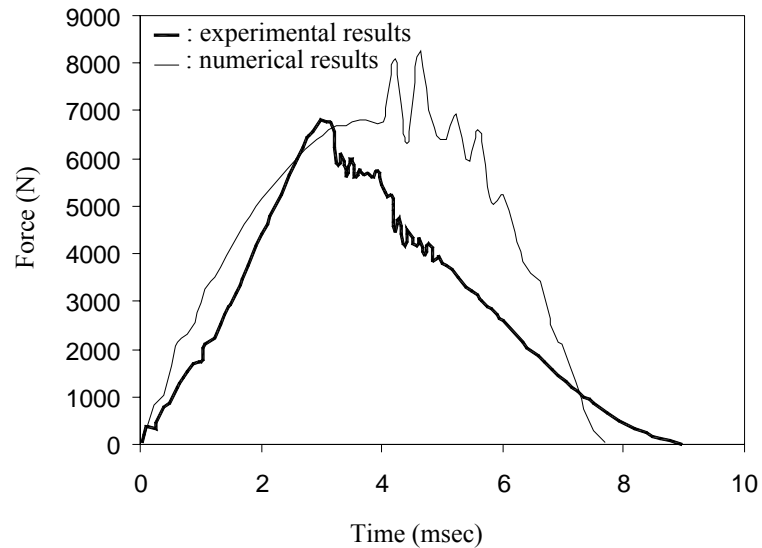


Figure 5.30 Experimental and numerical force-time curves of the $[90/0]_6$ composite plates (impactor velocity=2.91 m/sec)

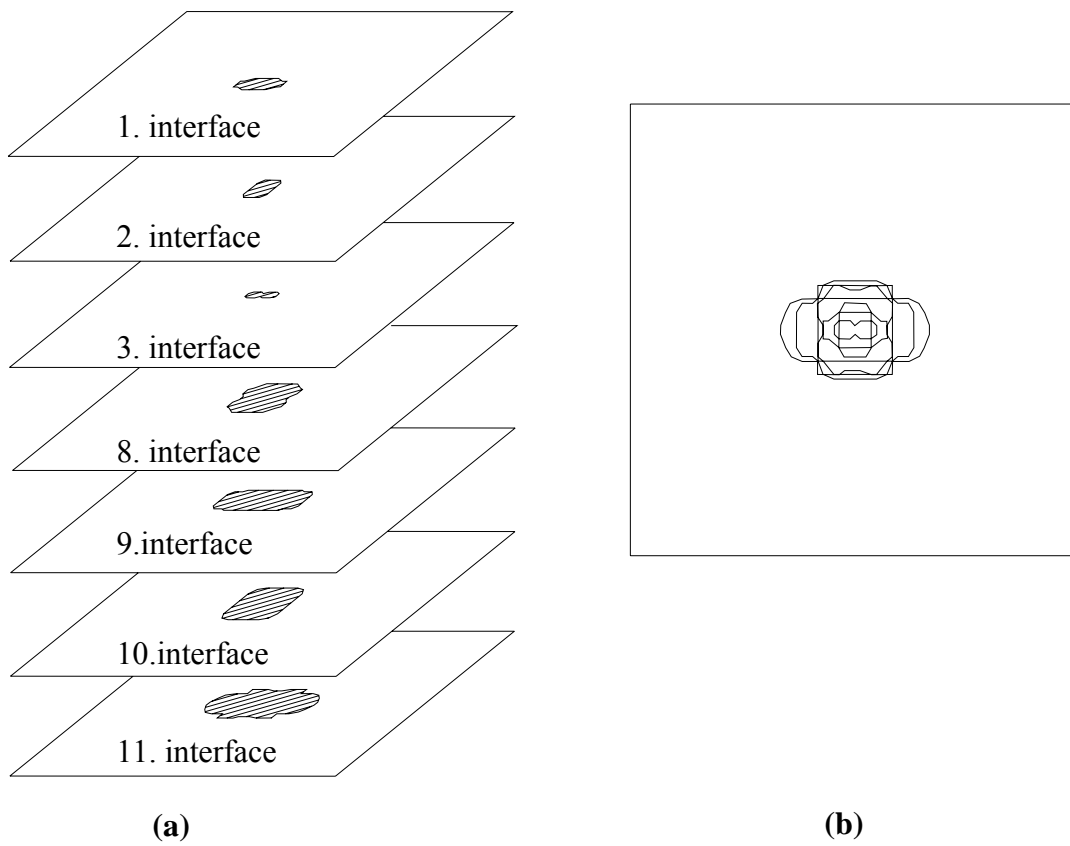


Figure 5.31 (a) Delamination in the interfaces, (b) total delamination, of the $[90/0]_6$ composite plates

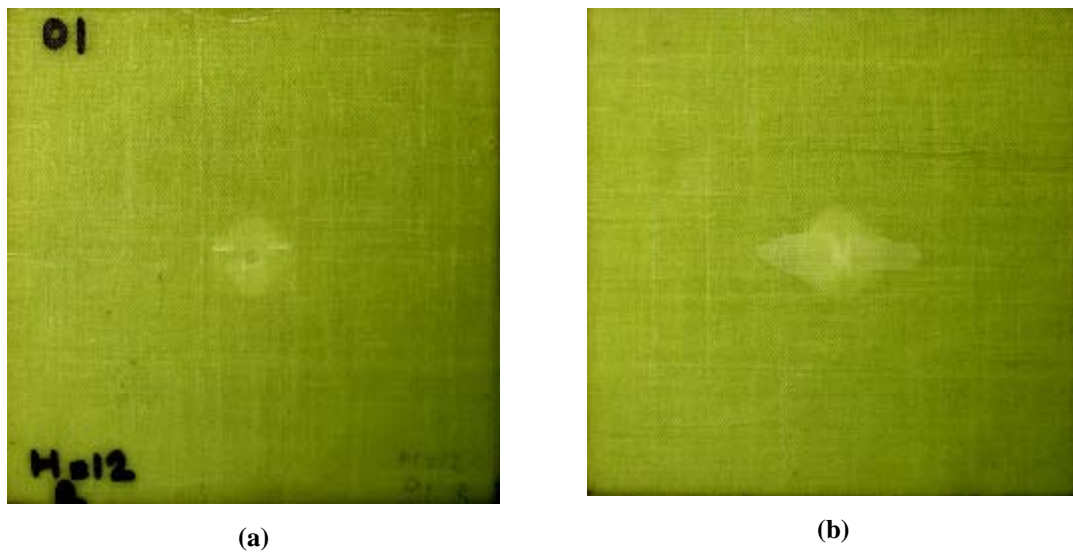


Figure 5.32 (a) Top and (b) bottom images of the $[90/0]_6$ composite plates

The force-time curves of the $[30/0]_6$ composite impacted by impactor with 2.47 m/sec and 2.91 m/sec velocities right before the contact are given in Figure 5.33 and Figure 5.34, respectively. The experimental and numerical curves have similar behaviors. The numerical curves have higher force values than experimental curves. In both cases the contact durations are higher for experimental results.

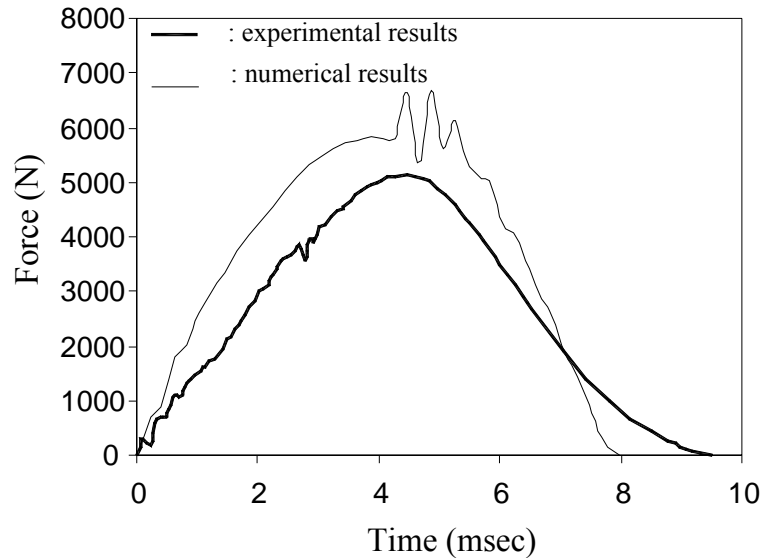


Figure 5.33 Experimental and numerical force-time curves of the $[30/0]_6$ composite plates (impactor velocity=2.47 m/sec)

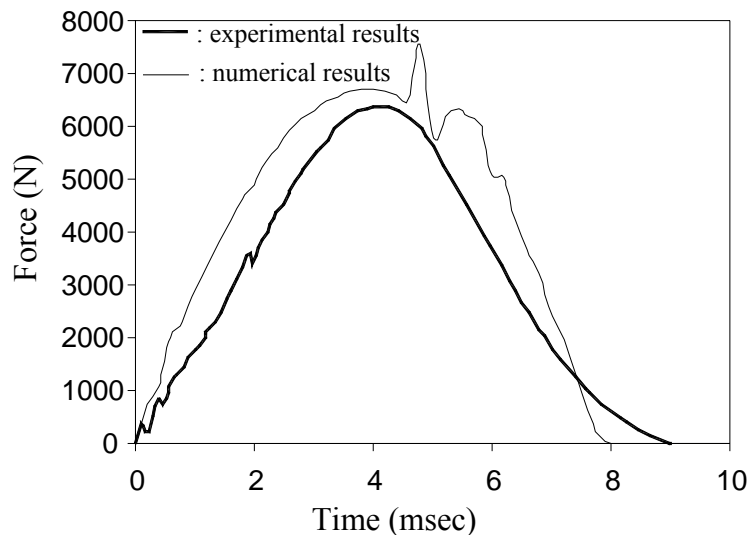


Figure 5.34 Experimental and numerical force-time curves of the $[30/0]_6$ composite plates (impactor velocity=2.91 m/sec)

Generally, the numerical results and experimental results were similar for situation of low impact velocity resulting in low impact energy. The computer code can be used for the specimen subjected to low energy impact which produces only delamination. Additionally, the reason of difference between the numerical and experimental results may be explained the mechanical properties used in numerical study are taken from a technical datasheet.

CHAPTER SIX

CONCLUSIONS

In this study, the effects of angle between adjacent layers, weaving gaps, curing pressure, cell size, stitching, and angle between fill and warp strips on impact behavior of composite plates were investigated. From this study, it is concluded that:

- Both the bending stiffnesses and the peak force decrease with decrease of the angle between adjacent layers while the perforation threshold and the maximum deflection increase.
- The woven composite with gap between cells and low curing pressure shows better impact properties than the other composites produced with varied gap and pressure.
- The impact-induced bending stiffnesses are similar for woven composites with varied cell sizes, so is the maximum deflection. When the cell size is equal to the diameter of the impactor nose, the absorbed energy value is the smallest, implying the confinement of the cell boundary on the damage expansion.
- Stitching generally does not change peak force and perforation threshold while the stitching points are located on the cell corners. However, they decrease if the stitching points are located within the cell. The first bending stiffness value does not change but the second bending stiffness value becomes lower with stitching for all cell sizes.
- As the weaving angle between the fill and the warp strips decrease, bending stiffnesses and peak force decrease; whereas maximum deflection and absorbed energy increase.
- For the composites consist of unidirectional layers and under the low impact energy condition, the numerical and experimental results were found to be similar.

In the future, it is intended and recommended to investigate the effect of:

- weaving angle on the mechanical properties of woven fabric composites.
- weaving with different fill and warp strips in width on impact response of composites.
- stitching density, stitching pattern and the type of thread used in stitching on impact response of composite plates.

REFERENCES

- Abatan, A., Hu, H., & Olowokere, D. (1998). Impact resistance modelling of hybrid laminated composites. *Journal of Thermoplastic Composite Materials*, 11, 249- 260.
- Abrate, S. (1991). Impact on laminated composite materials. *Applied Mechanics Review*, 44, 155-190.
- Abrate, S. (1994). Impact on laminated composites: Recent Advances, *Applied Mechanics Review*, 47, 517-544.
- Abrate, S. (1998). *Impact on composite structures*. Cambridge: Cambridge University Press.
- Aslan, Z. & Karakuzu, R. (2002). Transient dynamic analysis of laminated composite plate subjected to low- velocity impact. *Mathematical & Computational Applications*, 7-2, 73-82.
- Aslan, Z., Karakuzu, R. & Sayman, O. (2002). Dynamic characteristics of laminated woven e-glass-epoxy composite plates subjected to low velocity heavy mass impact. *Journal of Composite Materials*, 36, 2421-2442.
- Aslan, Z., Karakuzu, R. & Buket, O. (2003). The response of laminated composite plates under low-velocity impact loading. *Composites Science and Technology*, 59, 119-127.
- Ataş, C. (2004). *Large deformations in composite laminated plates*. PhD Thesis, Dokuz Eylül University.
- Baucom, J. N., Zikry, M. A. & Qiu, Y. (2004) Dynamic and quasi-static failure evolution of 3D woven cellular composite systems. *Journal of Reinforced Plastics and Composites*, 23, 471-481.

- Baucom, J. N. & Zikry, M. A. (2005). Low-velocity impact damage progression in woven e-glass composite systems. *Composites Part A*, 36, 658-664.
- Carlsson, L. A. & Pipes, R. B. (1997). *Experimental characterization advanced composite materials* (2 nd ed.). Pennsylvania: Technomic Publishing Company.
- Cantwell, W. J. & Morton, J. (1991). The impact resistance of composite materials- a review. *Composites*, 22, 347-362.
- Chen, G., Li, Z., Kou, C. & Gui, L. (2004). Finite element analysis of low-velocity impact damage of stitched laminates. *Journal of Reinforced Plastics and Composite*, 23, 987-995.
- Choi, H. Y., Downs, R. J. & Chang, F. K. (1991). A new approach toward understanding damage mechanisms and mechanics of laminated composites due to low-velocity impact, Part I-Experiments. *Journal of Composite Material*. 25, 992-1011.
- Choi, H. Y., Wu, H. Y. T. & Chang, F. K. (1991). A new approach toward understanding damage mechanisms and mechanics of laminated composites due to low-velocity impact, Part II-Analysis. *Journal of Composite Materials*, 25, 1012-1038.
- Choi, H. Y., & Chang, F. K. (1992). A model for predicting damage in graphite/epoxy laminated composites resulting from low-velocity point impact. *Journal of Composite Materials*, 26 (14), 2134-2169.
- Choi, I. H., & Hong, C. S. (1994). New approach for simple prediction of impact force history on composite laminates. *AIAA Journal*, 32, 2067-2072.
- Chang, F. K. & Lessard, L. B. (1991). Damage tolerance of laminated composites containing an open hole and subjected to compressive loading: Part I- Analysis. *Journal of Composite Materials*, 25, 2-43.

- Coppens, G. J. (2004). *Effects of three-dimensional geometry on penetration and perforation resistance.*, MSc. Thesis, Michigan State University.
- Curtis, P. T. & Bishop, S. M. (1984). An assessment of the potential of woven carbon fiber-reinforced plastics for high performance applications. *Composites*, 15, 259-265.
- Freitas, M., Silva, A., & Reis, L. (2000). Numerical evaluation of failure mechanisms on composite specimens subjected to impact loading. *Composites: Part B*, 31, 199- 207.
- Gibson, R. F. (1994). *Principles of Composite Material Mechanics*. Singapore: McGraw-Hill
- Gillespie JR, J. W. & Monib, A. M., Carlsson, L. A. (2003). Damage tolerance of thick-section S-2 glass fabric composites subjected to ballistic impact loading. *Journal of Composite Material*. 37, 2131-2147.
- Netcomposites. (nd). *Guide to composite*. Retrieved April 21, 2006, from <http://www.netcomposites.com>.
- Hertz, O. (1982). Ueber die Berührung fester elastischer Körper. *Journal fur die Reine und Angewandte Mathematic*, 92, 156-171.
- Hosur, M. V., Karim, M. R. & Jeelani, S. (2003). Experimental investigations on the response of stitched/unstitched woven S2-Glass/SC15 Epoxy composites under single and repeated low velocity impact loading. *Composite Structures*, 61, 89-102.
- Hosur, M.V., Adya, M., Alexander, J. & Jeelani, S. (2004). Studies on impact damage resistance of affordable stitched woven carbon/epoxy composite laminates. *Journal of Reinforced Plastics and Composite*, 22, 927-952.
- Hosur, M.V., Vaidya, U.K., Ulven, C. and Jeelani, S. (2004). Performance of stitched/unstitched woven carbon/epoxy composites under high velocity impact loading. *Composite Structures*, 64, 455-466.

- Hou, J. P., Petrinic, N., Ruiz, C., & Hallett, S.R. (2000). Prediction of impact damage in composite plates. *Composites Science and Technology*, 60, 273-281.
- Jenq, S. T., Jing, H. -S. & Chung, C. (1994). Predicting the ballistic limit for plain woven glass/epoxy composite laminate. *International Journal of Impact Engineering*, 15, 451-464.
- Joshi, S. P., & Sun, C. T. (1987). Impact-induced fracture initiation and detailed dynamic stress field in the vicinity of impact. *Proc. American Society of Composites 2nd Tech. Conf.* 177-185.
- Kang, T. J. & Lee, S. H. (1994). Effect of stitching on the mechanical and impact properties of woven laminate composite. *Journal of Composite Materials*, 28, 1574-1587.
- Kim, J. K. & Sham, M. L. (2000). Impact and delamination failure of woven-fabric composites. *Composites Science and Technology*, 60, 745-761.
- Kim, J. K., & Kang, K. W. (2001). An analysis of impact force in plain-weave glass/epoxy composite plates subjected to transverse impact. *Composites Science and Technology*, 61, 135-143.
- Larsson, F. (1997). Damage tolerance of a stitched carbon/epoxy laminate. *Composites Part A*, 28A, 923-934.
- Lee, J. D., Du, S., & Liebowitz, H. (1984). Three dimensional finite element and dynamic analysis of composite laminate subjected to impact. *Computers & Structures*, 19, 807-813.
- Lesser, A. J. & Filippov, A. G. (1991). Kinetics of damage mechanisms in laminated composites. *International SAMPE Symposium and Exhibition*, 36, 886-900.

- Liu, D. & Malvem, L. E. (1987). Matrix cracking in impacted glass/ epoxy plates. *Journal of Composite Materials*, 21, 594-609.
- Liu, D. (1988). Impact- induced delamination- a view of bending stiffness mismatching. *Journal of Composite Materials*, 22, 674-692.
- Liu, D. & Raju, B. B. (2000). Effects of joining techniques on impact perforation resistance of assembled composite plates. *Experimental Mechanics*, 40, 46-53.
- Liu, D., Raju, B. B. & Dang, X. (2000). Impact perforation resistance of laminated and assembled composite plates. *International Journal of Impact Engineering*, 24, 733-746.
- Liu, D. (2004). Characterization of impact properties and damage process of glass/epoxy composite laminates. *Journal of Composite Material*,. 38, 1425-1442.
- Lopresto, V., Melito, V. Leone, C. & Caprino, G. (2006). Effect of stitches on the impact behavior of graphite/epoxy composites. *Composite Science and Technology*, 66, 206-214.
- Mallick, P. K. (1993). *Fiber-reinforced composites*, (2 rd ed.). NY: Marcel Dekker.
- Mouritz, A. P. & Cox, B. N. (1997). A mechanistic approach to the properties of stitched laminates. *Composite Part A: Appl Sci Eng.*, 31, 1-27.
- Naik, N.K. & Sekher, Y. C. (1998). Damage in laminated composites due to low velocity impact. *Journal of Reinforced Plastics and Composites*, 17, 1232-1263.
- Naik, N. K., Sekher, Y. C. & Meduri, S. (2000). Damage in woven-fabric composites subjected to low-velocity impact. *Composites Science and Technology*, 60, 731-744.
- Naik, N. K., Borade, S. V., Arya, H., Sailendra, M. & Prabhu, S.V. (2002). Experimental studies on impact behavior of woven fabric composites: effect of impact parameters. *Journal of Reinforced Plastics and Composite*, 21, 1347-1362.

- Pierson, M. O., & Vaziri, R. (1996). Analytical solution for low-velocity impact response of composite plates. *AIAA Journal*, 34, 1633-1640.
- Ramkumar, R. L., & Chen, P. C. (1982). Low-velocity impact response of laminated plates. *AIAA Journal*, 21, 1448-1452.
- Reeder, J. R. (1995). Stitching vs. a toughed matrix: compressive strength effects. *Journal of Composite Materials*, 29, 2464-2487.
- Sankar, B. V., & Sun, C. T. (1985). Low-velocity impact response of laminated beams subjected to initial stresses. *AIAA Journal*, 23, 1962-1969.
- Sharma, S. K. & Sankar, B. V. (1997). Effect of stitching on impact and interlaminar properties of graphite/epoxy laminates. *Journal of Thermoplastic Composite Material*, 10, 241-253.
- Shiow, Y. P. & Shim, V. P. (1998). An experimental study of low velocity impact damage in woven fiber composites. *Journal of Composite Materials*, 32, 1178-1202.
- Shivakumar, K. N., Elber, W., & Illg, W. (1985). Prediction of low-velocity impact damage in thin circular laminates. *AIAA Journal*, 23, 442-449.
- Sjoblom, P. O., Hartness, J. T. & Cordell, T. M. (1988). On low velocity impact testing of composite materials. *Journal of Composite Materials*, 22, 30-52.
- Sun, C. T., & Yang, S. H. (1980). *Contact law and impact responses of laminated composites*. NASA CR-159884, National Aeronautical and Space Administration, Washington, D.C.
- Sutherland, L. S. & Soares, C. G. (1999). Impact tests on woven-roving e-glass/polyester laminates. *Composites Science and Technology*, 59, 1553-1567.

Tan, T. M. & Sun, C. T. (1985). Use of statical indentation laws in the impact analysis of laminated composite plates. *Journal of Applied Mechanics*, 52, 6-12.

Wu, H. Y., & Chang, F. K. (1989). Transient dynamic analysis of laminated composite plates subjected to transverse impact. *Computers and Structures*, 31 (3), 453-466.

Zienkiewicz, O. C. (1977). *The finite element method* (3 rd ed.). NY: McGraw-Hill.

APPENDIX

The typical curves of each statement of the composite specimen subjected to impact loading are given in Results and Discussion section. However, there are no details about each experiment. In this section, all of the curves of the experiments and impact velocities are given as follows:

Table A.1 Impact velocities of the $[90/0]_6$ composite specimens

$[90/0]_6$	Specimen Number					
	1	2	3	4	5	6
Velocity (m/sec)	2.35	2.91	3.52	3.65	3.90	3.98

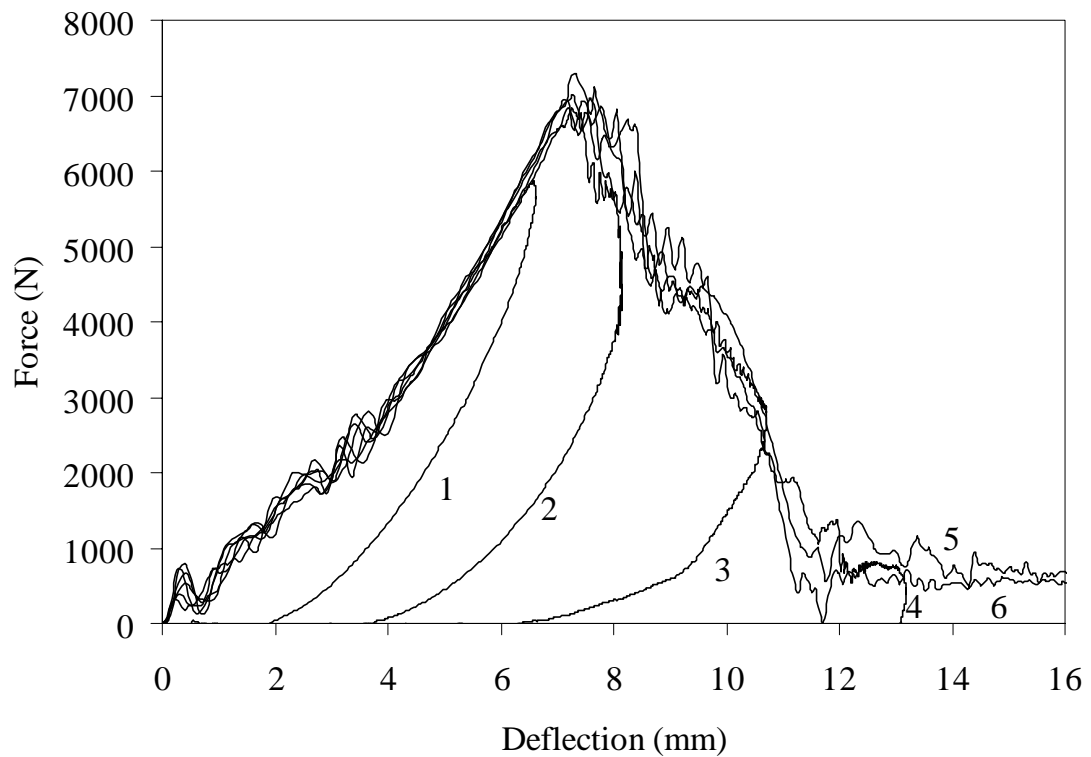


Figure A.1 Force-deflection curves of the $[90/0]_6$ composite plates

Table A.2 Impact velocities of the $[30/0]_6$ composite specimens

$[30/0]_6$	Specimen Number				
	1	2	3	4	5
Velocity (m/sec)	2.47	2.91	3.76	4.10	4.15

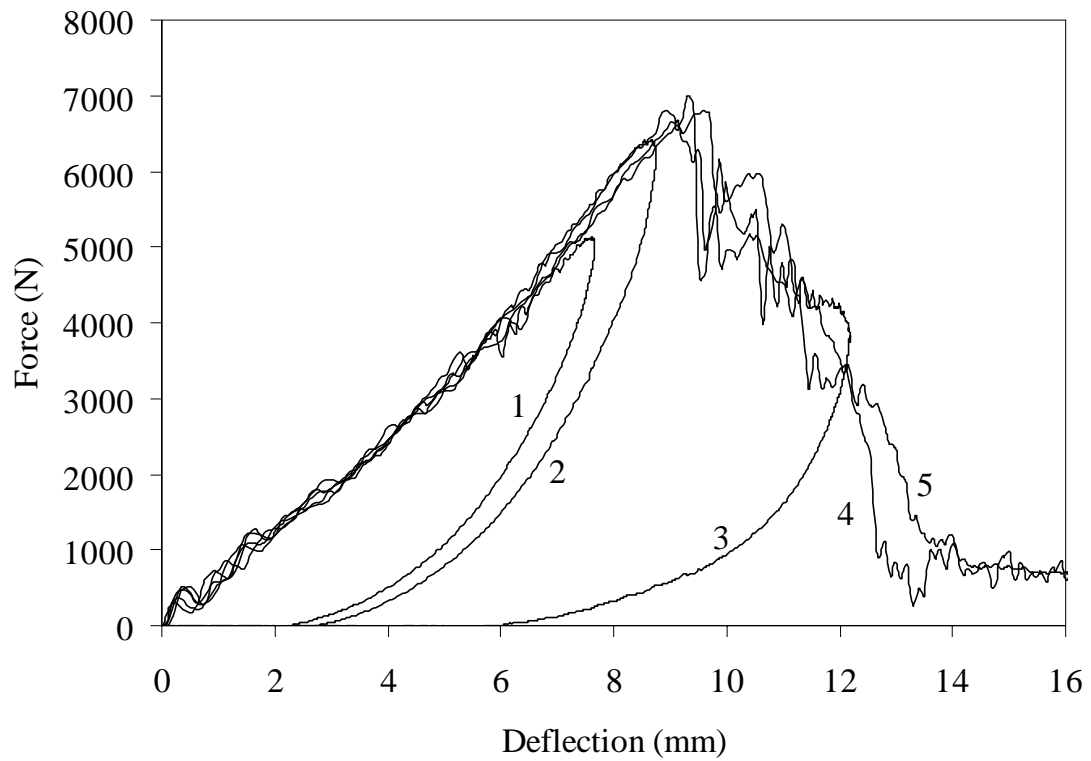
Figure A.2 Force-deflection curves of the $[30/0]_6$ composite plates

Table A.3 Impact velocities of the $[15/0]_6$ composite specimens

$[15/0]_6$	Specimen Number				
	1	2	3	4	5
Velocity (m/sec)	3.41	3.76	3.94	4.11	4.18

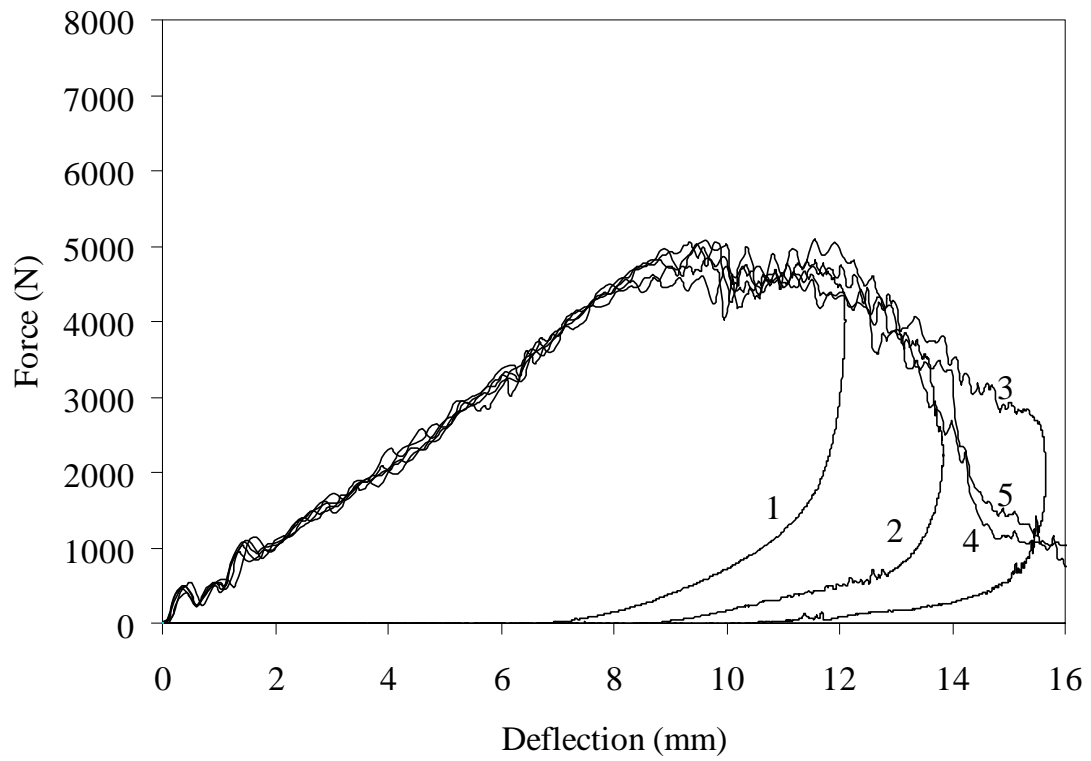
Figure A.3 Force-deflection curves of the $[15/0]_6$ composite plates

Table A.4 Impact velocities of the $[\underline{90/0}]_4^{25.4 \times 25.4}$ composite specimens produced with gap and cured under high pressure (HP₁)

$[\underline{90/0}]_4^{25.4 \times 25.4}$ HP ₁	Specimen Number				
	1	2	3	4	5
Velocity (m/sec)	2.89	3.08	3.16	3.31	3.44

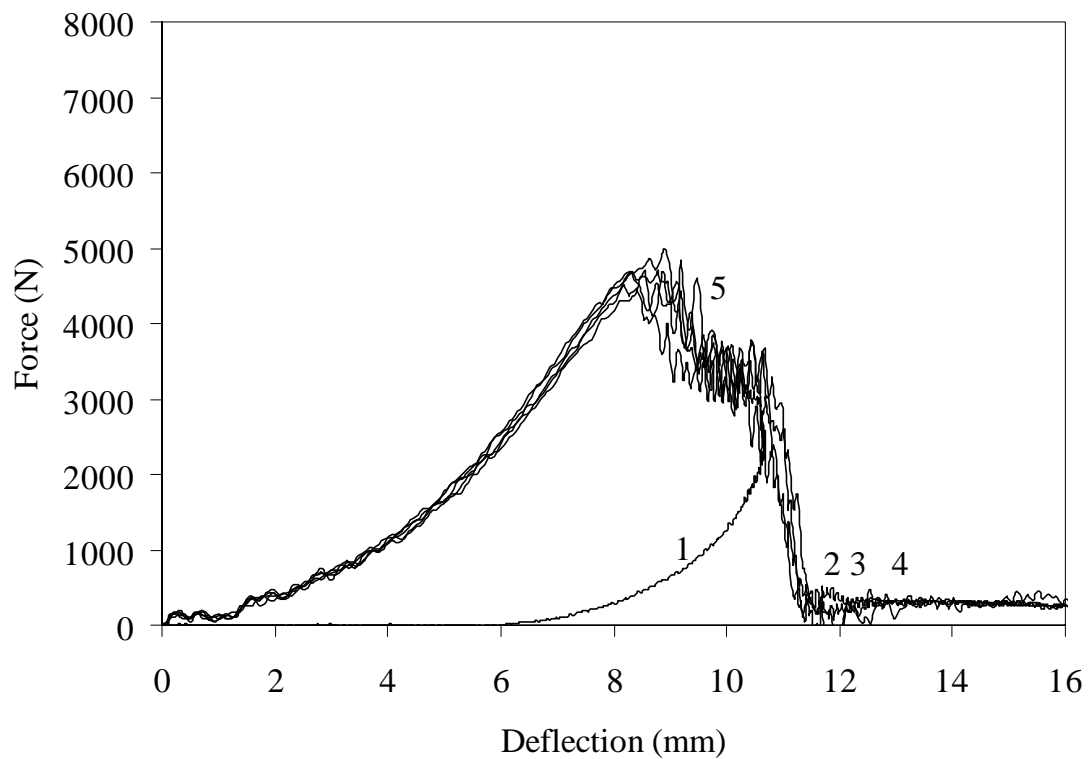


Figure A.4 Force-deflection curves of the $[\underline{90/0}]_4^{25.4 \times 25.4}$ composite plates produced with gap and cured under high pressure (HP₁)

Table A.5 Impact velocities of the $[\underline{90/0}]_4^{25.4 \times 25.4}$ composite specimens produced without gap and cured under high pressure (HP₂)

$[\underline{90/0}]_4^{25.4 \times 25.4}$ HP ₂	Specimen Number			
	1	2	3	4
Velocity (m/sec)	2.92	2.98	3.08	3.14

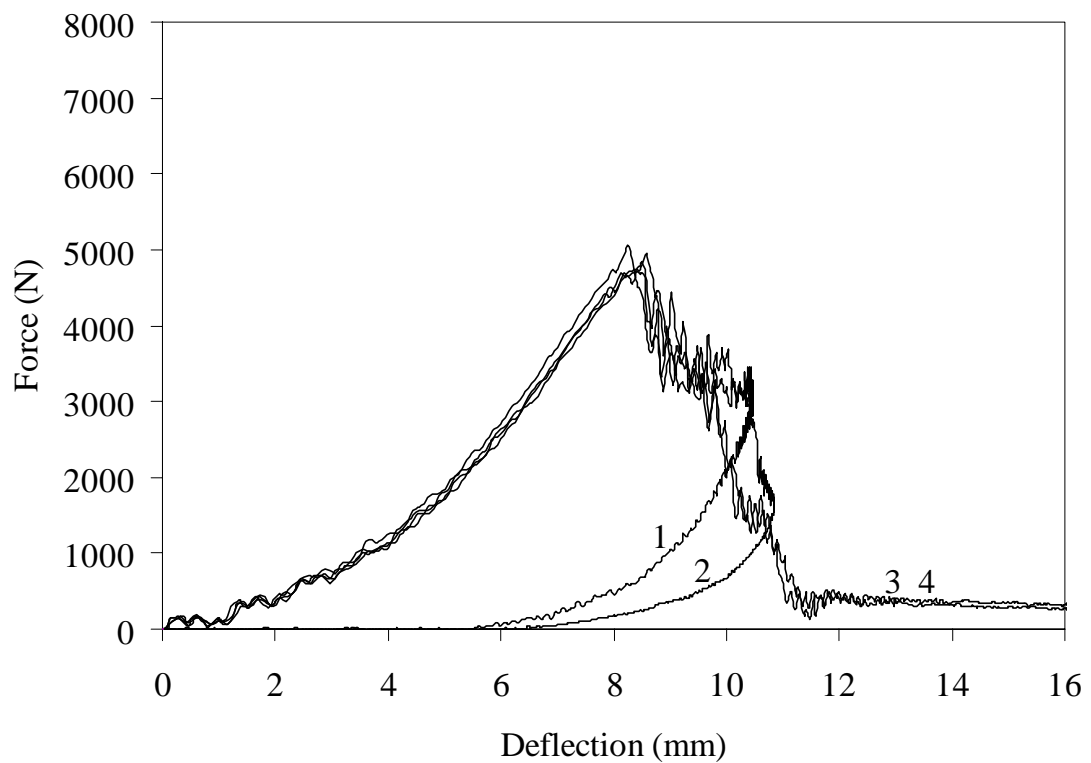


Figure A.5 Force-deflection curves of the $[\underline{90/0}]_4^{25.4 \times 25.4}$ composite plates produced without gap and cured under high pressure (HP₂)

Table A.6 Impact velocities of the $[\underline{90/0}]_4^{25.4 \times 25.4}$ composite specimens produced with gap and cured under low pressure (LP₁)

$[\underline{90/0}]_4^{25.4 \times 25.4}$ LP ₁	Specimen Number				
	1	2	3	4	5
Velocity (m/sec)	3.16	3.22	3.36	3.56	3.72

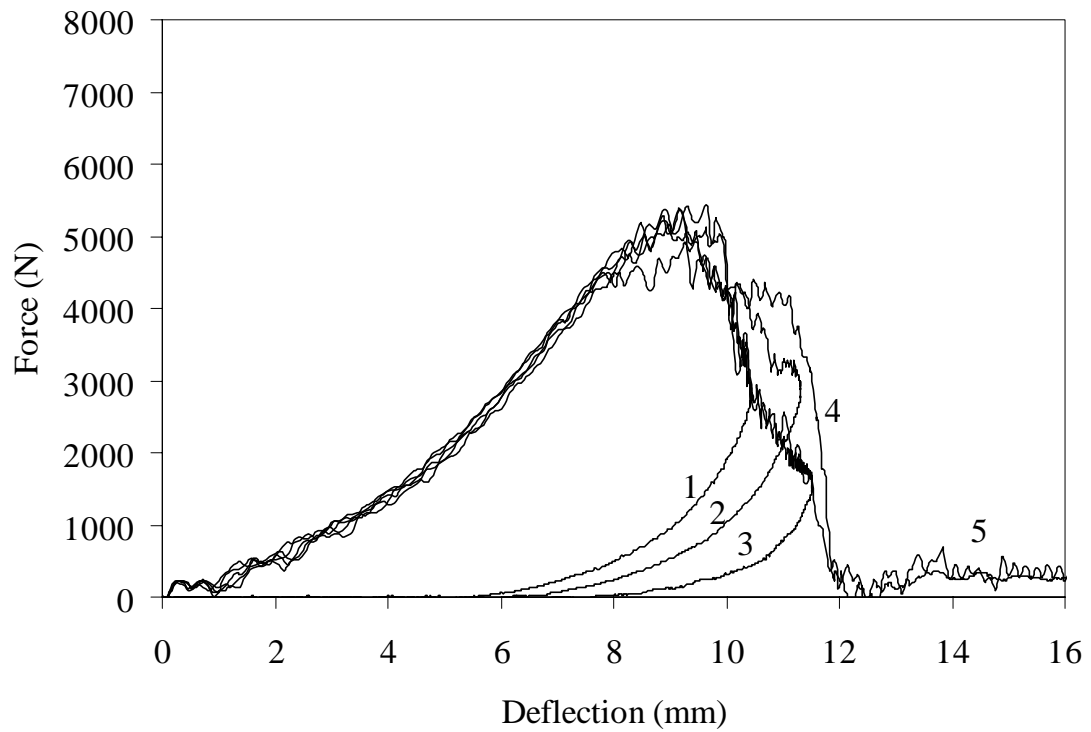


Figure A.6 Force-deflection curves of the $[\underline{90/0}]_4^{25.4 \times 25.4}$ composite plates produced with gap and cured under low pressure (LP₁)

Table A.7 Impact velocities of the $[\underline{90/0}]_4^{25.4 \times 25.4}$ composite specimens produced without gap and cured under low pressure (LP_2)

$[\underline{90/0}]_4^{25.4 \times 25.4}$ LP_2	Specimen Number			
	1	2	3	4
Velocity (m/sec)	3.14	3.12	3.26	3.43

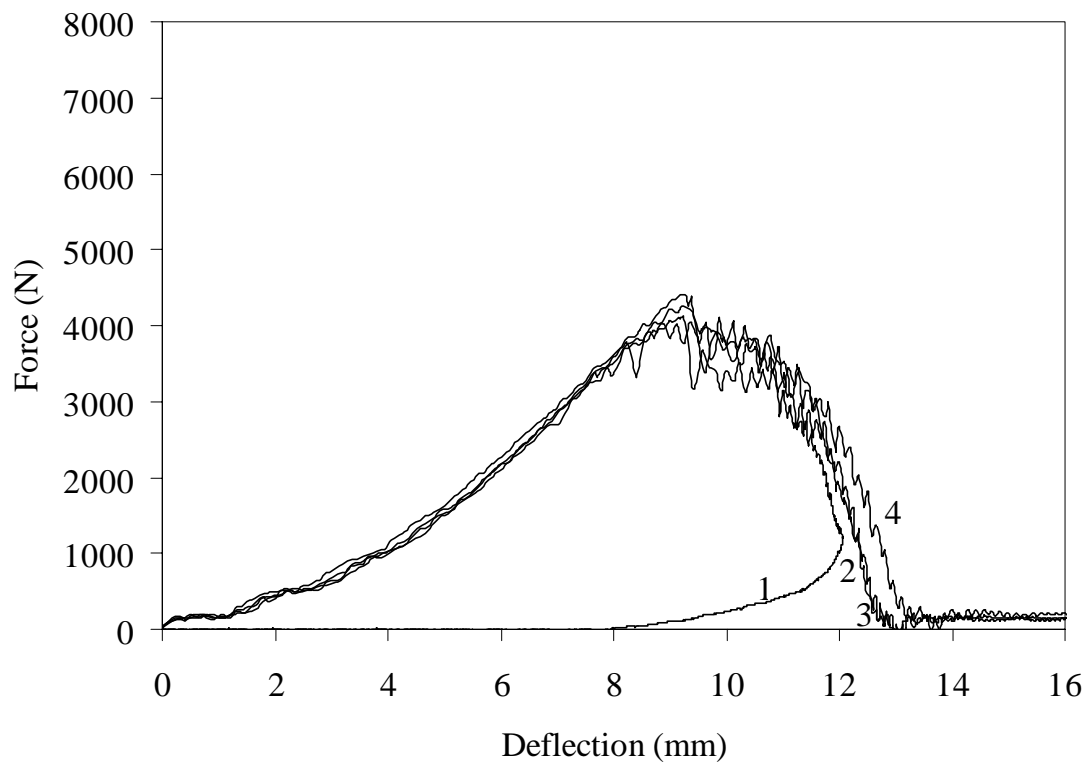


Figure A.7 Force-deflection curves of the $[\underline{90/0}]_4^{25.4 \times 25.4}$ composite plates produced without gap and cured under low pressure (LP_2)

Table A.8 Impact velocities of the $[\underline{90}/0]_6^{25.4 \times 25.4}$ composite specimens

$[\underline{90}/0]_6^{25.4 \times 25.4}$	Specimen Number				
	1	2	3	4	5
Velocity (m/sec)	3.23	3.53	3.78	3.90	4.03

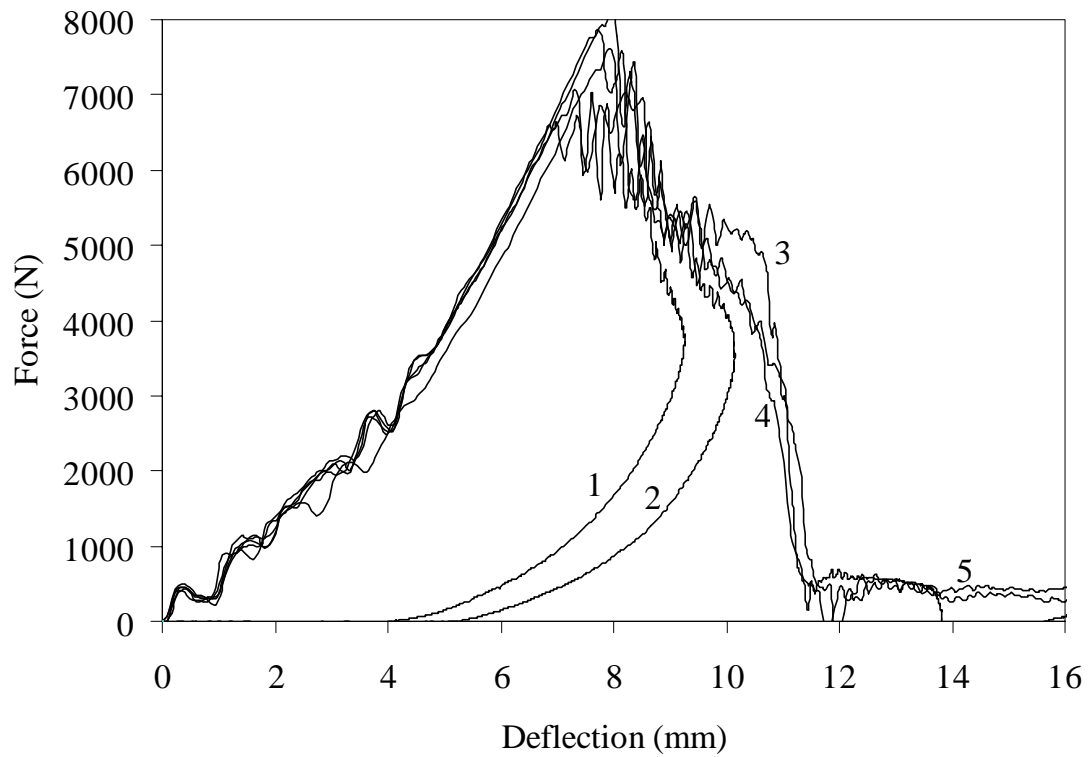
Figure A.8 Force-deflection curves of the $[\underline{90}/0]_6^{25.4 \times 25.4}$ composite plates

Table A.9 Impact velocities of the $[\underline{90}/0]_6^{12.7 \times 12.7}$ composite specimens

$[\underline{90}/0]_6^{12.7 \times 12.7}$	Specimen Number				
	1	2	3	4	5
Velocity (m/sec)	3.25	3.30	3.39	3.63	3.91

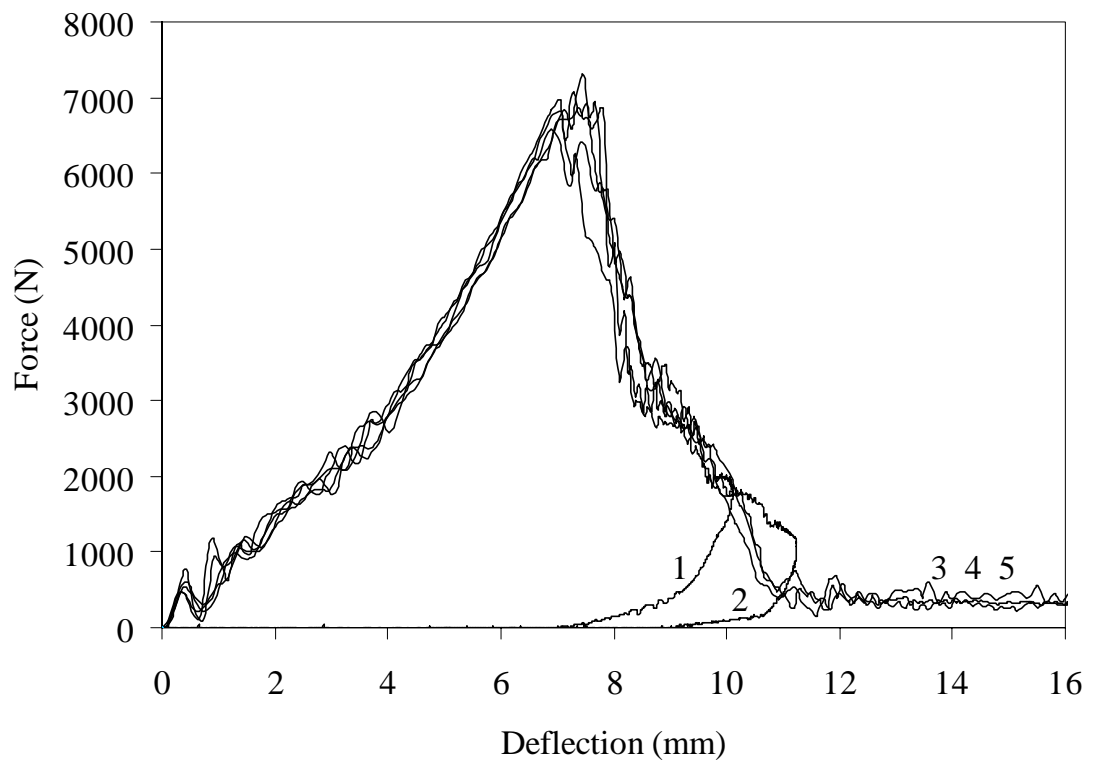


Figure A.9 Force-deflection curves of the $[\underline{90}/0]_6^{12.7 \times 12.7}$ composite plates

Table A.10 Impact velocities of the $[\underline{90/0}]_6^{6.4 \times 6.4}$ composite specimens

$[\underline{90/0}]_6^{6.4 \times 6.4}$	Specimen Number				
	1	2	3	4	5
Velocity (m/sec)	3.24	3.37	3.52	3.71	3.94

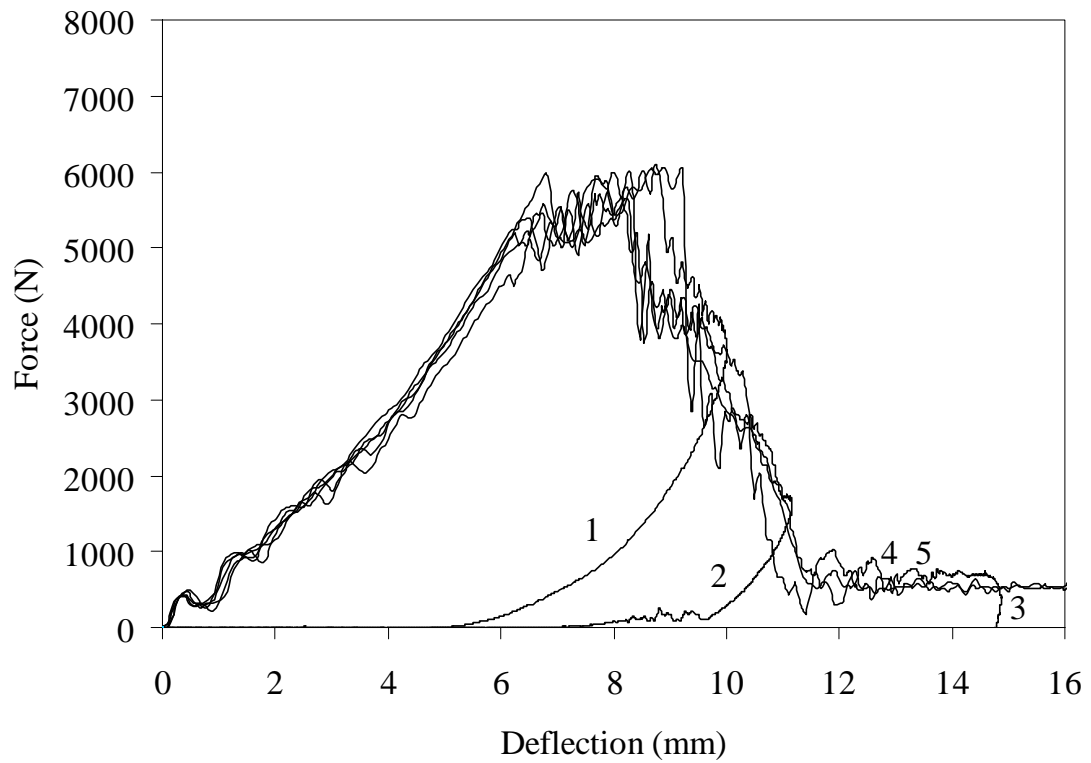
Figure A.10 Force-deflection curves of the $[\underline{90/0}]_6^{6.4 \times 6.4}$ composite plates

Table A.11 Impact velocities of the $S[90/0]_6$ composite specimens

$S[90/0]_6$	Specimen Number		
	1	2	3
Velocity (m/sec)	3.52	3.65	4.00

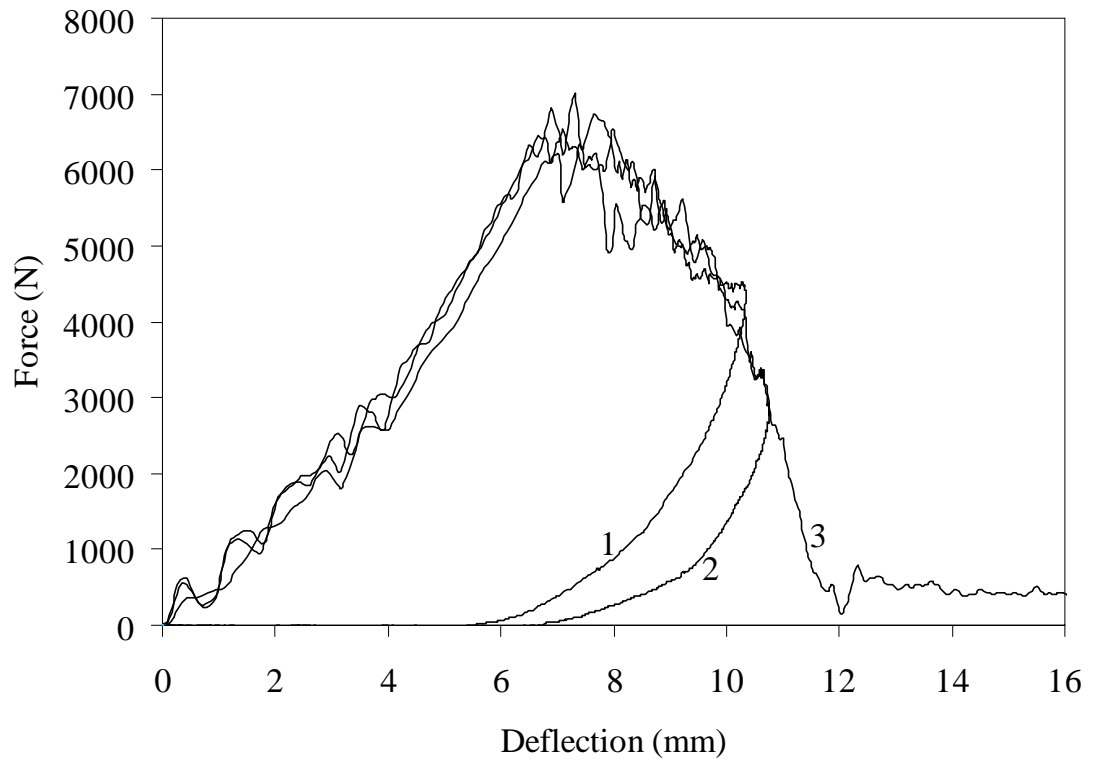
Figure A.11 Force-deflection curves of the $S[90/0]_6$ composite plates

Table A.12 Impact velocities of the $S[90/0]_6^{25.4 \times 25.4}$ composite specimens

$S[90/0]_6^{25.4 \times 25.4}$	Specimen Number			
	1	2	3	4
Velocity (m/sec)	3.73	3.59	3.77	4.00

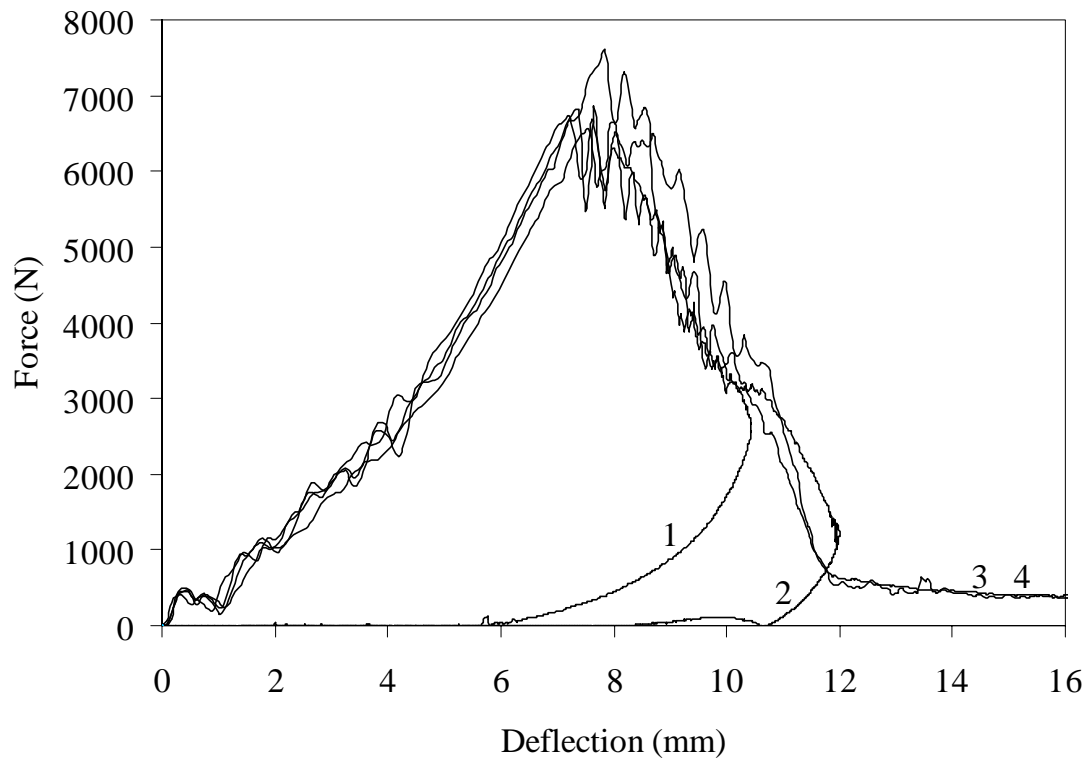
Figure A.12 Force-deflection curves of the $S[90/0]_6^{25.4 \times 25.4}$ composite plates

Table A.13 Impact velocities of the $S[90/0]_6^{12.7 \times 12.7}$ composite specimens

$S[90/0]_6^{12.7 \times 12.7}$	Specimen Number			
	1	2	3	4
Velocity (m/sec)	3.09	3.25	3.31	3.52

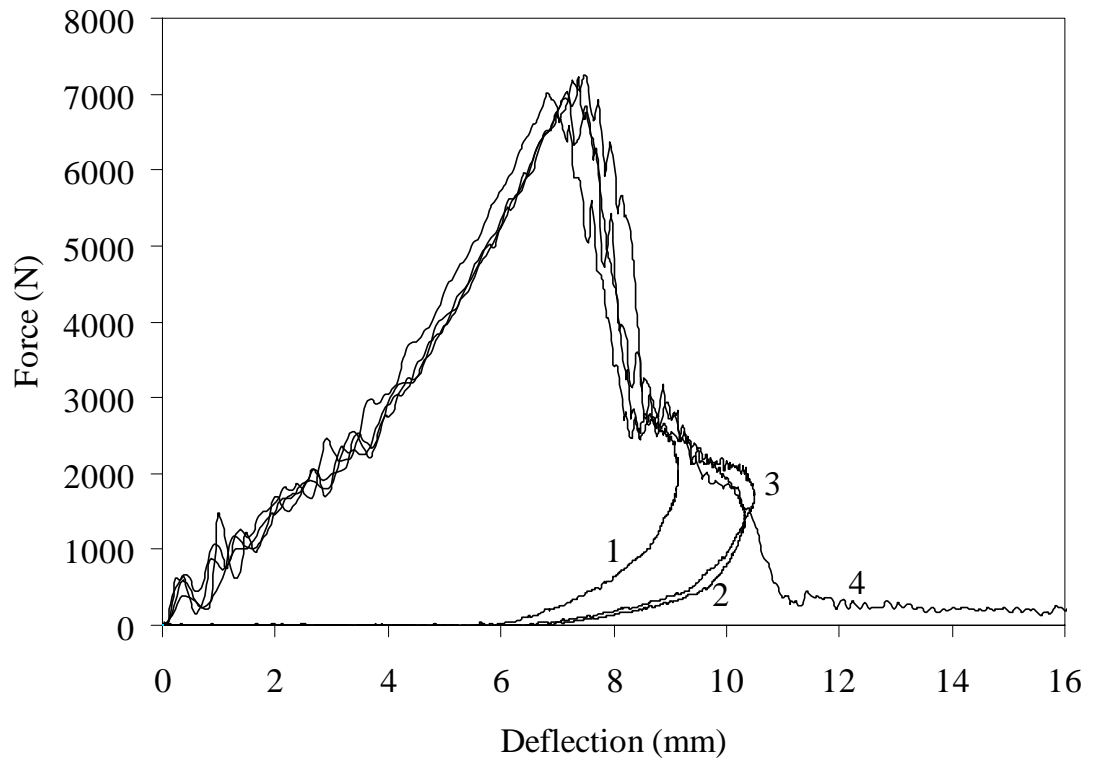
Figure A.13 Force-deflection curves of the $S[90/0]_6^{12.7 \times 12.7}$ composite plates

Table A.14 Impact velocities of the $S[90/0]_6^{6.4 \times 6.4}$ composite specimens

$S[90/0]_6^{6.4 \times 6.4}$	Specimen Number			
	1	2	3	4
Velocity (m/sec)	3.24	3.39	3.51	3.76

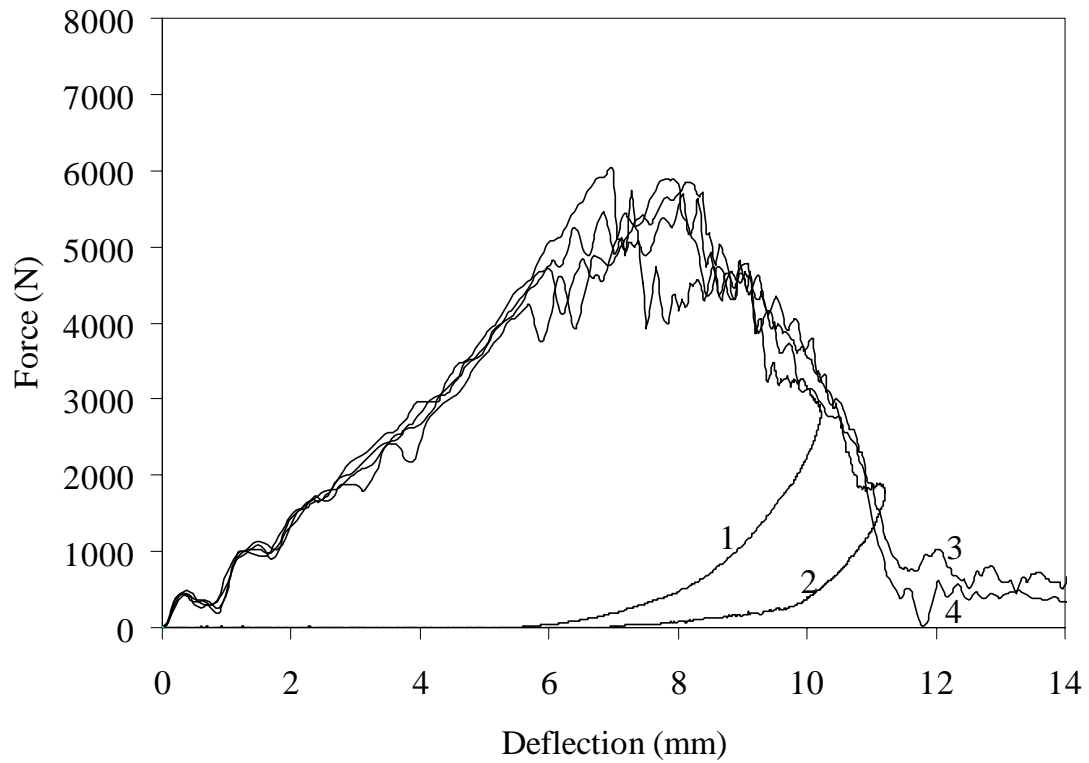
Figure A.14 Force-deflection curves of the $S[90/0]_6^{6.4 \times 6.4}$ composite plates

Table A.15 Impact velocities of the $[\underline{60}/0]_6^{12.7 \times 12.7}$ composite specimens

$[\underline{60}/0]_6^{12.7 \times 12.7}$	Specimen Number							
	1	2	3	4	5	6	7	8
Velocity (m/sec)	2.36	3.01	3.24	3.32	3.39	3.53	3.66	3.76

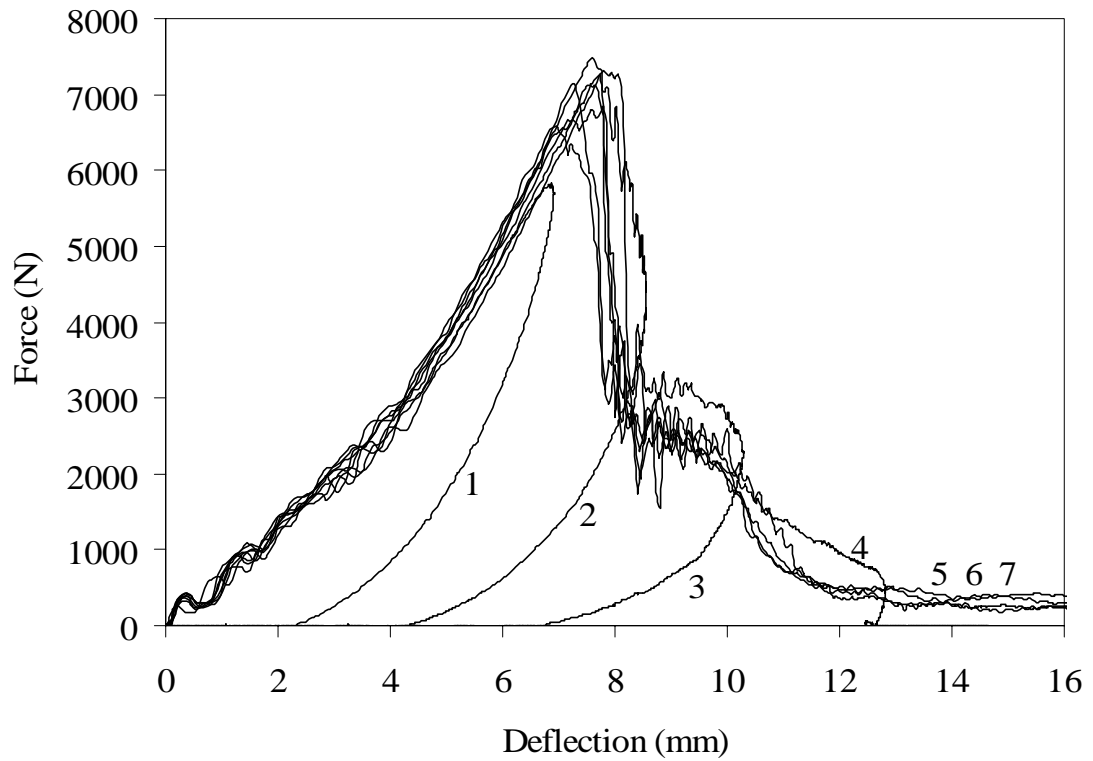
Figure A.15 Force-deflection curves of the $[\underline{60}/0]_6^{12.7 \times 12.7}$ composite plates

Table A.16 Impact velocities of the $[\underline{45/0}]_6^{12.7 \times 12.7}$ composite specimens

$[\underline{45/0}]_6^{12.7 \times 12.7}$	Specimen Number								
	1	2	3	4	5	6	7	8	9
Velocity (m/sec)	2.78	2.94	3.11	3.27	3.39	3.55	3.68	3.81	3.91

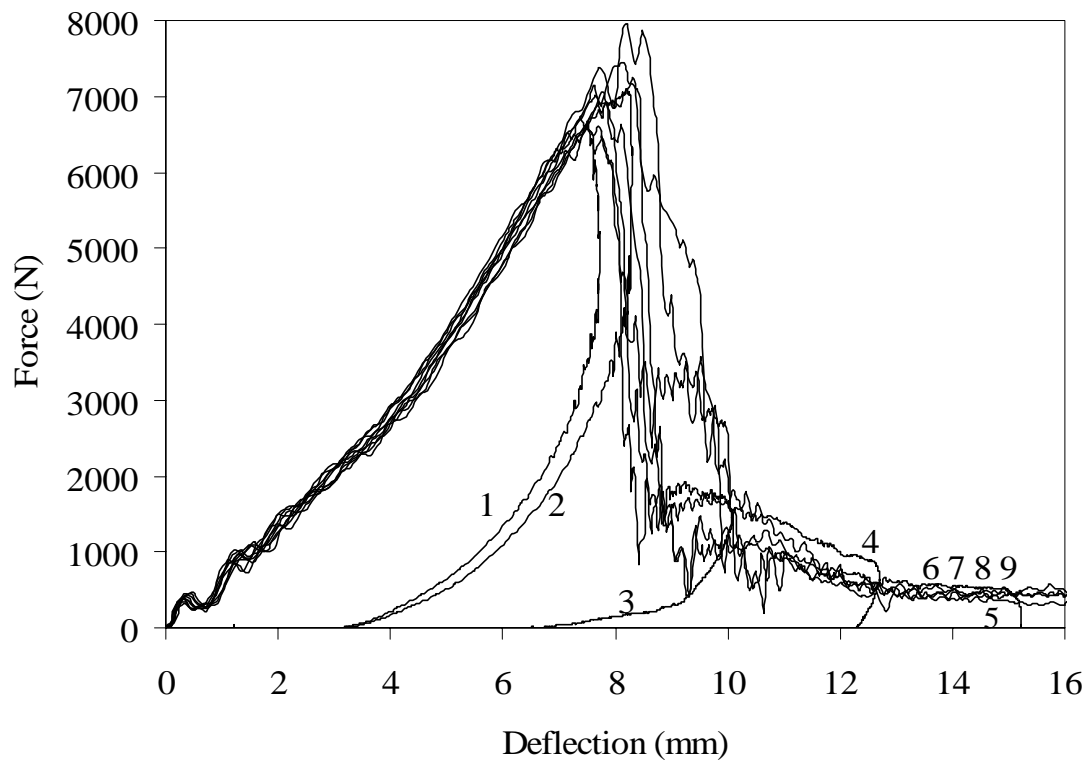
Figure A.16 Force-deflection curves of the $[\underline{45/0}]_6^{12.7 \times 12.7}$ composite plates

Table A.17 Impact velocities of the $[\underline{30/0}]_6^{12.7 \times 12.7}$ composite specimens

$[\underline{30/0}]_6^{12.7 \times 12.7}$	Specimen Number								
	1	2	3	4	5	6	7	8	9
Velocity (m/sec)	2.95	3.11	3.26	3.41	3.48	3.56	3.70	3.82	4.01

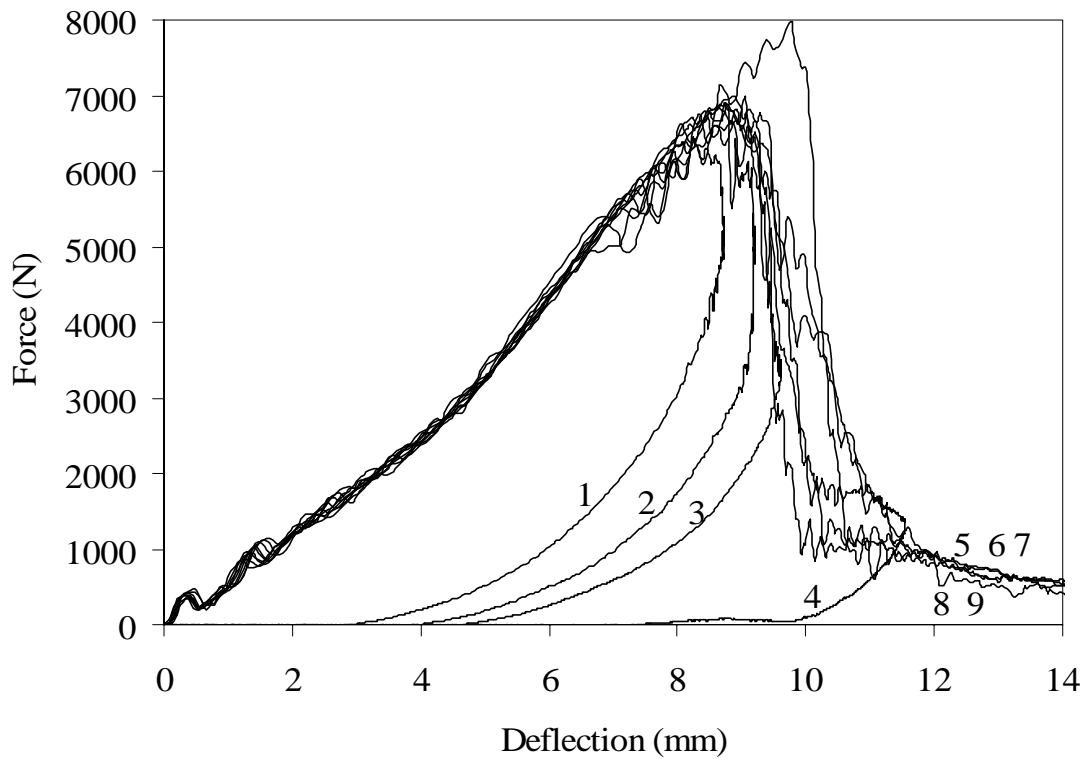
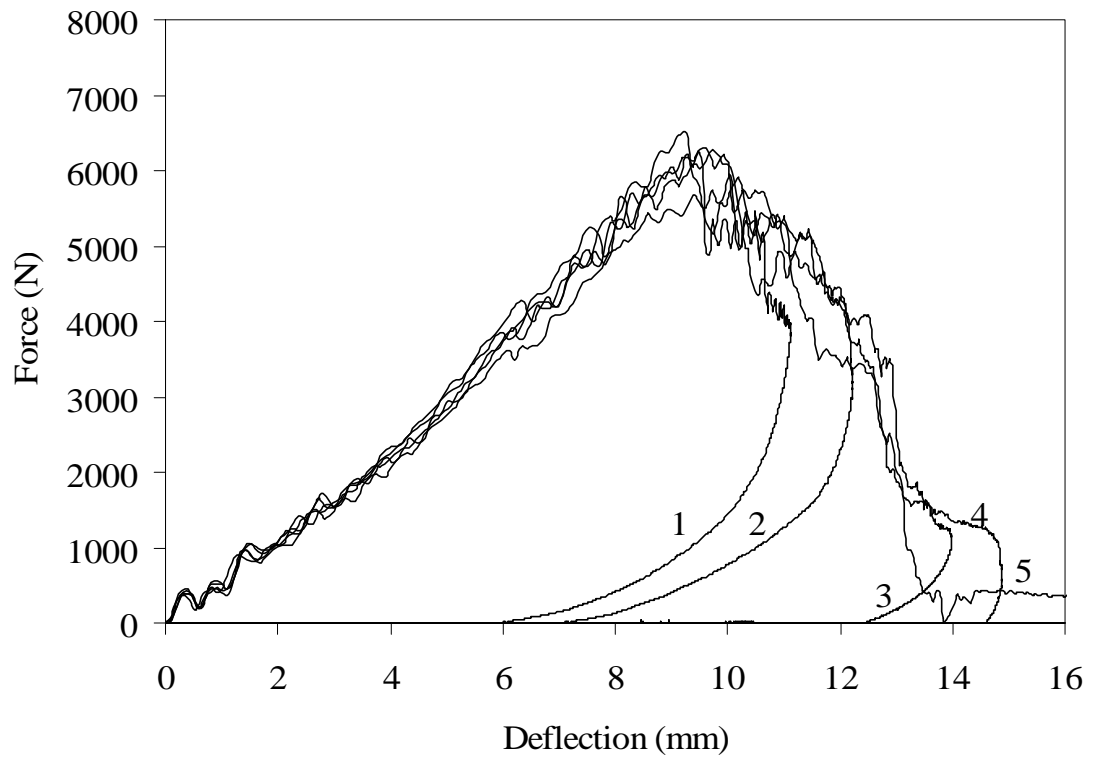
Figure A.17 Force-deflection curves of the $[\underline{30/0}]_6^{12.7 \times 12.7}$ composite plates

Table A.18 Impact velocities of the $[\underline{15/0}]_6^{12.7 \times 12.7}$ composite specimens

$[\underline{15/0}]_6^{12.7 \times 12.7}$	Specimen Number				
	1	2	3	4	5
Velocity (m/sec)	3.41	3.69	3.80	3.90	4.04

Figure A.18 Force-deflection curves of the $[\underline{15/0}]_6^{12.7 \times 12.7}$ composite plates